Master's thesis

NTNU
Norwegian University of Science and Technology
Faculty of Information Technology and Electrical Engineering
Department of Electric Power Engineering

Erlend Westad

Instantaneous Frequency Identification in Microgrids Through Adaptive Data Analysis

Master's thesis in Energy and Environmental Engineering
Supervisor: Olav Bjarte Fosso and Marta Molinas
June 2020

NTNU
Norwegian University of Science and Technology

Erlend Westad

Instantaneous Frequency Identification in Microgrids Through Adaptive Data Analysis

Master's thesis in Energy and Environmental Engineering
Supervisor: Olav Bjarte Fosso and Marta Molinas
June 2020

Norwegian University of Science and Technology
Faculty of Information Technology and Electrical Engineering
Department of Electric Power Engineering

NTNU
Norwegian University of
Science and Technology

Abstract

With increased integration of power electronic equipment and distributed energy generation, the modern power system has become more prone to harmonic pollution. As isolated systems categorized by low inertia such as microgrids are more common, the presence of non-linear distortion is becoming an increasing problem. The most common methods used for surveillance in the power system are as of now based on average value calculations. They are thus not suited for the rising non-linearity caused by the harmonics in the evolving system. For monitoring and control equipment to keep operating with adequate performance, there is a need for alternative surveillance methods capable of instantaneous frequency and amplitude detection.

This thesis aims to explore the use of adaptive data analysis as an alternative surveillance method for harmonic detection in the power system. Empirical Mode Decomposition (EMD) and its real-time extension, Online EMD, have been used in conjunction with Hilbert-Transform (HT) and Fast Fourier Transform (FFT) for extensive instantaneous frequency and amplitude identification. First, a comparison of the decomposition quality of EMD and Online EMD is made using synthetic signals, looking at different stoppage criteria and their reaction to disturbances. The methods have then been applied for harmonic detection in an actual voltage and current measurement taken from a wind turbine generator. The measurements have been decomposed by EMD, utilizing FFT and a recreated boundary condition map to construct appropriate masking signals to avoid mode mixing. The use of masking signals to avoid mode-mixing has then been adapted and used in the Online EMD for the same measurements. As adequately pure IMFs are extracted, they are removed from the original signal, and the new resulting signal is treated as new input for further decomposition. As all relevant modes are extracted, they are analyzed by HT and FFT, and the results from the EMD and Online EMD are compared.

Essentially, the methods proved to be powerful tools for harmonic detection but requires techniques to handle mode mixing when applied to complex signals. The use of masking signals is shown to be a highly effective mode mixing separation technique and is seen to also be effective when adapted for use with the Online EMD.

Sammendrag

Den økende integreringen av kraftelektroniske komponenter har sammen med mer distribuert generering av energi ført til at kraftsystemet er mer usatt for harmonisk forurensning. Isolerte systemer typisk kategorisert av lavt treghetsmoment er spesielt usatt, og har gjort ikke-lineære harmonisk støy til et økende problem. Dagens monitoreringsutstyr benytter seg i stor grad av metoder som baserer seg på gjennomsnittlige verdier og utregninger, og er dermed ikke egnet for å benyttes ved større grad av ikke-linearitet. Det trengs dermed en alternativ metode med mulighet for å beregne momentant frekvens og amplitude slik at kontrollutstyr skal kunne fungere med nødvendig nøyaktighet og presisjon.

Denne oppgaven utforsker bruken av adaptiv data analyse som en alternativ metode for detektering av harmoniske komponenter i kraftsystemet. Empirical Mode Decomposition (EMD) og sanntids versjonen Online EMD har blitt brukt sammen med Hilbert-Transform (HT) og Fast Fourier Transform (FFT) for å se nærmere på muligheten for momentan frekvens og amplitude beregning. En sammenlikning av dekomposisjon kvaliteten til EMD og Online EMD er gjort for forskjellige stop-kriterier og forstyrrelser. Deretter har metodene blitt brukt for å indentifisere det harmoniske innholdet i en virkelig strøm og spenningsmåling henter fra en vind turbin. EMD ble brukt til å dekomponere målingene, og FFT ble brukt sammen med et grensetilstands-kart for å konstruere maskerings signal for å forhindre frekvens miksing. Bruken av maskerings signal ble så modifisert til bruk sammen med Online EMD, for de samme målingene. Tilfredsstillende IMFer ble deretter fjernet fra det originale signalet og det resulterende signalet ble analysert på nytt. Etter at alle relevante komponenter har blitt fjernet fra signalet blir de videre analysert ved hjelp av HT og FFT, og resultatene fra EMD og Online EMD blir sammenliknet.

Metodene brukt i denne oppgaven viste seg å være gode verktøy for å finne det harmoniske innholdet i et signal, men krever teknikker som kan behandle mode-miksing ved mer komplekse signaler. Maskerings-signal var veldig effektiv seperasjons metode, og den viste seg og også fungere godt sammen med Online EMD.

Preface

This is the master's thesis to conclude the Master of Science degree in Energy and Environmental Engineering at the Norwegian University of Science and Technology. The work was carried out at the Department of Electric Power Engineering during spring 2020.

I want to express my sincere gratitude to my supervisor Professor Olav Bjarte Fosso, for excellent guidance and for providing the opportunity to work on such an interesting topic. I also want to thank my co-supervisor, Professor Marta Molinas. Her insightful lectures sparked my interest for the world of signal analysis.

Trondheim, June 4, 2020
Erlend Westad

Table of Contents

List of Figures

Abbreviations

DER	Distributed Energy Resources
DFT	Discrete Fourier Transform
EMD	Empirical Mode Decomposition
FFT	Fast Fourier Transform
HHT	Hilbert-Huang Transform
HT	Hilbert Transform
IA	Instantaneous Amplitude
IF	Instantaneous Frequency
IMF	Intrinsic Mode Function
PCC	Point of Common Coupling
RMS	Root-Mean-Square
STFT	Short-Time Fourier Transform
THD	Total Harmonic Distortion
WT	Wavelet Transform
WTG	Wind Turbine Generator

Chapter 1

Introduction

1.1 Background and Motivation

This thesis is a continuation of a specialization project done prior to this work, thus the background and motivation is here presented as an adapted and revised version from [1].

For a long time, the power system has been characterized by excellent power and frequency quality, ensured by the high inertia rotating masses of the generators in the system. As such, the frequency was not likely to deviate far from the fundamental frequency, usually keeping a steady 50 Hz or 60 Hz. However, as the electrical grid is evolving, new components, such as power electronics converters, rectifiers, and adjustable speed drives, now interact at a larger scale. Combined with the increase of non-linear loads, the electrical grid is more prone to harmonic pollution as harmonic injection and non-linear distortions are becoming common.

Power systems with no connection to a stiff grid, typically categorized by low inertia, are especially susceptible to harmonic pollution. Isolated microgrids such as wind farms, marine vessels, and solar microgrids are only some examples of such systems as large frequency deviations caused by harmonics can cause significant damage. Furthermore, as a result of more advanced inverter control, conditions with varying load demand may lead to time-varying oscillations in such power systems [2]. To satisfy the operational conditions of the low inertia microgrids, sophisticated control and monitoring methods are needed. Monitoring methods linked to frequency-related issues have been relying on Fourier based analysis, and the concept of *instantaneous frequency* has yet to be used on a larger scale for monitoring or control purposes in the electric power system [3].

The standard methods used for data acquisition in the power system today assumes a constant fundamental frequency, relying on average value calculations and only considered constant harmonics that are integer multiples of the fundamental frequency [4, 5, 6]. Looking at the IEC Standard 61000-4-7, it is apparent that the currently used methods are

inaccurate when dealing with environments of time-varying angular frequency [7]. For control and monitoring equipment to keep adequate control, measurement, and estimation techniques relying on average values should transition to rely on instantaneous frequency and amplitude [2][8]. However, using mathematical formulations to describe physical behavior in large scale systems can be challenging. Controllers relying on mathematical models and approximations may lead to complex control schemes whose operations might be challenging to understand, and implementation might be costly due to their complex nature. As opposed to this high-fidelity modeling, this thesis explores the use of adaptive data analysis as an alternative method for frequency and harmonic monitoring in the power system. Using methods capable of handling both non-linear and non-stationary signals, available measurements are used to characterize the grid under investigation. Relying on instantaneous values, the control systems used in microgrids should be able to perform faster and more accurate actions, resulting in a more secure and stable power grid.

1.2 Objective and Scope of Work

This thesis's objective is to explore adaptive data analysis as an alternative to present methods used for monitoring and control in the power system. This is done by assessing the potential of EMD and online EMD when used in conjunction with HT and FFT. Thus, the main methods are thorough review of existing literature and further implementation of the methods in MATLAB. Further investigation is done by constructing synthetic signals to compare decomposition quality, and by applying the detection methods to an actual voltage and current measurement to identify the harmonic content. Techniques for mode-mixing separation in the EMD are also explored, mainly focusing on masking signals constructed by the help of frequency identification through FFT and a boundary condition map. This technique is then adapted and investigated when used with the Online EMD.

1.3 Structure of Thesis

- **Chapter 1: Introduction** - Here the background and motivation for this thesis is presented. Also included are the Objective and Scope of work, and the structure of the thesis.
- **Chapter 2: State-of-the-art in Methods for Frequency Identifications in Microgrids** - This chapter presents a more thorough theoretical background for the relevant techniques used in this thesis. A brief introduction to the concepts of microgrids and harmonics is also given.
- **Chapter 3: Comparison of Classical and Online EMD** - In this chapter a comparison of the decomposition quality of classical and Online EMD is made by various synthetic signals.
- **Chapter 4: Frequency and Amplitude Identification Through HHT and Online EMD** - In this chapter a real voltage and current measurement is analysed by EMD, Online EMD, HT and FFT.

- **Chapter 5: Conclusion and Future Work** - Conclusion of the thesis and recommendations for future work.
- **Appendix A:** - Contains more graphs from the step-by-step decomposition of signals $L1$ and $L12$, and a recreation of the original signals from the resulting IMFs. A closer look at the IF and IA plot for the resulting IMFs is also included.

Chapter 2

State-of-the-art in Methods for Frequency Identification in Microgrids

The state of art were reviewed, and an identification of some of the relevant background material were carried out in the project preceding this thesis [1]. The relevant sections have thus been revised and adapted to be presented in this masters thesis.

2.1 Concept of Microgrids and Harmonics

2.1.1 Microgrids

The definition of a microgrid given by the US department of energy is [9]: *"a group of interconnected loads and distributed energy resources with clearly defined electrical boundaries that act as a single controllable entity for the grid and can connect and disconnect from the grid to enable it to operate in both grid-connected or island modes"*. Being a combination of storage devices, distributed energy sources, and flexible loads, the microgrid is an entirely localized energy system capable of operating both connected and disconnected to the traditional macro grid. Disconnecting from the grid is often called "islanding," while the interconnection point is referred to as Point of Common Coupling (PCC) [10].

An essential aspect of the microgrid is local generation capability, thus integrating local renewable energy sources such as solar, wind, small hydro, geothermal, waste-to-energy, and combined heat and power is done to ensure reliable generation of power when not connected to the main grid. Less distance between generation and load leads to lower transmission losses, resulting in a more efficient power system. By integrating the local generation, the microgrid can operate as a power source for the main grid in times of out-

age or failure. This not only ensures a more secure and reliable main grid but results in more reliable and affordable energy for both urban and rural communities.

Contrary to the high inertia of the traditional power system, lower inertia is a significant concern for the microgrid as frequency, and speed deviation is inversely proportional to the inertia of the system. The high inertia rotating masses, i.e., synchronous generators in the traditional power grid, serve as storage for additional energy in the system during disturbances, thus ensuring constant voltage and frequency levels [11]. Furthermore, an increased load on the system causes a mismatch between the mechanical and electrical power, thus slowing the rotor using the kinetic energy to compensate for the difference in supply and demand. However, the low inertia of the microgrid makes such control schemes ineffective when dealing with system transients. The microgrid thus needs sophisticated frequency control and surveillance, as well as efficient energy storage to deal with transients when operating independently from the main grid.

2.1.2 Harmonics

This section provides a short introduction to the concept of harmonics. The information presented here is mainly from [12], where more thorough information on harmonics and its impact on the power system can be found. Here harmonics refers to the components of a waveform that is an integer multiple of that waveform's fundamental frequency [12]. When mentioned in the power system, harmonics usually refer to the harmonic content found in either the current or voltage of the system. Thus, for a power system with a fundamental frequency of 50 Hz, the third harmonic implies the presence of a 150 Hz component and the fourth harmonic a 200 Hz component. Thus, harmonic components are referred to by order and is given by:

$$f_h = h \cdot f_n \tag{2.1}$$

Where f_n is the fundamental frequency and h is the harmonic order. Such that the fifth order harmonic f_5 is given by

$$f_5 = 5 \cdot 50Hz = 250Hz \tag{2.2}$$

Non-integer multiples of the fundamental frequency may also appear, though less common, this phenomenon is referred to as inter-harmonics. Harmonic voltages and currents are sources of many problems within the power system. These problems include overheating of equipment and cabling, reduced energy efficiency, and reduced functionality due to loss of electromagnetic compatibility [12]. Furthermore, the harmonic current from installations can flow back into the network propagating as voltage harmonics, causing the supply waveform to be distorted, leading to increased network losses and lower reliability for several types of equipment [12]. The presence of harmonic current in the electric supply system is not a new phenomenon. The phenomenon was initially produced by the mercury arc rectifiers when converting AC to DC for railway electrification, by industrial DC variable speed drives, and by direct half-wave rectification used in radio and television sets [12]. However, the modern power system relying more on power electronic components and other passive equipment interacting at a larger scale has caused the number of

units causing harmonics to increase[12].

Total Harmonic Distortion (THD) is used to measure the degree of harmonics present in the power system. THD is defined as the ratio between the harmonics and the fundamental frequency present in the signal. Let the current with harmonic presence be given as:

$$i_s(t) = i_{s1}(t) + \sum_{h \neq 1} i_{sh}(t) \tag{2.3}$$

Where i_{s1} is the fundamental component and $i_{sh}(t)$ the harmonic component. The THD of the current in 2.3 referreing to RMS value is given as [13]:

$$\%THD = 100 \cdot \frac{\sqrt{i_s^2 - i_{s1}^2}}{i_{s1}} = 100 \cdot \sqrt{\sum_{h \neq 1} (\frac{i_{sh}}{i_{s1}})^2} \tag{2.4}$$

In an ideal power system, the current and voltage waveforms are pure sinusoids with no distortions. Realistically the system will contain some harmonics. When a non-linear relation between the applied voltage and current flowing in the load occurs, non-sinusoidal currents (and voltages) are generated. This should not be confused with a phase shift between the waveforms, as usually seen in simple circuits containing capacitance or inductance, as the current flowing will still be proportional to the voltage. However, given a circuit consisting of a full-wave rectifier and a capacitor, the supply voltage must exceed that stored on the reservoir's capacitor for the current to flow. Thus, the current only flows when the voltage is close to the peak of the voltage sine wave [12]. This produces a cyclic waveform as seen in Figure 2.1(b).

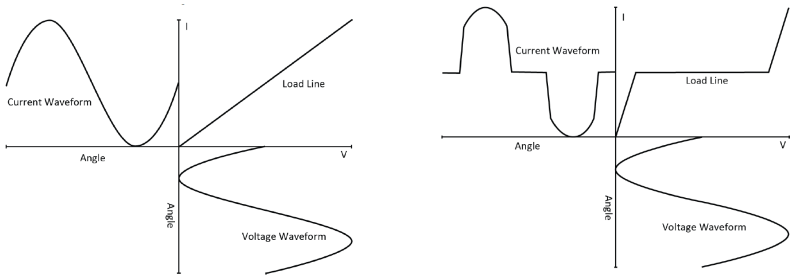

(a) Current waveform in a linear load **(b)** Current waveform in a non linear load

Figure 2.1: Waveforms of linear and non linear loads [12]

Though this waveform is a cropped version of the waveform given a linear load as seen in Figure 2.1(a), this current waveform can be deconstructed into several sine waves that together result in what can be seen in Figure 2.1(b). All the additional sine waves contributing to the flat shape will be the resulting harmonics in the wave. This makes it apparent

that the distorted current waveform, as seen in Figure 2.1(b) is the sum of the fundamental harmonic and a percentage of some higher-order harmonics.

2.2 Fourier Transform

The Fourier transform (FT), developed by Jean B.J Fourier in 1807, is regarded as a powerful tool in spectrum analysis. However, the method did not gain its current popularity before the development of the Fast Fourier Transform (FFT) in 1965 [14]. Based on the Discrete Fourier Transform (DTF), the FFT is a method for efficiently computing the finite FT of N complex data points in $Nlog_2N$ operations [15]. Defined in Equation (2.5), the FT results in the Fourier expansion seen in Equation (2.6), a trigonometric function that is complete, convergent, orthogonal and unique.

$$\mathfrak{F}\{g(t)\} = G(f) = \int_{-\infty}^{\infty} g(t)e^{-2i\pi ft}dt \tag{2.5}$$

This allows every signal to be decomposed into a combination of sinusoidal waves $x(t)$, each with constant amplitude a_j and frequency ω_j [16].

$$x(t) = \sum_j a_j e^{i\omega_j t} \tag{2.6}$$

The discrete implementation of the FT is given in Equation (2.7).

$$A_r = \sum_{k=1}^{N-1} X_k e^{\frac{-2\pi irk}{N}} \qquad r = 0, ..., N-1 \tag{2.7}$$

Where A_r is the *r*th cofficient of the DFT, $j = \sqrt{-1}$ and X_k denotes the *k*th sample of the time series consisting of N samples.

The FFT iteratively calculates coefficients, combining progressively larger weighted sums of data samples to produce the resulting DFT coefficients seen in Equation 2.7 [17]. By leveraging the use of symmetries in the transformation, the FFT is a more efficient implementation of the DFT, effectively reducing the number of computing operations needed from $\mathcal{O}(N^2)$ to $\mathcal{O}(NlogN)$. However, it is also important to note that as the FFT is an integral transformation that imparts a domain change from time to frequency, it is limited by the uncertainty principle. Thus, the determination of frequency is time interval dependent, imposing a strong limitation when the demand for both frequency and time resolution is very high[16].

2.2.1 Fourier Transform in the Power System

The FFT is as of today the standard method used for harmonic measuring and monitoring in the power system [4, 5, 6]. When applying Fourier series for harmonic measurement in the electrical power grid, it should be implemented as given by IEEE 519 and IEC 61000-4-7 [6, 4, 5] as seen in Equation (2.8) to (2.15).

$$f(t) = c_0 + \sum_{m=1}^{\infty} c_m \sin(\frac{m}{N}\omega_1 t + \varphi_m) \tag{2.8}$$

$$c_m = \sqrt{a_m^2 + b_m^2} \tag{2.9}$$

$$C_m = \frac{c_m}{\sqrt{2}} \tag{2.10}$$

$$\varphi_m = \arctan(\frac{a_m}{b_m}) \qquad if \quad b_m \geq 0 \tag{2.11}$$

$$\varphi_m = \pi + \arctan(\frac{a_m}{b_m}) \qquad if \quad b_m \leq 0 \tag{2.12}$$

$$b_m = \frac{2}{T_w} \int_0^{T_w} f(t) \sin(\frac{m}{N}\omega_1 t + \phi_m) dt \tag{2.13}$$

$$a_m = \frac{2}{T_w} \int_0^{T_w} f(t) \cos(\frac{m}{N}\omega_1 t + \phi_m) dt \tag{2.14}$$

$$c_0 = \frac{1}{T_w} \int_0^{T_w} f(t) dt \tag{2.15}$$

The signal is decomposed into a finite set of sinusoids of fundamental frequency ω_1 and mean value c_m. T_w is the width of the time window in which the Fourier transform is performed, while N denotes the number of fundamental periods within said window. The harmonic order, or the ordinal number related to the frequency basis ($f = \frac{1}{T_w}$), is given by m. Note that as the measurements obtained in the power system are of discrete-time, the FT is not implemented exactly as in the equations above, but rather as an adapted version to fit the FFT previously mentioned. Digital measurement instruments based on 50 Hz frequency systems are recommended by IEEE Standard 519, when applying FT based techniques, to use a window length of 10 cycles i.e., $T_w = 0.2$ [4]. This results in new spectral components every 0.2 seconds.As such, the method is not capable of instantaneous detection and will result in unreliable readings when time-varying frequencies or inter-harmonics are present. The effect of a time-varying frequency on the FFT is referred to as *leakage*. The energy at one point spreads to the adjacent frequencies, resulting in amplitude peaks spread over a larger frequency domain. In the presence of inter-harmonics i.e., harmonics given by non-integer times the fundamental, a distorted amplitude split between the closest integer frequency-bins can be observed. This is referred to as the *picket-fence-effect* [5]. To further illustrate the FFT capabilities, it is applied to several synthetic signals featuring different characteristics. The respective signals and their resulting transformation can be seen below in Figure 2.2 to 2.6.

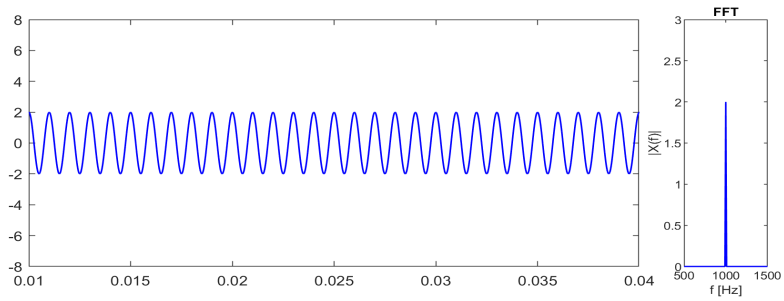

Figure 2.2: FFT applied to a linear and stationary signal $x(t) = 2cos(2\pi 1000t)$.

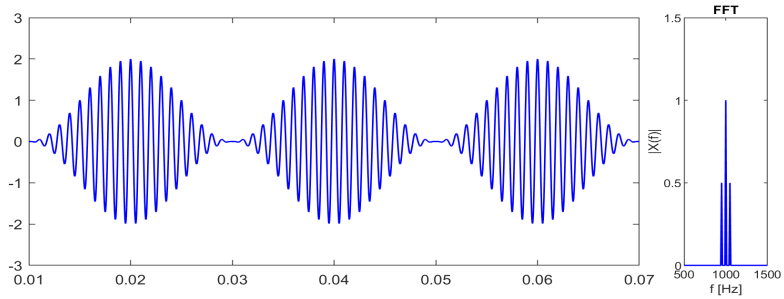

Figure 2.3: FFT applied to a signal with varying amplitude $x(t) = (1+cos(2\pi 50t))cos(2\pi 1000t)$.

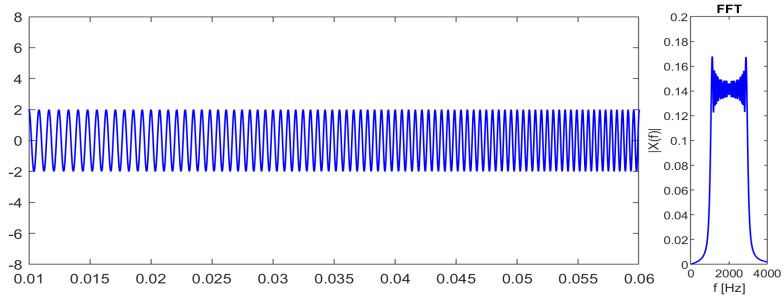

Figure 2.4: FFT applied to a signal with increasing frequency $x(t) = 2cos(2\pi((z + 1000)t))$. z being the rate of frequency increase.

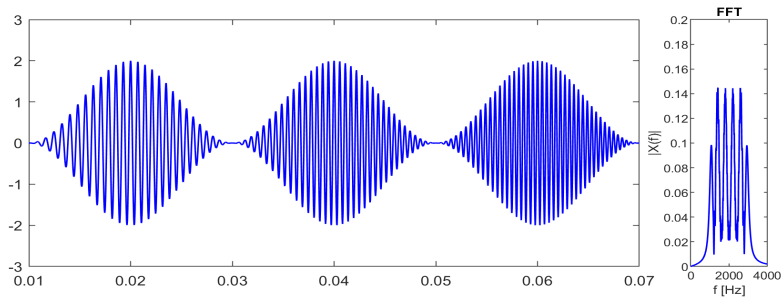

Figure 2.5: FFT applied to a signal with increasing frequency and varying amplitude $x(t) = (1 + cos(\pi 50t))cos(2\pi((z + 1000)t))$. z being the rate of frequency increase.

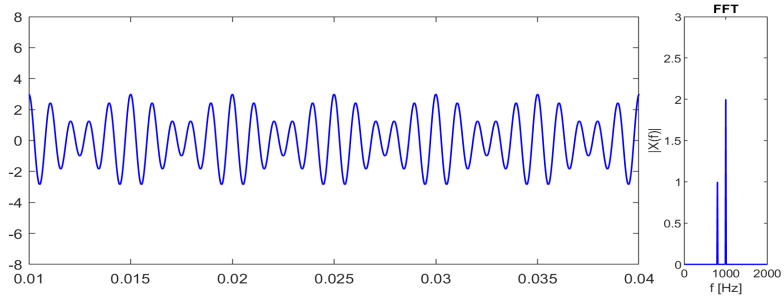

Figure 2.6: FFT applied two superimposed signals $x(t) = cos(2\pi 800t) + 2cos(2\pi 1000t)$.

2.3 Hilbert Transform

The uncertainty principle limits the time-frequency relationship in many of the methods used for time series analysis. Though this issue is addressed in versions such as Short Time Fourier Transform (STFT), where the spectral window can be chosen based on the required time and frequency resolution [16], or Wavelet Transform (WT) were the frequency and time resolution is relative to the frequency of the signal [3], they are not capable of accurate real-time tracking. Integral methods such as these are, by definition, not suited to deal with varying frequency, as the frequency is not a function of time within the integral limit. The differential equations can only see frequency as a constant, not a varying parameter. Thus, it is necessary to introduce new characteristics; Instantaneous Frequency (IF) and Instantaneous Amplitude (IA). By using the Hilbert Transform (HT) of a given time series, a strong analytical signal is generated, making it possible to calculate the IA and IF.

The HT is an integral transform defined in the time domain as a convolution between the Hilbert Transformer $\frac{1}{\pi t}$ and a function $f(t)$ [18]:

$$\hat{f}(t) = \frac{1}{\pi} P \int_{-\infty}^{\infty} \frac{f(\tau)}{t-\tau} d\tau \tag{2.16}$$

Where P indicates the Cauchy principal value.

Contrary to other transformations such as the FT, HT does not involve a domain change. Thus the resulting transformed time series is not equivalent to the original signal. However, as HT can be represented by a phase shift of 90° to every Fourier component of a function $\hat{f}(cos(t)) = sin(t)$,(i.e., a linear filter shifting the phase by $\frac{\pi}{2}$ while maintaining the amplitude), four consecutive HT applied to a time series will result in the original representation of said time series. Figure 2.7 shows how the real part of the HT represents the envelope of the transformed signal.

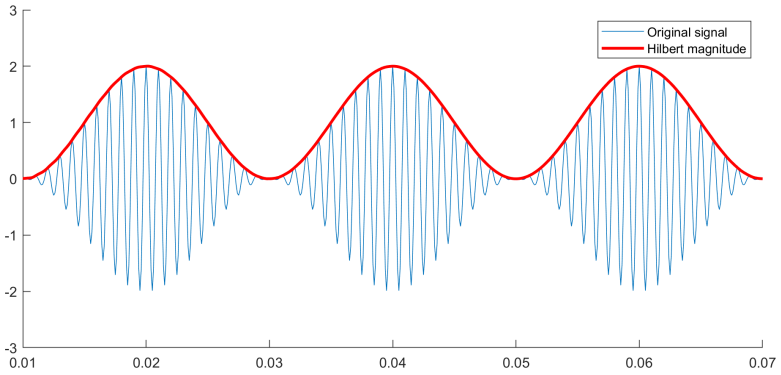

Figure 2.7: A signal with varying amplitude and its envelope, calculated using the magnitude of the Hilbert Transform

The HT $\hat{f}(t)$ is related to the original signal $f(t)$ such that together they create a *strong analytic signal*, and can be expressed in exponential form as shown in Equation (2.17).

$$z(t) = f(t) + i\hat{f}(t) = A(t)e^{i\varphi(t)} \tag{2.17}$$

where

$$A(t) = \sqrt{f(t)^2 + \hat{f}(t)^2} \tag{2.18}$$

$$\varphi(t) = arctan(\frac{\hat{f}(t)}{f(t)}) \tag{2.19}$$

By expressing $z(t)$ with an amplitude $A(t)$ as in 2.18 and a phase $\varphi(t)$ as in 2.19, the IF can be expressed as the derivative of the phase, or as *rate of change of phase*, shown in equation 2.20.

$$\omega(t) = \frac{1}{2\pi}\frac{d\varphi(t)}{dt} \tag{2.20}$$

As can be seen from Equation 2.17, a visualization of the HT can be achieved by viewing the resulting analytical signal as a vector rotating in the complex plane with angular speed $\omega(t)$ and magnitude $A(t)$. A perfect circle represents a mono-variable time series with constant amplitude and frequency, as a linear increase in phase at a constant magnitude results in smooth rotation and a constant IF and IA. Using an arbitrary linearly increasing phase (and magnitude) as a baseline, deviations from this line is the cause of change in the calculated IF. The instantly calculated frequency makes it possible to handle both varying and instantly changing frequencies in a mono-variable signal. However, given a multi-variable signal, the IF will represent a mix of all frequencies in the signal with increasing complexity depending on the number of components. It is thus commonly used in conjunction with EMD to separate the modes of oscillation before the HT. This process is referred to as the Hilbert-Huang Transform [19]. The definition of frequency as a time-varying parameter is, however, highly controversial. Time and frequency are generally viewed as inverse quantities, thus making instantaneous localization of frequency ambiguous at best [16]. Nevertheless, HT has been shown to determine the spectral peaks for non-stationary signals quite well. Examples of the HT applied to different signals can be seen in Figures 2.8 to 2.13.

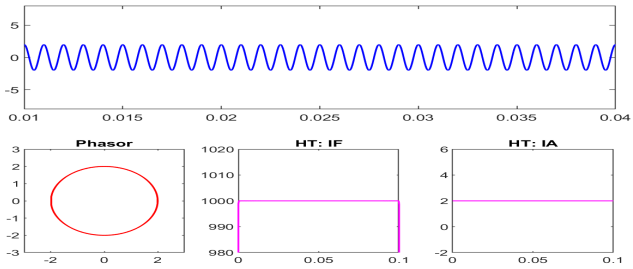

Figure 2.8: The complex phasor representation, instantaneous frequency and instantaneous amplitude resulting from the HT applied to a linear and stationary signal $x(t) = (1 + cos(2\pi 50t))cos(2\pi 1000t)$.

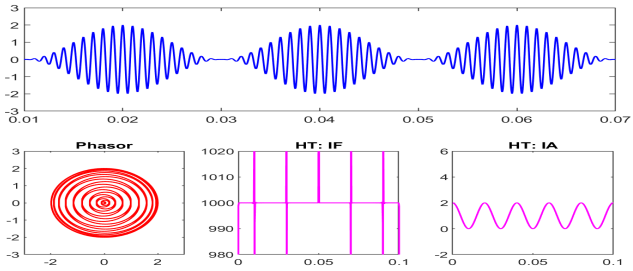

Figure 2.9: The complex phasor representation, instantaneous frequency and instantaneous amplitude resulting from the HT applied to a signal with varying amplitude $x(t) = (1 + cos(2\pi 50t))cos(2\pi 1000t)$.

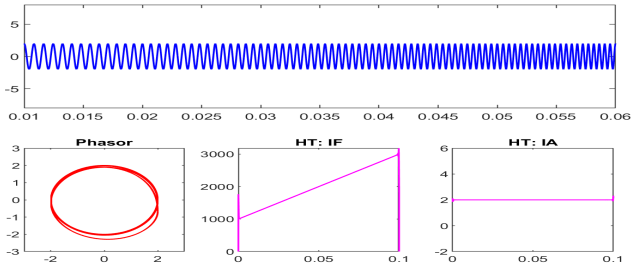

Figure 2.10: The complex phasor representation, instantaneous frequency and instantaneous amplitude resulting from the HT applied to a signal with increasing frequency $x(t) = 2cos(2\pi((z + 1000)t))$. z being the rate of frequency increase.

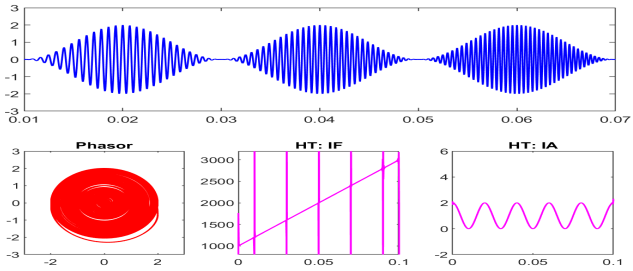

Figure 2.11: The complex phasor representation, instantaneous frequency and instantaneous amplitude resulting from the HT applied to a signal with increasing frequency and varying amplitude $x(t) = (1 + cos(\pi 50t))cos(2\pi((z + 1000)t))$. z being the rate of frequency increase.

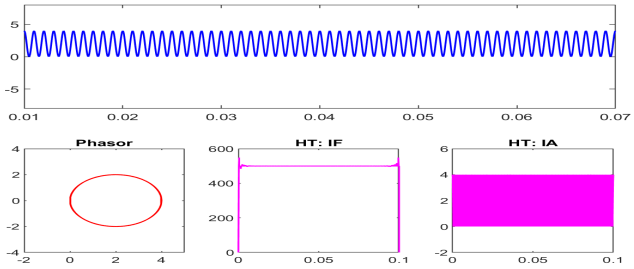

Figure 2.12: The complex phasor representation, instantaneous frequency and instantaneous amplitude resulting from the HT applied to a signal with offset $x(t) = 2 + 2cos(2\pi 1000t)$.

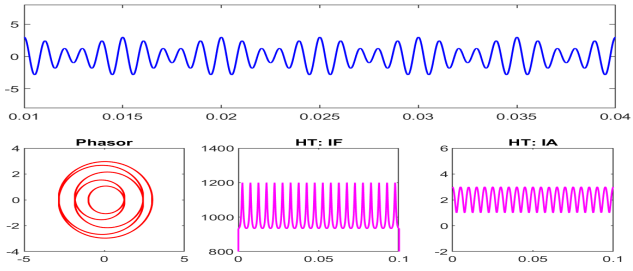

Figure 2.13: The complex phasor representation, instantaneous frequency and instantaneous amplitude resulting from the HT applied to two superimposed signals $x(t) = cos(2\pi 800t) + 2cos(2\pi 1000t)$

2.4 Empirical Mode Decomposition

The Empirical Mode Decomposition (EMD) is a data-driven time-series method capable of handling both non-linear and non-stationary signals. By considering oscillations on a local level, the method separates multi-component time-series into a finite set of modes, each representing zero-mean amplitude and frequency-modulated oscillations [20]. These modes are referred to as intrinsic mode functions (IMFs). Requiring no a priori defined basis system while fully capable of operating unsupervised, the method has proven to be highly effective [21, 22, 23]. However, due to its adaptive nature, the method lacks an analytical formulation, making theoretical analysis and performance evaluation challenging [24]. As mentioned in section 2.3, EMD is referred to as *Hilbert-Huang Transformation* (HHT) when used conjunction with the HT.

2.4.1 Intrinsic Mode Functions

An IMF is a function that satisfy two conditions [19]:

1. In the whole data set, the number of extrema and the number of zero crossings must either equal or differ at most by one.

2. At any point, the mean value of the envelope defined by the local maxima and the envelope defined by the local minima is zero.

The conditions limiting the IMFs are essential for defining a meaningful instantaneous frequency and amplitude. The symmetry concerning the local zero mean, enforced by requiring the mean of the envelopes constructed by local extrema to be zero, changes what traditionally used to be a global requirement to a local one [19]. This reduces asymmetries in the resulting waveform, further limiting fluctuations in the instantaneous frequency. To remove all unwanted fluctuations and asymmetries, one could enforce the ideal requirement of 'the local mean of the data being zero.' However, it is immediately evident that non-stationary signals would require a local time scale for each local mean, essentially being impossible to define [19]. However, using envelopes as an approximation to the ideal, in combination with the first requirement, which is the traditional narrow-band requirement for a stationary Gaussian process, an IMF is not restricted to a narrow band signal. Thus, an IMF can contain both amplitude and frequency modulation and can represent non-stationary signals [19].

2.4.2 The Sifting process

The process in which EMD decomposes a signal into a set of IMFs is referred to as *sifting*. The original signal $x(t)$ is thus represented by IMFs $x_n(t)$ and a residue $r(t)$, as can be seen in Equation (2.21)

$$x(t) = \sum x_n(t) + r(t) \tag{2.21}$$

The decomposition satisfies the perfect reconstruction property as superimposing all IMFs and residue reconstructs the original signal without any loss of information [20].

Sifting is illustrated in Figure 2.14, and Figure 2.15 shows the envelope and mean calculation for a given signal. The sifting process is summarized by the algorithm given below [25]

- Step 0: Initialize $n := 1, r_0 = x(t)$
- Step 1: Extract the n-th IMF accordingly:
  (a) Set $h_0(t) = r_{n-1}$ and $k := 1$
  (b) Identify all local maxima and minima of $h_{k-1}(t)$
  (c) Construct for $h_{k-1}(t)$ the upper envelope $U_{k-1}(t)$ defined by the maxima, and lower envelope $L_{k-1}(t)$ defined by the minima, by using a fitting interpolation method (traditionally cubic spline interpolation).
  (d) Determine the mean $m_{k-1}(t) = \frac{1}{2}(U_{k-1}(t) - L_{k-1}(t))$ of both envelops of $h_{k-1}(t)$
  (e) Set $h_k(t) := h_{k-1}(t) - m_{k-1}(t)$
    (i) if $h_k(t)$ does not satisfy IMF criteria, set $k \rightarrow k+1$ and repeat the process starting at point (b)
    (ii) if $h_k(t)$ satisfy the IMF criteria set $x_n(t) := h_k(t)$ and $r_n(t) := r_{n-1}(t) - x_n(t)$
- Step 2: If $r_n(t)$ represents a residue, stop the process; if not set $n \rightarrow n + 1$ and go to step 1.

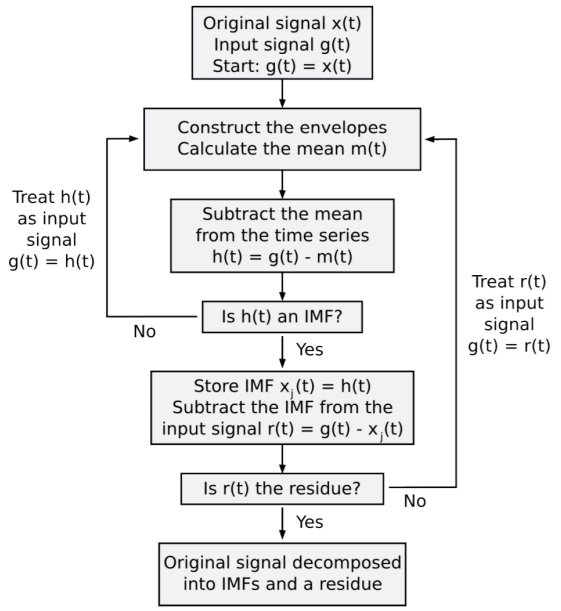

Figure 2.14: Flow diagram of the EMD algorithm [25].

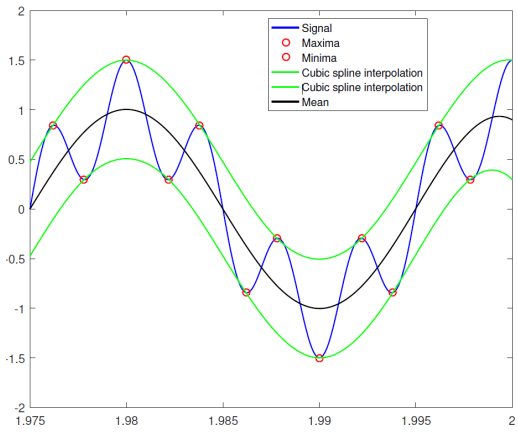

Figure 2.15: Example of the mean of a signal calculated by use of local envelopes based on local extrema.

EMD applied to a signal composite of three frequency components is illustrated in Figure 2.16. As expected the sifting process decomposes the signal into three different IMFs.

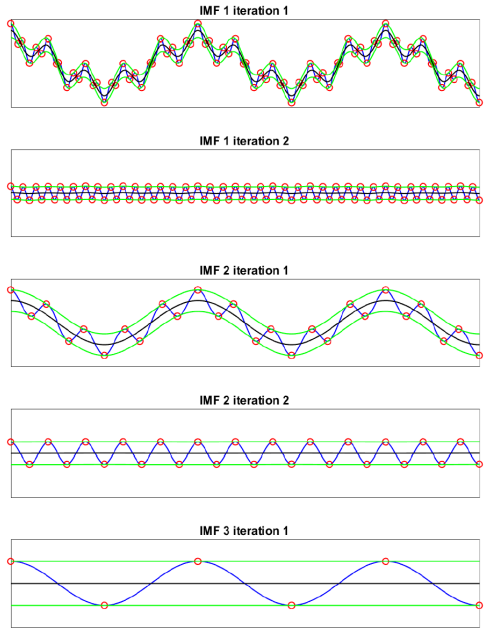

Figure 2.16: EMD applied to a signal composite of three different frequencies.

2.4.3 Stoppage Criteria

The sifting process serves two important functions; elimination of riding waves and smoothing of uneven amplitudes [19]. Riding waves is defined by [26]

> *In a singal, if there exists a local minimum greater than zero between two successive local maxima, or if there exists a local maximum less than zero between two successive local minima, the segment between these two successive local maxima (or local minima) is called a riding wave.*

The first function translates into ensuing meaningful instantaneous frequency, while the second function handles cases of large amplitude disparity between waves. While these functions are necessary for the decomposition and extraction of IMFs, they can when overused rob IMFs of their physically meaningful characteristics [19]. As such, a signal may be fragmented into physically meaningless IMFs that do not hold any relevance to the original signal. Therefore, it is necessary to determine a stoppage criterion for the sifting process that ensues the IMFs retain as much physical sense as possible while keeping the mean close to zero. Some commonly used stoppage criteria are given below [16]:

1. Specifying a fixed number of siftings
2. Stopping when x_n, or residue r_n, is smaller than a pre-set value.
3. Standard deviation (SD) between two consecutive siftings is smaller than a pre-set value.
4. Using an evaluating function*

The SD in the 3rd stopping criterion is often referred to as the Rilling stopping criterion and is given by:

$$SD = \sum_{t=0}^{T} \frac{|(h_{1(k-1)}(t) - h_{1k}(t))|^2}{h_{1(k-1)}^2(t)} \tag{2.22}$$

A typical value given for the SD is set between 0.2 and 0.3 [19].

*An evaluating function proposed by [24] uses thresholds θ_1 and θ_2. Defining a mode amplitude as in Equation (2.23) and an evaluating function as in Equation (2.24), sifting is performed while $\sigma(t) < \theta_1$ for a fraction of the signal duration $(1 - \alpha)$, and changes to $\sigma(t) < \theta_2$ for the remaining fraction. Thus the method handles globally small fluctuations while accounting for locally large excursions. Typical values for this method is $\alpha = 0.05$, $\theta_1 = 0.05$ and $\theta_2 = 10\theta_1$ [24].

$$a(t) := \frac{U(t) - L(t)}{2} \tag{2.23}$$

$$\sigma(t) := |\frac{m(t)}{a(t)}| \tag{2.24}$$

2.4.4 End effect and boundary conditions

The estimation of envelops $U(t)$ and $L(t)$ is a critical aspect of the EMD. As the IMFs are dependent on the mean calculated from these values, the technique used to connect extrema can have a tremendous impact on the decomposition quality of the EMD. The most common method used for connecting extrema is spline interpolation. Being piece-wise composed function of polynomial order n, splines are n-1 times differentiable at their knots acting as continuous functions [25]. The spline interpolation recommended by [19] is the *cubic spline*, as though computationally costly, it usually yields the best approximation of the signal envelopes [25]. In some situations, other types of interpolation may be better as the vital aspect is how well it is matched to the original signal.

Using spline interpolation to construct envelopes can cause mismatch at the boundaries of the signal, causing increasingly larger fluctuations as the error propagates through the IMFs [25]. The effect is caused by splines treating the first and last data points as knots for both the upper and lower envelope, resulting in a mean with no physical meaning when close to the ends of the signal [25]. As this mean is used for further extraction of IMFs, improper boundary condition can impact all subsequent IMFs extracted. Over-sifting will cause these errors to propagate further into their respective IMFs and can, if not handled, render the resulting IMFs useless. An example of a boundary condition error propagating through IMFs can be seen in Figure 2.17.

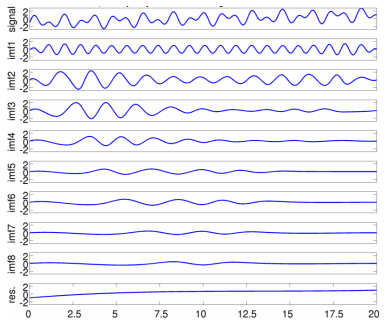

(a) EMD of the non-stationary time series $x(t) = sin(7t) + sin(4t) + 0.1t - 1$ with improper boundary conditions. Here the first and last data point of the time series have been treated as knots of x(t).

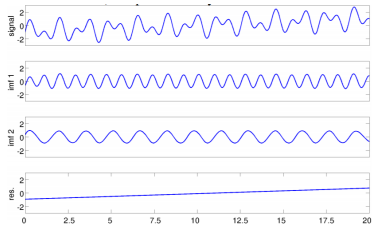

(b) EMD of time series given in **(a)** using proper boundary conditions.

Figure 2.17: Example of improper and proper boundary conditions [25].

2.4.5 Mode mixing

The inability to distinguish between closely spaced spectral components is a common issue in spectral analysis. This is also the case for EMD, as mode-mode mixing can cause problems when decomposing a signal into a set of IMFs. However, an important aspect of EMD is the IMFs representation of physically important characteristics in the original signal [27]. Therefore, it is necessary to be aware of situations in which the fragmentation

of a signal by EMD can cause the results to lose their physical meaning. An example of this is the human perception of tones. When presented with two tones sufficiently close in frequency, the ear will perceive these tones not as two separate entities but as a single tone modulated in amplitude. This effect is commonly referred to as the *beat-effect* and is shown in Figure 2.18. This can be expressed mathematically, as there is no difference in expressing $x(t) = cos(2\pi f_1 t) + cos(2\pi f_2 t)$ as $x(t) = 2cos\pi(f_1 - f_2)tcos\pi(f_1 + f_2)t$. As such, one can wonder if a decomposition into two modes yields a more accurate answer if the goal is a representation matched to perception rather than mathematics.

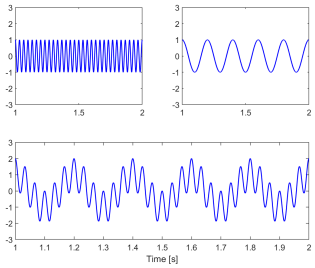

(a) Upper left: $cos(2\pi 30t)$. Upper right: $cos(2\pi 5t)$. Bottom: $cos(2\pi 30t) + cos(2\pi 5t)$

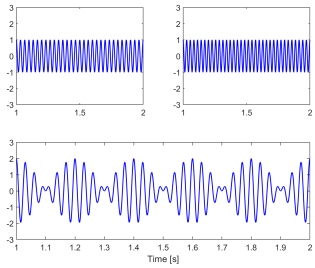

(b) Upper left: $cos(2\pi 30t)$. Upper right: $cos(2\pi 35t)$. Bottom: $cos(2\pi 30t) + cos(2\pi 35t)$

Figure 2.18: Beat effect — When the frequencies of the two superimposed tones are sufficiently far apart(left) the two-tones interpretation is meaningful. When they get closer(right), an interpretation in terms of a single tone modulated in amplitude is favored [27].

To maximize the potential of the EMD, it is necessary to know how and when it manages to retrieve individual tones, and when it considers input as a single tone. Even if a full decomposition is not accurate in a physical sense, a thorough understanding of the process can be useful for understanding complex signals.

Expressing a two-tone composite signal by Equation (2.25)

$$x[n] = a_1 cos(2\pi f_1 + \varphi_1) + a_2 cos(2\pi f_2 + \varphi_2), \quad f_1 > f_2 \tag{2.25}$$

It has been discovered in [27] that the behavior of the EMD will depend on the relative parameters $a \equiv \frac{a_2}{a_1}$,$f \equiv \frac{f_2}{f_1}$ and $\varphi \equiv \frac{\varphi_2}{\varphi_1}$. Thus the composite signal can instead be expressed as seen in Equation (2.26).

$$x(t; a, f) = cos2\pi t + acos(2\pi t + \varphi), t \in R \tag{2.26}$$

As the EMD extracts IMFs using a mean calculated by envelopes based on empirically located extrema, it seems rather intuitive that the EMD will notice only components impacting the final extrema in the superimposed signal. It is found in [27] that the contribution of extrema is dependent on parameters a and f. As there are three possible outcomes i.e., clean separation of modes, no separation of modes, and something in-between, the

relationship is divided into three outcomes. This has been extensively investigated in [27]. Below is a brief visualized recount of the findings reported.

Case 1: $af < 1$. If $af < 1$ the extrema rate in the superimposed signal is the same as the high frequency (HF) component. This is illustrated in 2.19(a)(a). By plotting the derivative of the HF component versus the opposite derivative of the LF component, each crossing represents an extremum in the superimposed signal. Thus, for each pair of extrema in the high amplitude HF component, there is exactly one crossing i.e., one extremum in the composite signal. As the HF component has a consistent impact on the superimposed signal, the EMD is fully able to detect and extract the HF component [27].
Case 2: $af > 1 \cup af^2 < 1$. If $af > 1 \cup af^2 < 1$ there is no regular pattern to the rate of extrema in the superimposed signal. Looking at 2.19(a)(b) there is no guarantee for a regular distribution of crossings. In this case, the EMD is *sometimes* able to detect the HF component resulting in IMF with partly separated modes.
Case 3: $af^2 > 1$ If $af^2 > 1$ the extrema rate is the same as the low-frequency component (LF). Thus, the EMD cannot detect the HF component, extracting it as a part of the LF component. This is illustrated in Figure 2.19(a)(c), as there is one extremum in the superimposed signal for each pair of extremum in the high amplitude LF component. Thus, the superimposed signal's extrema are only impacted by the LF component, hiding the HF component from the EMD.

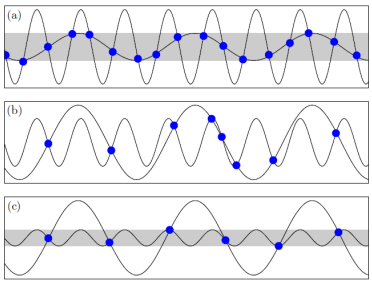

(a) Each graph plots the derivative of the HF component and the opposite derivative of the LF component, each crossing representing an extremum in the superimposed signal.

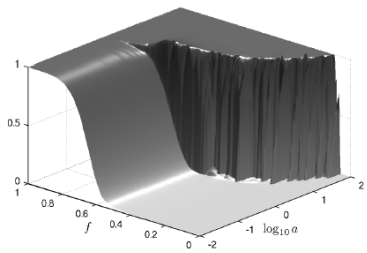

(b) A 3D representation of when mode-mixing appears in IMFs.

Figure 2.19: The mode-mixing criteria visualized [27].

A visualization of the complete relationship between a and f is shown in Figure 2.19(b). The ground level of the graph represents the complete separation of modes, while the top-level represents no decomposition. As the relationship between a and f changes, the degree of mode-mixing changes accordingly. Note that there is a drastic change in the EMDs' ability to distinguish closely spaced spectral components as the amplitude reaches a threshold value, while a change in frequency results in a more gradual decline in decomposition quality.

Mode mixing due to closely spaced spectral tones can be a problem when applying EMD

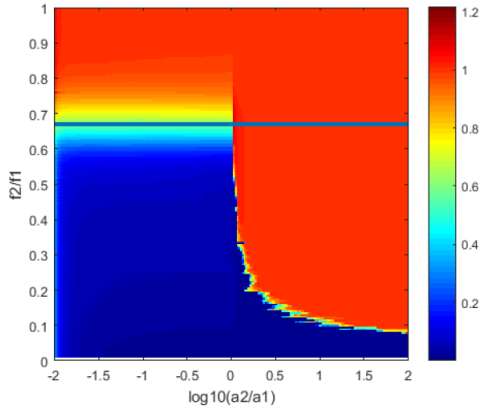

Figure 2.20: Boundary condition map for mode-mixing in EMD. Red area represent mode-mixing, blue area represent clean separation of two signals [28].

to complex signals. A method for mode mixing separation is presented in [28]. By utilizing a 2D projection of the amplitude and frequency ratios given in a *Boundary Map* [28] depicted in Figure 2.20 it is possible to construct a *masking singal* $f_m(t)$ that will mix with *one* of the tones involved in a mode mix. Adding the masking signal to the original signal will result in a controlled artificial mode mixing, causing the extraction of a mode mixed IMF containing the masking signal and the intended mode. This removes the intended mode from the previous mode-mixed signal, leaving a pure IMF. Furthermore, as the masking signal characteristics are known, it can be easily removed from the new mode-mixed IMF by averaging the results of the EMD with a separate EMD using the opposite masking signal. This process is depicted in Equation (2.27) to (2.4.5).

$$x_+(t) = x(t) + f_m(t) \tag{2.27}$$

$$x_-(t) = x(t) - f_m(t) \tag{2.28}$$

$$x(t) = \sum \frac{x_{n,+}(t) + x_{n,-}(t)}{2} + r(t) \tag{2.29}$$

2.5 Real-time Empirical Mode Decomposition

Though the EMD is a sophisticated method with clear advantages over other empirical decomposition techniques, which are often limited due to conditions that only apply approximately in certain situations [20], there are two apparent shortcomings. First, due to the empirical nature of the method, time series with a high sampling rate over a long duration, i.e., large amounts of data, can be a challenge. Current EMD techniques and computational capacities limit the complete analysis of large amounts of data requiring the segmentation of large data streams. Second, the traditional analysis requires the complete data set, thus the need to wait until the data collection is finished. This is indeed quite limiting if applying EMD for use in the power system as surveillance and diagnostic of current and voltage often requires a high sampling rate and real-time tracking. Thus, there is a need for a real-time version of the EMD capable of handling large amounts of data. In this section, two such methods are presented. These being the weighted sliding Empirical Mode Decomposition (wSEMD) [20] and its extension, the Online EMD [29].

2.5.1 Weighted Sliding Empirical Mode Decomposition

To handle the problem of computer memory and load when dealing with time series of considerable length, one could propose clean segmentation of the data stream. By separating the data into several distinct segments, applying EMD to each segment would significantly reduce the computational load. However, due to the boundary condition effect on the EMD, the resulting IMFs would have discontinuous and boundary condition errors propagating in the IMFs, as shown in Figure 2.21.

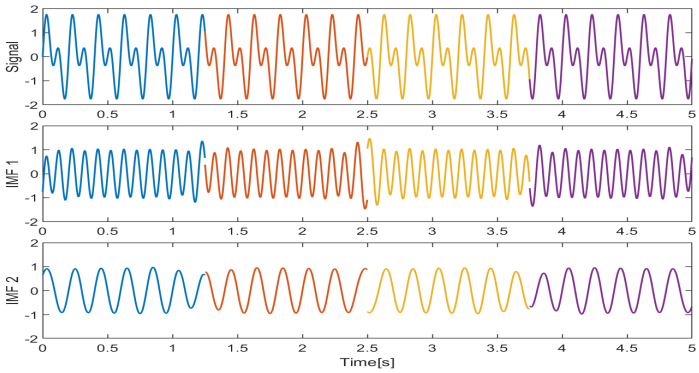

Figure 2.21: EMD decomposition of synthetic signal $x(t) = cos(2\pi 10t) + cos(2\pi 5t)$. The series has been decomposed into four equal segments each with a separate EMD indicated by the color scheme. After adding the resulting IMFs, there are clear boundary errors at t = 1.25, 2.5 and 3.75.

SEMD preforms the traditional EMD or EEMD within a fixed window of size m, shifting the window forward with step size k applying EMD for each shifting until the whole time series has been covered [20]. Both m and k are chosen apriori, and should satisfy Equation (2.30) and (2.31) to avoid discontinues as in Figure 2.21 and to keep the window a multiple

of the step size.

$$k < m \tag{2.30}$$

$$E = \frac{m}{k} \in \mathbb{N} \tag{2.31}$$

This ensures that, if omitting the first *m* points, there will be *E* estimations for each point in the original time series *x(t)* for each window m_i. These estimated values may vary due to the boundary effect on each separate EMD, thus the mean value of each estimation is taken as the result of the SEMD. Given *j* IMFs for each segment m_i the original time series is decomposed into *j* different IMFs $x_{m_i}(t)$ and a residue $r_{m_i}(t)$ as can be seen in Equation (2.32).

$$x_{m_i}(t) = \sum x_{m_i j}(t) + r_{m_i}(t), \tag{2.32}$$

Each IMF is then collected in a matrix of E columns such that each value in a given column corresponds to the same point in the original time series. As averaging the amplitudes for each respective point in the IMFs requires an equal amount of data in each column, the columns related to the beginning and end of the times series are not included in further calculations. This algorithm is illustrated in Figure 2.22. For each point *t* a mean value is calculated such that for $t > m$

$$x_j(t) = \frac{1}{E} \sum_{i}^{i+E-1} x_{m_i j}(t) \tag{2.33}$$

$$r(t) = \frac{1}{E} \sum_{i}^{i+E-1} r_{m_i}(t) \tag{2.34}$$

$$i = \frac{t-m}{k} + 2 \tag{2.35}$$

The resulting functions $x_j(t)$ are referred to as SIMFs and $r(t)$ as the sliding residuum [20]. As averaging is used to calculate the resulting SIMFs, the number of IMFs uncovered in each window needs to be constant. i.e., chosen apriori and the and stoppage criterium is consequently limited to a fixed amount of siftings.

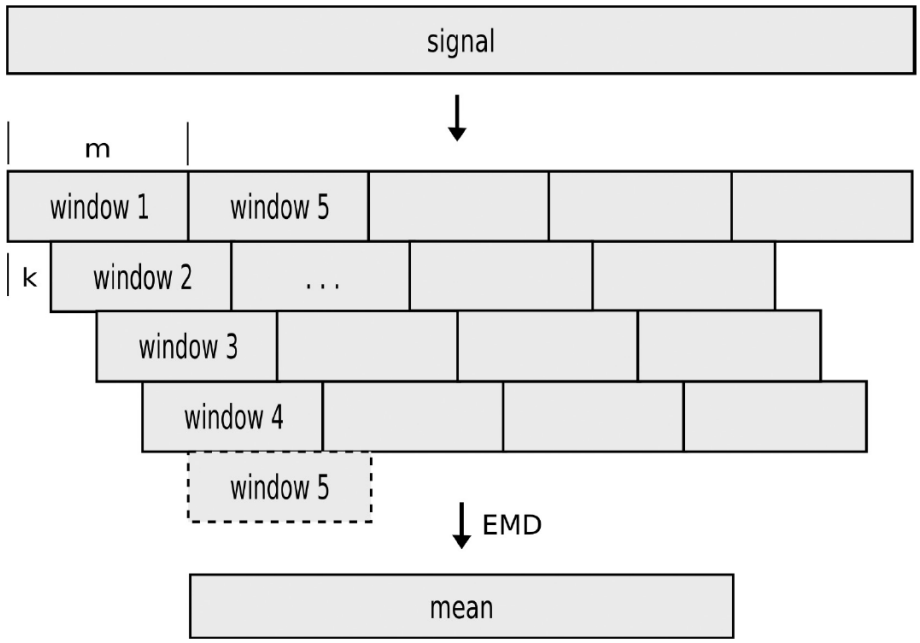

Figure 2.22: Schema of the SEMD algorithm [20]

Though averaging the resulting IMFs from each step does hinder discontinues and reduce error, the resulting SIMFs are still affected by the boundary conditions. As illustrated in Figure 2.23, the ends of each IMF is significantly more defective when compared to the rest of the signal.

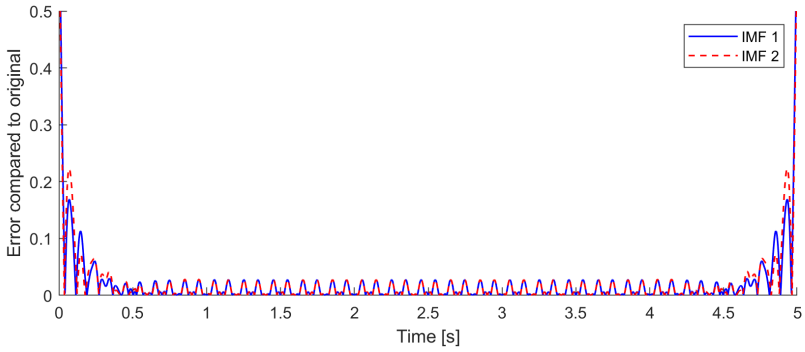

Figure 2.23: Error in resulting IMFs given signal as in Figure 2.21

This is usually not a severe problem using traditional EMD. However, when a time series is segmented, each segment has individual ends contributing to the boundary condition

errors. The contribution of each segment's ends is reduced by introducing a weighted sum of each estimate. This is done by multiplying the IMFs and residue from every window by a vector of rank *m* generated from a Gaussian distribution [20].

$$w(n) = exp\left(-\frac{1}{2}\left(\alpha\frac{2n}{N}\right)^2\right) \tag{2.36}$$

$$-\frac{N}{2} \leq n \leq \frac{N}{2}, \quad \alpha = 2.5, \quad N = m - 1 \tag{2.37}$$

The resulting averaged weighted point in an arbitrary IMF is calculated by taking the sum of *n* estimates multiplied by *n* weighting coefficients. The result is then normalized by the reciprocal of the sum of all used weights [20]. This preserves the amplitude of every SIMF and residue while ensuring the completeness of the decomposition. Using SEMD in combination with weighting coefficients is refereed to as wSEMD.

2.5.2 Online Empirical Mode Decomposition

While the method of wSEMD presented in section 2.5.1 solves some of the problems related to the classical EMD, it severely limits the potential of the underlying method. By determining the explicit number of IMFs extracted from any given time series and only using a fixed number of siftings as stoppage criteria, wSEMD weakens the prime benefits of the EMD; the ability to discover intrinsic components in an unexplored signal [29] empirically. An alternative method is the Online EMD proposed by Fontugne et al. in 2017. Based on the sliding approach seen in wSEMD, Online EMD extracts, and uncovers oscillations without any prior knowledge. Keeping the advantages of lower computational strain and memory requirement of the wSEMD, Online EMD can use any of the stoppage criteria mentioned in Section 2.4.3.

By utilizing a sliding window covering *l* local extrema, Online EMD operates as the classical EMD within this frame by extracting the fastest oscillating component. Shifting the window forward by one extremum, the next extracted mode is stitched to the previously extracted mode overlapping with the current window. As in wSEMD, a weighting factor is utilized to limit the contribution of boundary condition errors in each segment, and further average the resulting modes. The stitching procedure uses a window function as $\tilde{\phi}_w(s)$ as can be seen in Equation (2.38) that prevents discontinuities due to boundary errors [29]. An overview of Online EMD sliding window and stitching procedure can be seen in Figure 2.24

$$\tilde{\phi}_w(s) = \begin{cases} \tilde{\phi}(s) = \frac{1}{\sqrt{2\pi}} exp\left(-\frac{s^2}{2}\right) - \frac{1}{\sqrt{2\pi}} exp\left(-\frac{\tau^2}{2}\right), & \text{for s} \in [-\tau, \tau] \\ 0, & \text{otherwise} \end{cases} \tag{2.38}$$

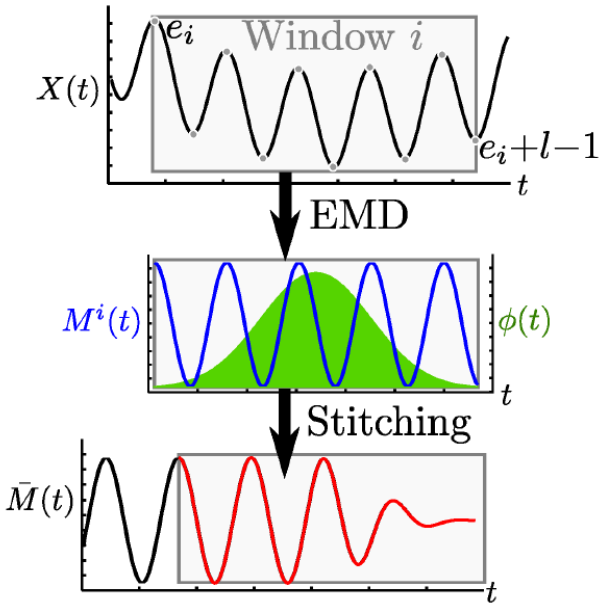

Figure 2.24: Overview of Online EMD sliding window and stitching procedure. In this case, the l = 10 extrema, M^i given by the blue signal, represents the fastest oscillation and is extracted using the classical EMD. The window function $\phi(t)$ is plotted in green, and the resulting weighted IMF, $\bar{M}$, stitched to the previous uncovered IMFs is red. Note that here $l' = l$ [29].

The complete algorithm for Online EMD is as follows [29]:

0. Initialize $i = 1, \Phi^0(t) = 0, e_1 = 0$ the starting time of the signal and $M = 0$.
1. Identify the window starting at e_1 containing *l* consecutive local extrema ($\{e_1, ...e_l\}$) of the signal $X(t)$.
2. Using classical EMD, extract the first IMF (i.e. fastest oscillation) $M^i(t)$ of the data in the window.
3. Let $e_1^{'}, ..., e_l^{'}$ be the positions of the $l^{'}$ extrema in M^i. Set $s_k = -\tau + 2(k+1)\tau/(l^{'} - 1)$ for $k \in \{1, .., l^{'} - 1\}$. We define warped weights $\phi_k(t)$ for $k \in \{1, ..., l^{'} - 1\}$ and t $\in [e_k^{'}, ..., e_{k+1}^{'}]$ as

$$\phi_k(t) = \tilde{\phi}\left(s_k + (s_{k+1} - s_k)\frac{t - e_k^{'}}{e_{k+1}^{'} - e_k^{'}}\right) \tag{2.39}$$

(and 0 outside). The weighted IMF $\hat{M}^i$ is defined as: $\hat{M}^i = (\phi_1(t)M_1^i(t), ..., \phi_{l^i-1}(t))$ where $M_k^i(t)$ is the mode between two extrema:

$$M_k^i(t) = M^i(t), \quad e_k^{'} \leq t \leq e_{k+1}^{'} \tag{2.40}$$

The total of the weights is kept in memory:

$$\Phi^i(t) = \Phi^{i-1}(t) + \sum_{k=1}^{l^{'}-1} \phi_k(t) \tag{2.41}$$

4. Stitch $\hat{M}^i$ on the weighted IMFs already extracted:

$$\bar{M} = \bar{M} + \hat{M}^i \tag{2.42}$$

and normalize the part of the data that will go out of the sliding window at the next iteration:

$$\bar{M}(t) = \bar{M}(t)/\phi^i(t) \quad \text{for all } t \in [e_i, e_{i+1}] \tag{2.43}$$

5. This newly finalized part of the IMF $\bar{M}(t)$, for $t \in [e_i, e_{i+1}]$ is subtracted from the data,

$$R^i = X^i(t) - \bar{M}(t) \quad \text{for all } t \in [e_i, e_{i+1}] \tag{2.44}$$

The resulting data R^i is pushed to another instance of Online EMD in order to identify subsequent IMFs.

6. Increase i to $i + 1$ and go back to step 1.

It is worth noting that given the nature of the stitching process and dependence on subsequent extrema, IMFs will have a time lag of $e_{i+l-1} - e_i < \Delta t < e_{i+l} - e_i$. The time lag Δt will increase for lower frequency IMFs as the distance between extrema increases. Furthermore, it is also worth noting that in step 3. and 4. there is a difference in the notation for the number of extrema in the IMF $l^{'}$ and the number of extrema defining the sliding window l. Though rare, situations were small and fast oscillations are added to larger slow oscillations can cause some of the smaller extremas to go unnoticed in the superimposed signal. These can however be recovered by the EMD and will lead to new extrema in the extracted IMF. Thus the need for a distinction between $l^{'}$ and l.

The clear advantage of the Online EMD is the ability to analyze data streams with constant execution time. This is shown in [29] where two signals, a sinusoid with a monotonic function and a white noise signal is used to compare the execution time for both the classical and Online EMD. Each total signal consists of 280K samples divided into 10K batches. As more points are ”released” into the stream, classical EMD is shown to slow down significantly, while online EMD keeps a steady execution time. The complete comparison, as all points are added, can be seen in Figure 2.25. As expected, the online EMD keeps each stream separate and does not need to rely on previous information for new analysis. As can be seen in Figure 2.25, the classical EMD requires four times more execution time from beginning to end for the sinusoidal signal, and a whole four orders more for the white noise signal. There is also a difference in execution time dependant on the number of uncovered IMFs. While the stitching and sliding window makes online EMD slower than classical for fewer than 130K samples, it easily outperforms classical EMD for larger data sets with an increasing number of oscillatory components [29] as indicated by the white noise signal in Figure 2.25.

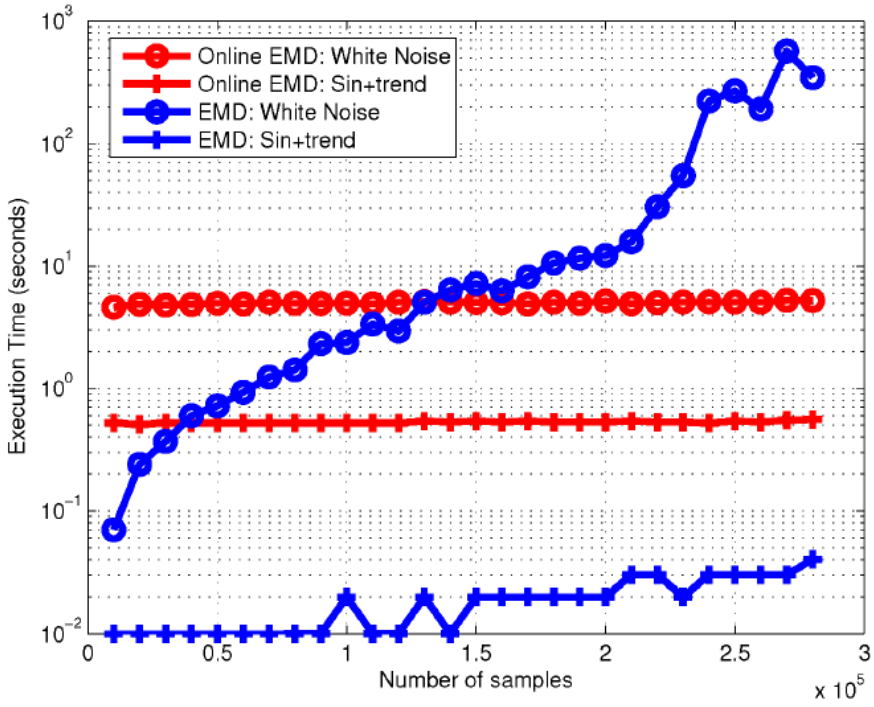

Figure 2.25: Execution time of Online EMD ($l = 20$) and classical EMD (both using Rilling stopping criterion) with a white noise signal and a sinusoid with a trend [29].

Chapter 3

Comparison of classical and Online EMD using synthetic signals

In this section comparison of the decomposition quality of the classical and Online EMD is done through synthetic signals. Two separate signals have been constructed, both a mix of three tones, one with an additional Gaussian white noise disturbance. Classical EMD is applied for both cases, using three different stoppage criteria. The instantaneous error and root-mean-square (RMS) error are then calculated for each relevant IMF uncovered. As the amplitude of the components are different, a weighted and averaged error for all three IMFs are used when comparing results. Using the stoppage criteria with lowest error in the classical EMD, online EMD is applied for window sizes $l = [10, 30]$. The version of Online EMD used is based on the MATLAB implementation of Online EMD as given in the ICASSP'17 paper [29] accessible at [30].

3.1 Case 1: Standard

The signal used in this case can be seen in Figure 3.1 and is given by

$$f(t) = f_1(t) + f_2(t) + f_3(t) \tag{3.1}$$

where

$$f_1(t) = 70cos(2\pi 150t) \quad f_2(t) = 100cos(2\pi 50t) \quad f_3(t) = 20cos(2\pi 20t) \tag{3.2}$$

The three following stoppage criteria has been chosen.

1. SD = 0.01
2. $\alpha = 0.001 \quad \theta_1 = 0.001 \quad \theta_2 = 0.01$
3. FIX = 10

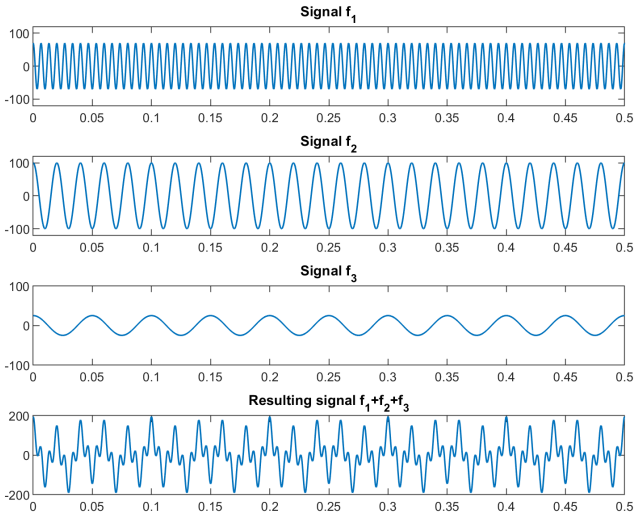

Figure 3.1: Signal consisting of three different amplitudes and modes of oscillations.

The resulting IMFs extracted and following error calculation can be seen in Figures 3.2, 3.3 and 3.5. Each criterion successfully uncovered the three components without a trace of mode mixing. This is to be expected as the ratios of frequency and amplitude in the signals are well within the limits of the Boundary Condition Map given in Figure 2.20 from [27]. However, boundary condition errors can be observed for all cases, as seen in the *Error compared to synthetic* graph. To exclude the error of this border effect the RMS error is calculated omitting the first and last 0.5 seconds of the signal. As can be seen in Figures 3.2 to 3.5, criteria 2 and 3 outperform criteria one significantly in both average RMS value and boundary condition error, the latter being almost double the value of the other criteria. It is however stoppage criteria FIX = 10 yielding the best overall results. This method is thus used as the stoppage criteria for the Online EMD for further analysis and comparison. The resulting Online EMD is treated the same as the classical EMD; thus, the first and last 0.5 seconds of the signal is omitted for the RMS error calculation. A summary of the average calculated RMS for window sizes $l = [10, 30]$ compared to the classical EMD for each stoppage criteria can be seen in Figure 3.6.

The stitching procedure responsible for merging each local IMF to a resulting final IMF is a potential new source of error for the Online EMD when compared to the classical version. Intuitively, the number of overlapping IMFs (i.e., widow size) is a determining factor for this error. It is observed in Figure 3.6 that this error significantly reduces as l increases for small values of l and even outperforms the classical EMD in the case $l = 13$. This is consistent with the results in [29], though it reported a significantly lower error for the first window sizes. As the window size increases, the RMS error appears to converge to the same error as in the classical EMD using the same stoppage criteria.

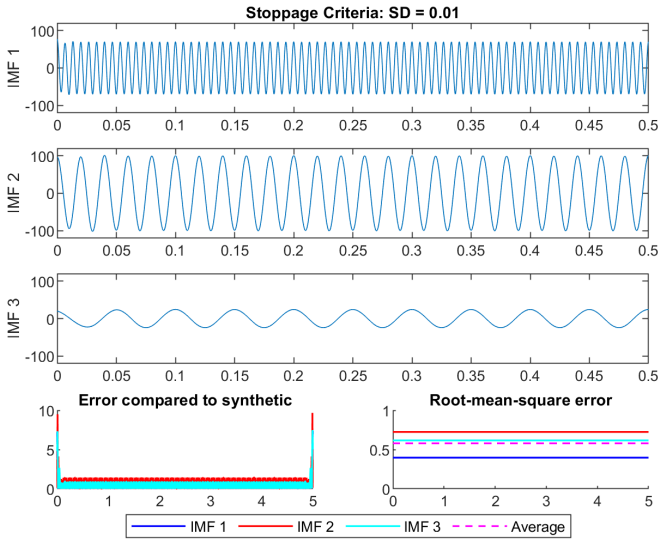

Figure 3.2: EMD with stoppage criteria SD = 0.01. Overall and rms error is calculated for each extracted IMF.

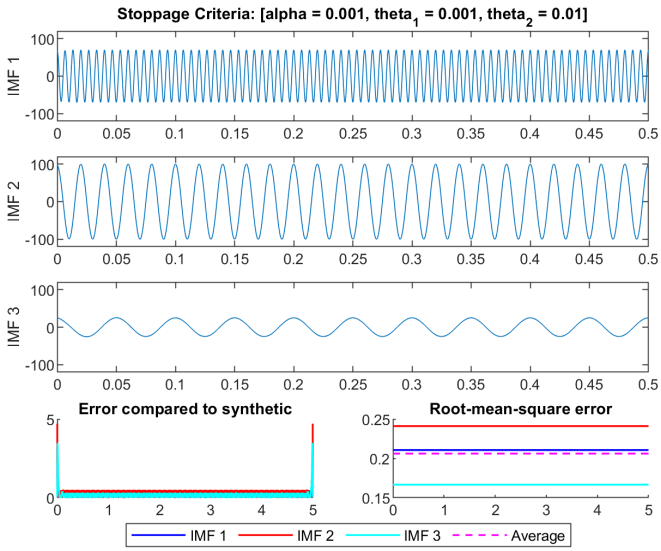

Figure 3.3: EMD with stoppage criteria $\alpha = 0.001 \quad \theta_1 = 0.001 \quad \theta_2 = 0.01$. Overall and rms error is calculated for each extracted IMF.

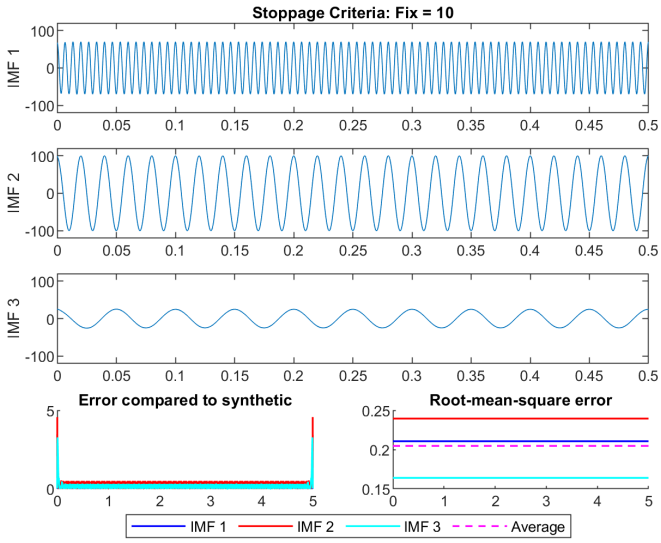

Figure 3.5: EMD with stoppage criteria FIX = 10. Overall and rms error is calculated for each extracted IMF.

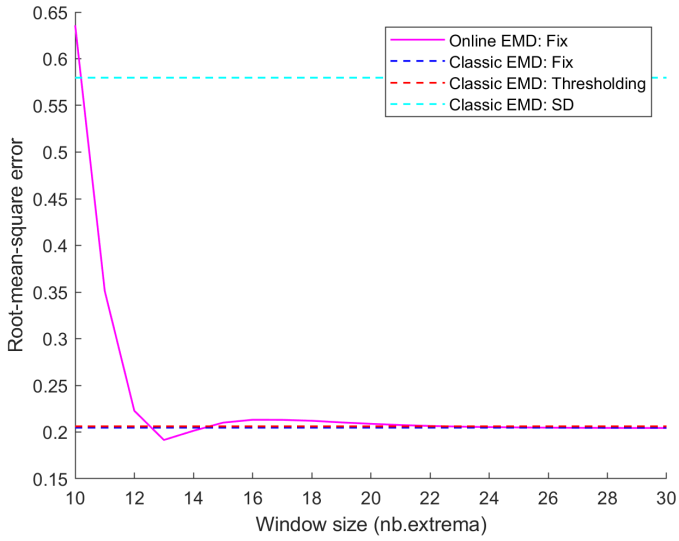

Figure 3.6: Average root-mean-square error for all IMFs as the widow size increases for the Online EMD.

3.2 Case 2: Gaussian white noise

To further test the robustness of the classical and Online EMD in the event of disturbances, a second case has been constructed. Here the signal, as seen in Figure 3.1, is used as the base with an additional Gaussian white noise component such that the resulting signal is as can be observed in Figure 3.7. To evaluate and compare the quality of decomposition of both classical and Online EMD, the process and stoppage criteria used in the previous case are repeated. However, due to the disturbances, FFT is used as an additional tool to support the evaluation.

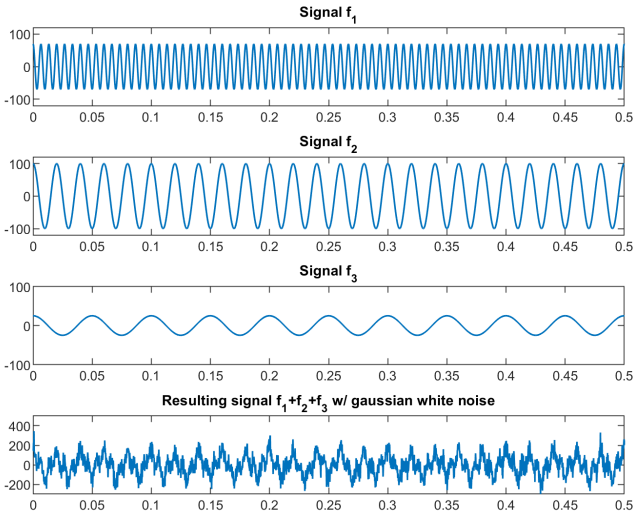

Figure 3.7: Signal consisting of three different amplitudes and modes of oscillations with a added Gaussian white noise component, matched to scale by the MATLAB awgn('measured') command.

3.2.1 Stoppage Criteria: Standard Deviation

The decomposition using $SD = 0.01$ can be seen in Figure 3.8. The noise component has a significant impact on decomposition quality. Using FFT as seen in Figure 3.9 the first three IMFs appear to have a denoising effect as they contain the high frequencies not included in the three signals f_1, f_2 and f_3. Furthermore, the fifth and sixth IMF appear to be a separation of the same mode, likely due to mode mixing with low-frequency noise components. It is deemed acceptable to use the result of adding these IMFs as a resulting IMF, as this is a non-invasive method used to improve the decomposition quality without altering the actual EMD. The resulting IMFs and error can be seen in Figure 3.10. The error has increased significantly compared to case 1, and as can be seen from the resulting IMFs, there are severe disturbances in both frequency and amplitude. However, while instantaneous values are somewhat lacking, using FFT as a supportive tool makes it

possible to get an overall impression of the components mixed in the signal, with regards to both amplitude and frequency.

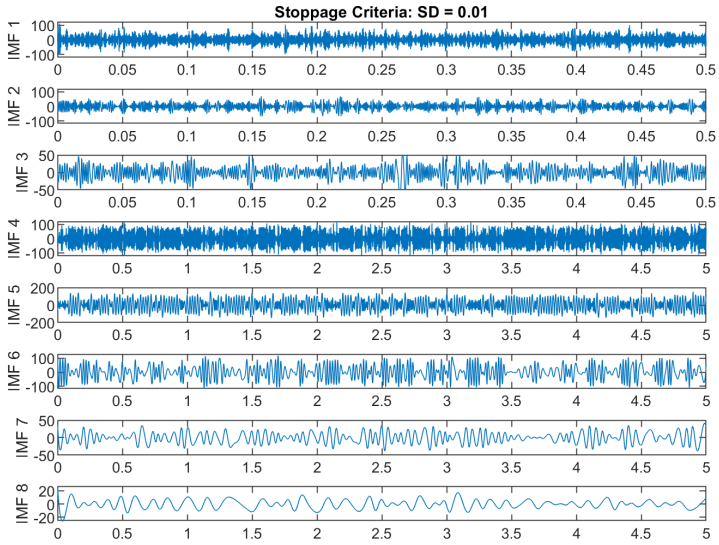

Figure 3.8: The first 8 IMFs from using the stoppage criteria $SD = 0.01$.

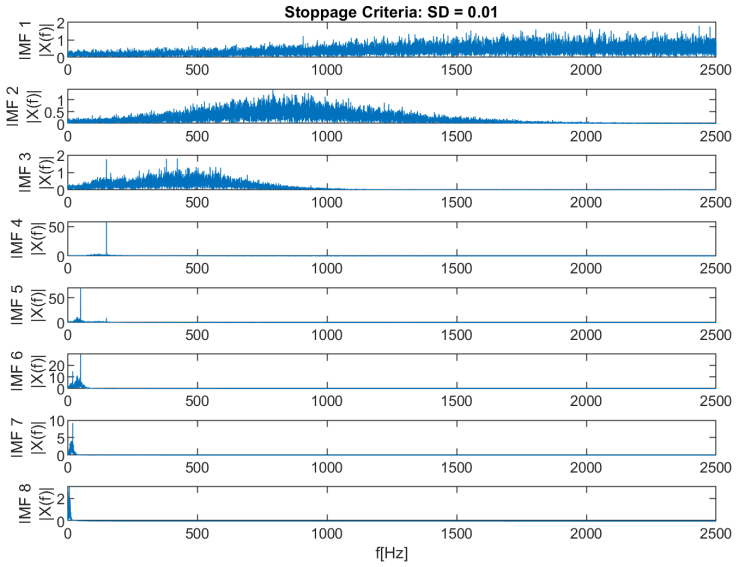

Figure 3.9: FFT of the first 8 IMFs using the stoppage criteria $SD = 0.01$.

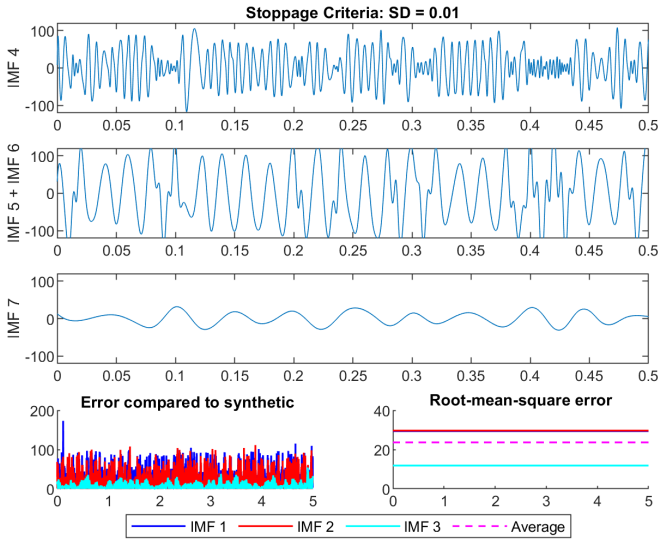

Figure 3.10: EMD with stoppage criteria $SD = 0.01$. Overall and rms error is calculated for each extracted IMF.

3.2.2 Stoppage Criteria: Thresholding

The decomposition using stoppage criteria $\alpha = 0.001 \quad \theta_1 = 0.001 \quad \theta_2 = 0.01$ can be seen in Figure 3.11. Applying FFT to the IMFs as seen in Figure 3.12 it is apparent the three first IMFs contain most of the noisy components in the signal. As with the SD criteria, it is possible to use EMD as a denoising tool. Observing the FFT and IMFs, the IMFs deemed to represent the same modes of oscillation have been added together in the resulting IMFs, as seen in Figure 3.13. Though the average RMS error is seen to be slightly lower than that of the SD condition, the instantaneous values of both frequency and amplitude in all three IMFs are distorted enough to not accurately represent the original modes. The most significant contribution to this error appears to be the mode-mixing due to the lower frequency noise components, as the high-frequency components are handled as separate IMFs. This can be most notably observed in IMF 6 and IMF 7 in Figure 3.3. Periodic reduction in amplitude in IMF 6 has a matching increase in amplitude in IMF 7 for the same mode of oscillation, IMF 6 is thus leaking somewhat into IMF 7. Though there are techniques capable of handling this occurrence to some extent, they are, in this instance, deemed too invasive, as the focus is on the robustness of the method itself.

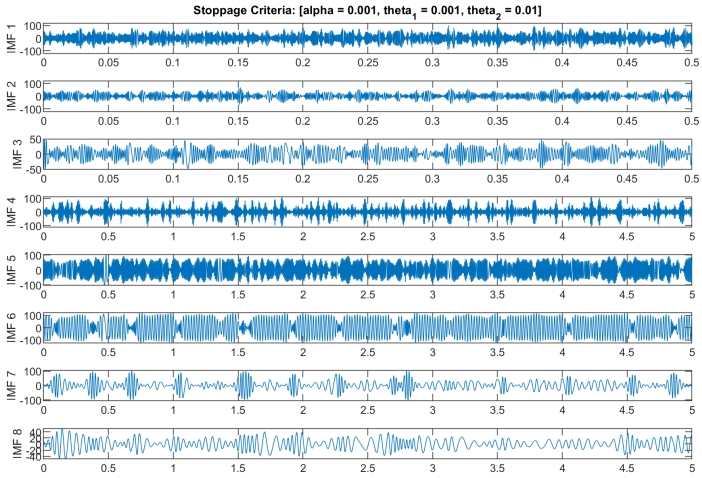

Figure 3.11: The first 8 IMFs from using the stoppage criteria $\alpha = 0.001 \quad \theta_1 = 0.001 \quad \theta_2 = 0.01$.

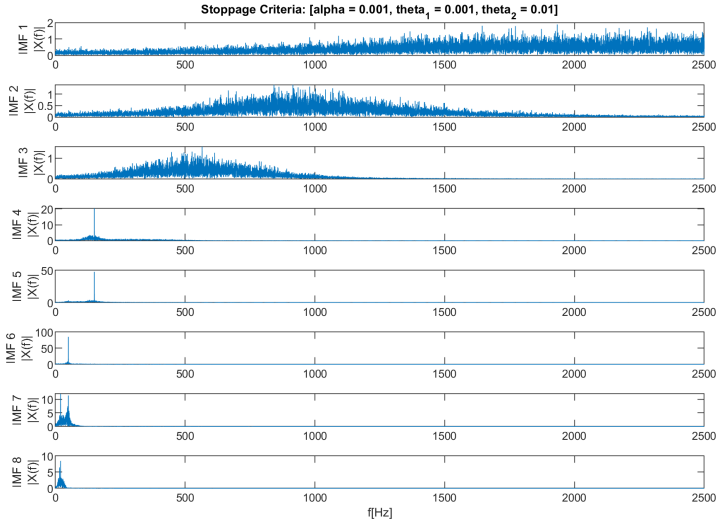

Figure 3.12: FFT of the first 8 IMFs using the stoppage criteria $\alpha = 0.001 \quad \theta_1 = 0.001 \quad \theta_2 = 0.01$.

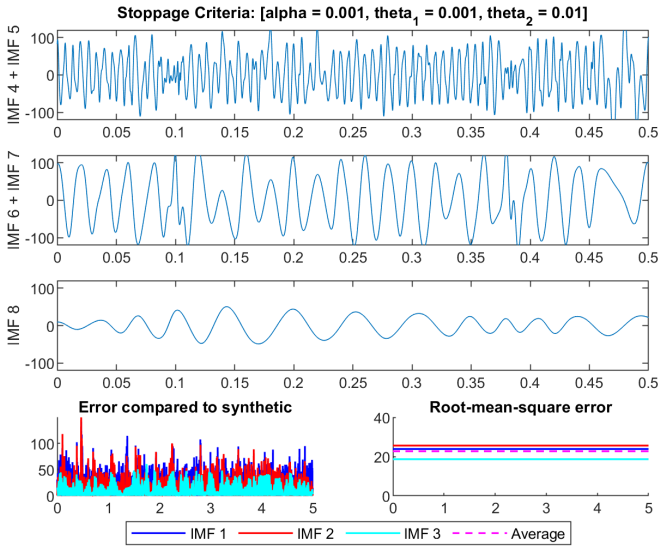

Figure 3.13: EMD with stoppage criteria $\alpha = 0.001 \quad \theta_1 = 0.001 \quad \theta_2 = 0.01$. Overall and rms error is calculated for each extracted IMF.

3.2.3 Stoppage Criteria: Fix

The decomposition using stoppage criteria FIX = 10 can be seen in Figure 3.14. The resulting FFT of each IMF can be seen in Figure 3.15. It appears that this stoppage criterion handles the noise significantly better than the previously used criteria. As can be seen from the FFT and IMFs, the fifth IMF represents f_2 surprisingly well. However, using FFT as a supportive tool, IMF 3 and IMF 4 have been added to the resulting IMF as this gives a slightly reduced error. As can be seen in Figure 3.16, the average RMS error is noticeably lower than that of the previous stoppage criteria. This is mostly due to the fifth IMF accurately representing the 50 Hz component. Thus, using a fixed number of siftings is the most robust when dealing with noisy components (without changing criteria). This could be due to the number of siftings being constant, while both SD and thresholding are more dynamic stoppage criteria and thus more susceptible to change as the number of siftings can be different for each IMF based on the nature of noise added.

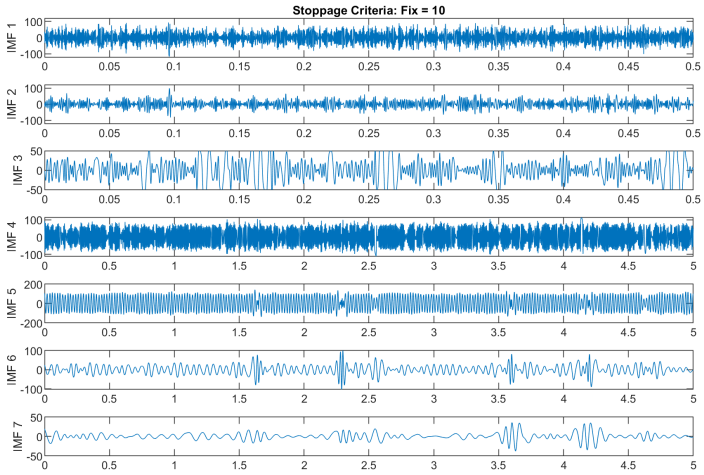

Figure 3.14: The first 7 IMFs from using the stoppage criteria FIX = 10.

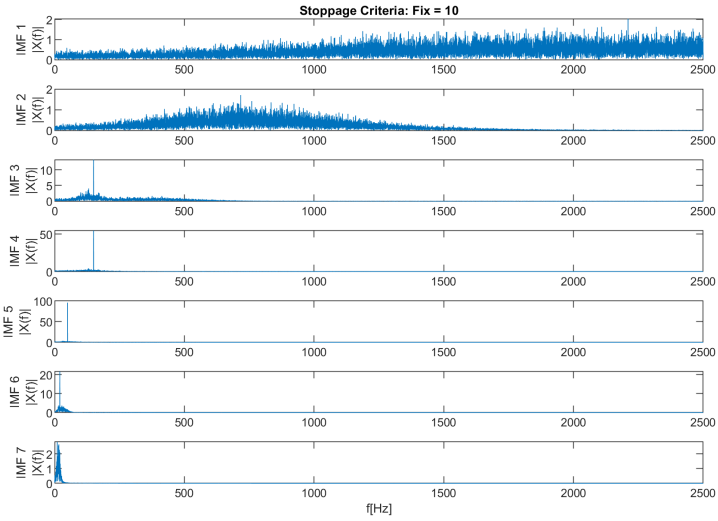

Figure 3.15: FFT of the first 7 IMFs using the stoppage criteria FIX = 10.

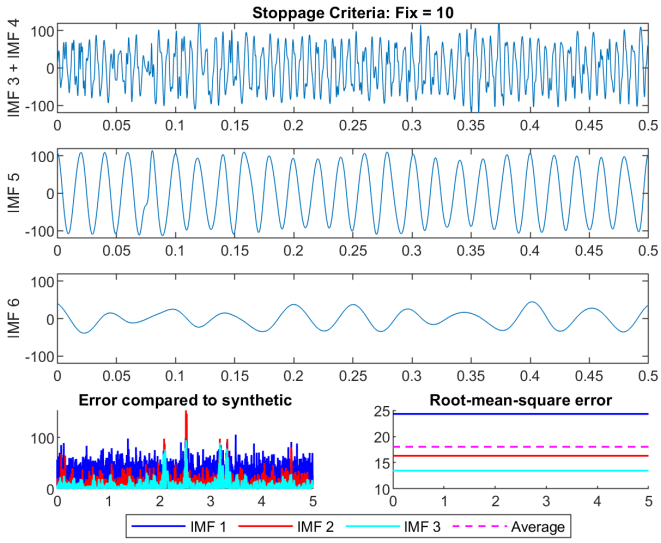

Figure 3.16: EMD with stoppage criteria FIX = 10. Overall and rms error is calculated for each extracted IMF

3.2.4 Online EMD

As FIX = 10 gave the best result for classical EMD, it has been used as the stoppage criteria for Online EMD. To test the effect of noise on the stitching process window sizes $l = [10, 30]$ have been used for average RMS error calculations, as the decomposition quality is a function of window length, which again is a function of the stitching process. The resulting IMFs with $l = 10$ can be seen in Figure 3.17. As with the classical implementation of EMD with FIX = 10, the 50 Hz component represented by IMF 5 is most noticeably similar to its original component f_2. However, IMF 3 and 4, as well as IMF 6 and 7, have been added to represent f_1 and f_3, respectively. A summary of the results with $l = [10, 30]$ can be seen in Figure 3.18. Surprisingly online EMD has better performance for lower values of l than the corresponding classical EMD. This may be due to the smoothing effect of the stitching as an averaging of the values is used, essentially reducing the impact of a typical white noise disturbance. The error is however, seen to significantly increase as l increases. Though the exact cause for this is unknown, it can be argued that this is due to the smoothing effect's trade-off and the stitching process being skewed as the window size increases. However, overall the Online EMD seems to keep the same robustness as the classical version. Furthermore, while not the intent for this comparison, using FFT as an additional tool when applying EMD to complex signals is seen to be highly effective.

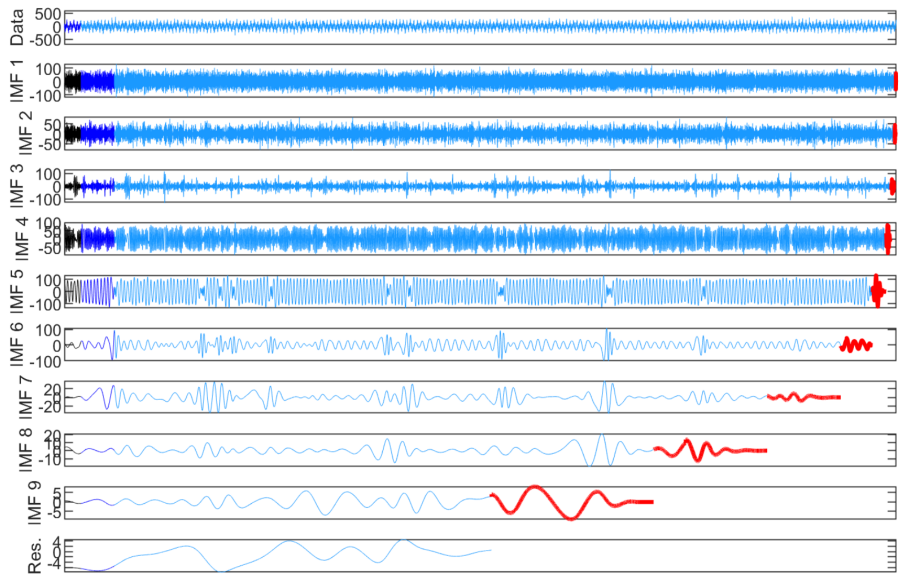

Figure 3.17: Online EMD with FIX = 10 as stoppage criteria. The red parts represents the section of the IMFs not yet completed due to lacking number of extrema.

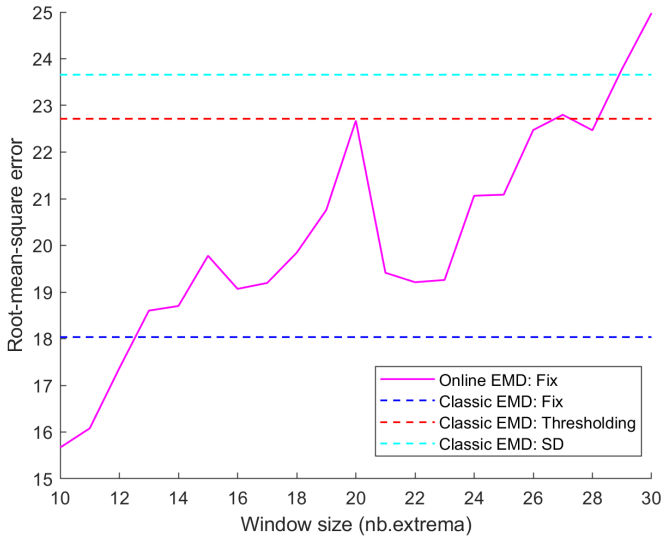

Figure 3.18: Average root-mean-square error for all IMFs as the widow size increases for the Online EMD.

Chapter 4

Frequency Identification in a Wind Turbine Through HHT and Online EMD

This section presents the results and methodology from analyzing an actual voltage and current measurement from a wind-turbine. Due to the high complexity of each signal, and the dominating presence of a 50 Hz component, careful separation of each mode is needed for a complete view of the harmonic interference. By using classical EMD and Online EMD in conjunction with FFT and a reconstructed boundary condition map [27], the mode mixing separation method suggested in [28] is used to separate the original signal into adequately pure IMFs. As IMFs are uncovered, they are removed from the original signal, and the process is repeated until all relevant modes are extracted. Each resulting IMF is then analyzed using HT and FFT, and the results of classical and Online EMD are compared. The IMFs extracted are now referred to by the value of their most dominating frequency component. A cubic spline and a fix of 10 has been used as stoppage criteria for both versions of EMD, as this yields the most consistent results.

4.1 Signal specifics

The signals analyzed are the three-phase line currents and line-to-line voltages of a wind-turbine generator located at Hundhammerfjellet windmill park. The currents and voltages are shown in Figure 4.1 and 4.2 respectively. The measurements were taken the 8^{th} of October 2014 from 23:34:02 to 23:34:06 with a sampling frequency of 25600 Hz. Based on empirical observation, the harmonic content in the voltages is very low. However, to illustrate the capabilities of the EMD, one voltage measurement is taken for further analysis. Figure 4.3 gives a closer look at the top of each waveform. The currents have the highest degree of distortions, the most notable being current $L1$. As such, current measurement $L1$ is also included in the analysis. A thorough recount of the methodology

for the analysis of current $L1$ and voltage $L12$ is given in the following section. Appendix A includes the IF and IA for every step of the decomposition.

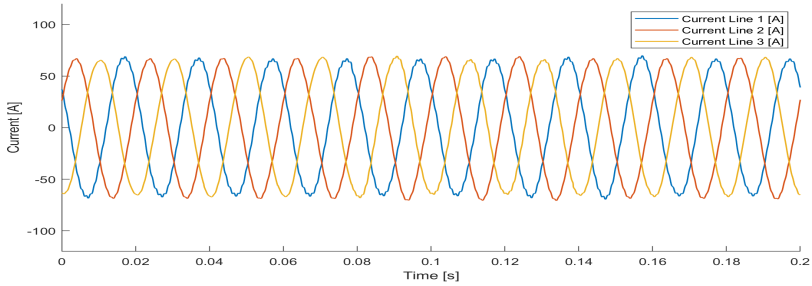

Figure 4.1: Current measurement from a WTG at Hundhammarhjellet, taken the 8th of October 2014 from 23:34:02 to 23:34:06 with a sampling frequency of 25600 Hz.

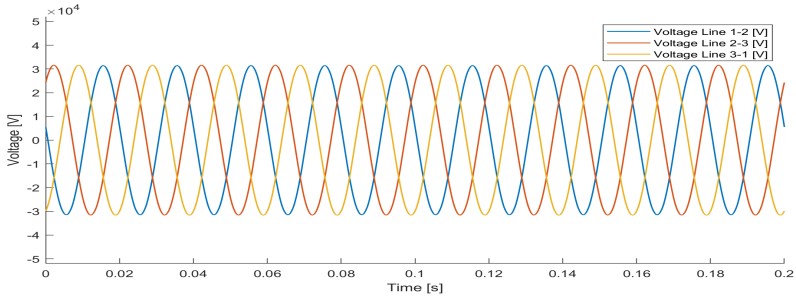

Figure 4.2: Voltage measurement from a WTG at Hundhammarhjellet, taken the 8th of October 2014 from 23:34:02 to 23:34:06 with a sampling frequency of 25600 Hz.

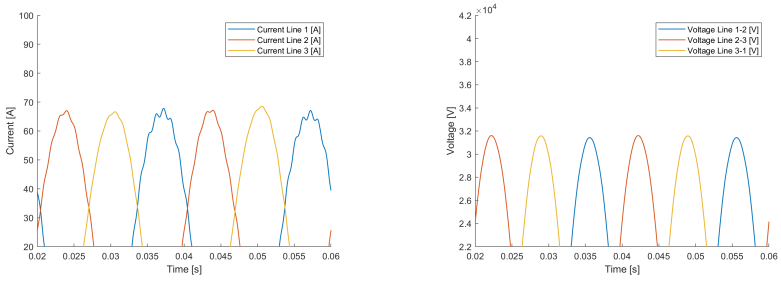

(a) Current measurements.

(b) Voltage measurements.

Figure 4.3: Closer look at the current and voltage measurement.

4.2 Methodology - Classical EMD

4.2.1 Current measurement L1

Figure 4.4 shows the current $L1$ hereby denoted as $f(t)$. Initially, it can be seen that while a 50 Hz component dominates the signal, there are distortions at the peaks and a slight overall change in amplitude over the signal duration. An initial analysis of the signal using FFT can be seen in Figure 4.5. Closer inspection reveals the presence of several frequencies in the signal, the most notable being 1050 Hz, 950 Hz, 250 Hz, and a cluster of inter-harmonics around the 142 Hz frequency.

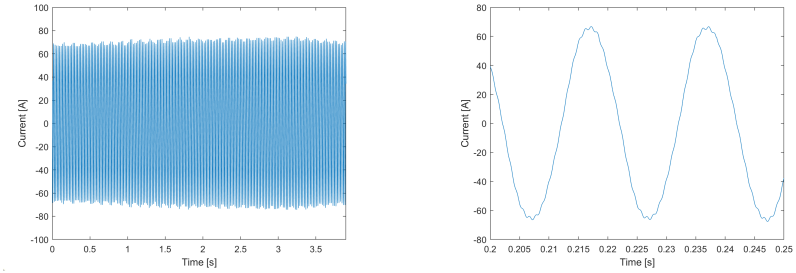

(a) Overall view of current measurement $f(t)$.

(b) Closer look at current $f(t)$.

Figure 4.4: Current measurement $f(t)$.

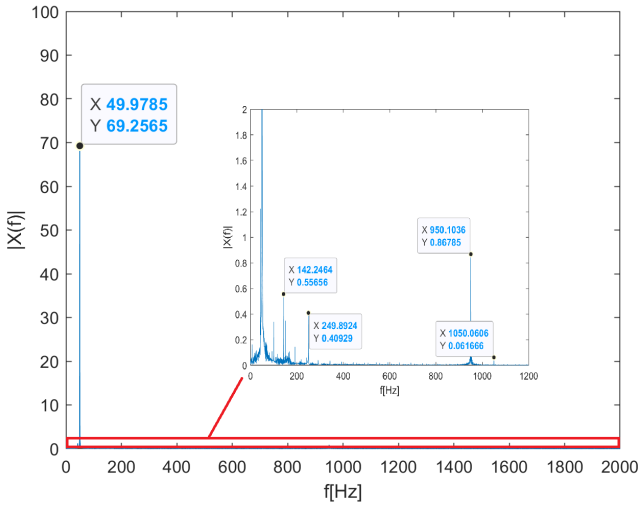

Figure 4.5: FFT of the dominant frequency, and a close-up of the other frequency components present in $f(t)$.

Extraction of the 50 Hz Component

Separation of the modes is initially attempted by the use of EMD, which resulted in 11 IMFs, the most relevant being shown in Figure 4.6. Visual inspection of the resulting IMFs indicates that parts of IMF 2 are leaking into the subsequent IMFs. This assumption is supported by applying FFT to each IMF, as seen in Figure 4.7. The results reveal mode-mixing between the 50 Hz component and what is assumed to be lower frequency noise components, the latter being either part of the original signal hidden by the dominating 50 Hz component, or a byproduct of the EMD.

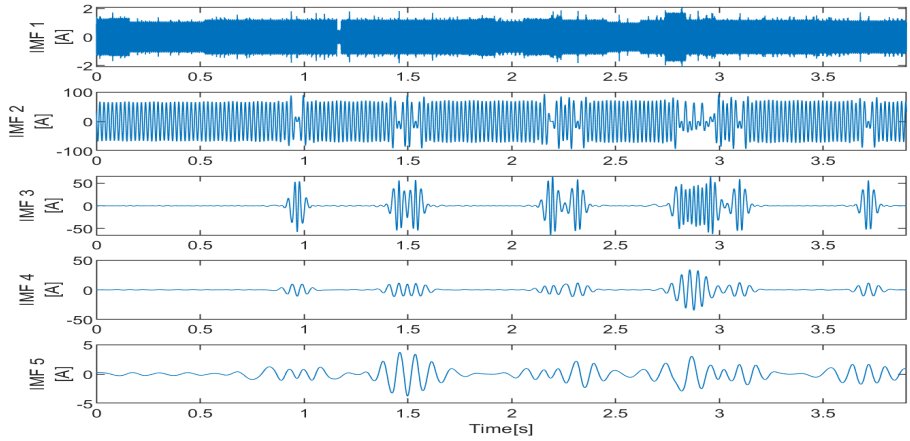

Figure 4.6: Resulting IMFs from EMD applied to $f(t)$.

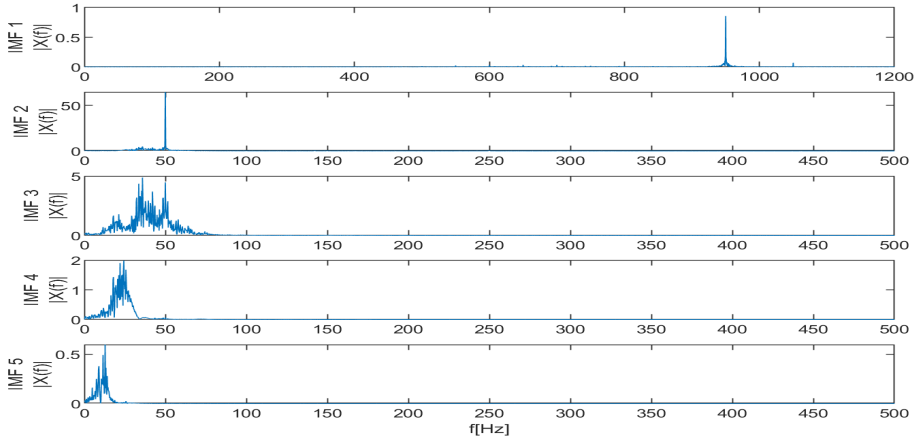

Figure 4.7: Closer look at the FFT of IMF 1.

Taking advantage of the significantly higher amplitude of the 50 Hz component, an appro-

priate masking signal, denoted as $f_{m1}(t)$, is constructed to avoid mode-mixing and leaking IMFs.

$$f_{m1}(t) = 5000sin(2\pi 200t) \tag{4.1}$$

The resulting IMFs their respective FFT can be seen in Figure 4.8 and 4.9. A more detailed version of IMF 1 can be seen in Figure 4.10. The leaking of IMF 2 is corrected, and IMF 1 now account for most of the modes uncovered in the initial FFT.

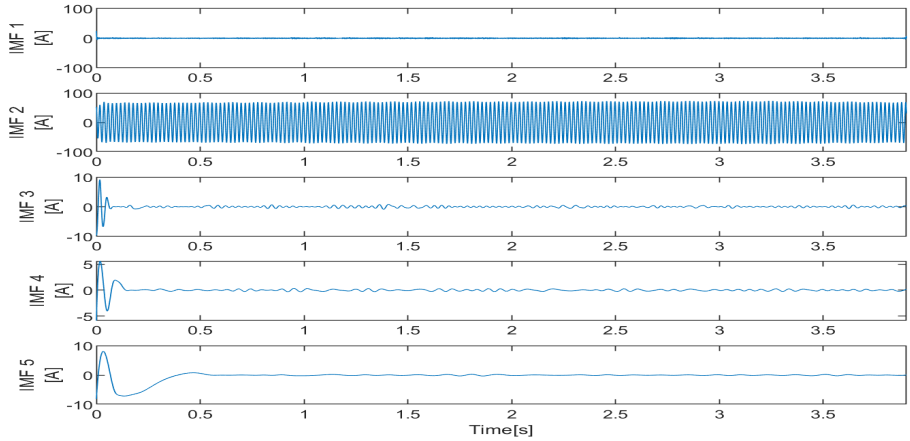

Figure 4.8: Resulting IMFs from EMD applied to $f(t)$ after adding masking signal $f_{m1}(t)$.

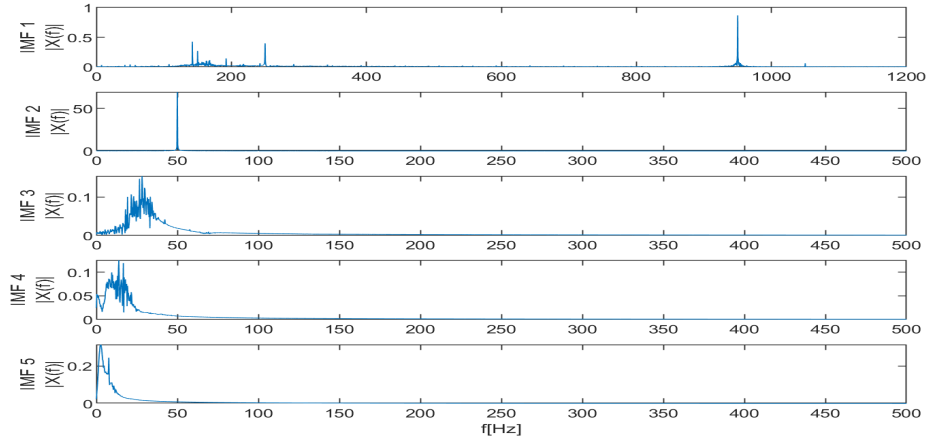

Figure 4.9: FFT of the IMFs from EMD applied to $f(t)$ after adding masking signal $f_{m1}(t)$.

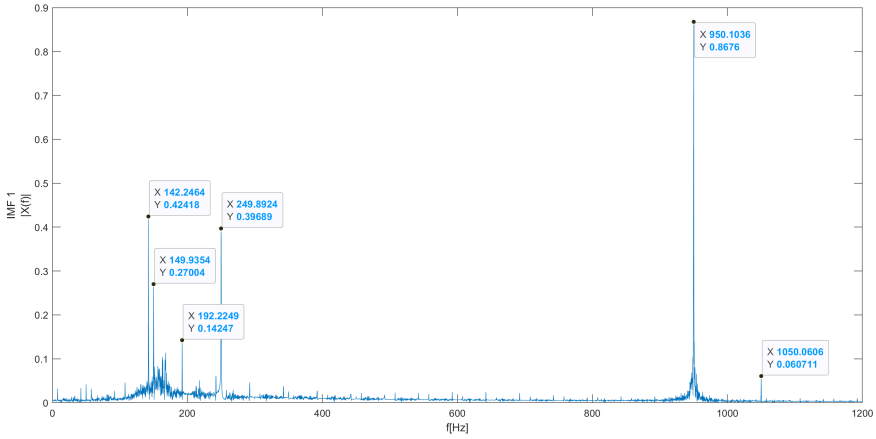

Figure 4.10: Closer look at the FFT of IMF 1 after adding masking signal $f_{m1}(t)$.

IMF 2 is now considered an adequately pure representation of the 50 Hz component and is extracted from the original signal and treated as a final IMF, as seen in Figure 4.56. The resulting signal $f_1 = f(t) - IMF_{50}$ is given in Figure 4.11.

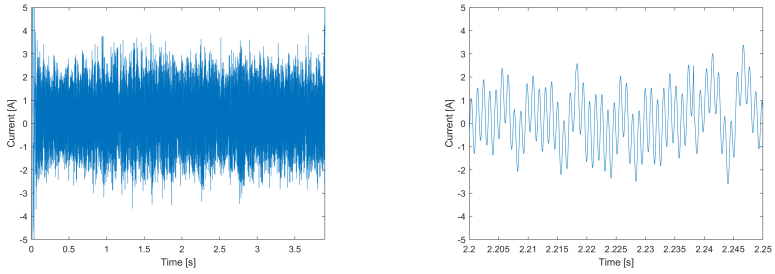

(a) Overall view of $f_1(t)$. **(b)** Close-up of $f_1(t)$.

Figure 4.11: Resulting signal $f_1(t)$, after removing 50 Hz component.

Extraction of 950 Hz Component

The 50 Hz component has been successfully removed, and now the 950 Hz component dominates the signal. Separation by EMD gives results as can be seen in Figure 4.12 and 4.13. A closer look at IMF 1 is given in Figure 4.14. Though there is a trace of mode-mixing with a 1050 Hz frequency component, it is deemed a satisfactory IMF as the modes are too close in both frequency and amplitude for adequately pure separation using masking signals.

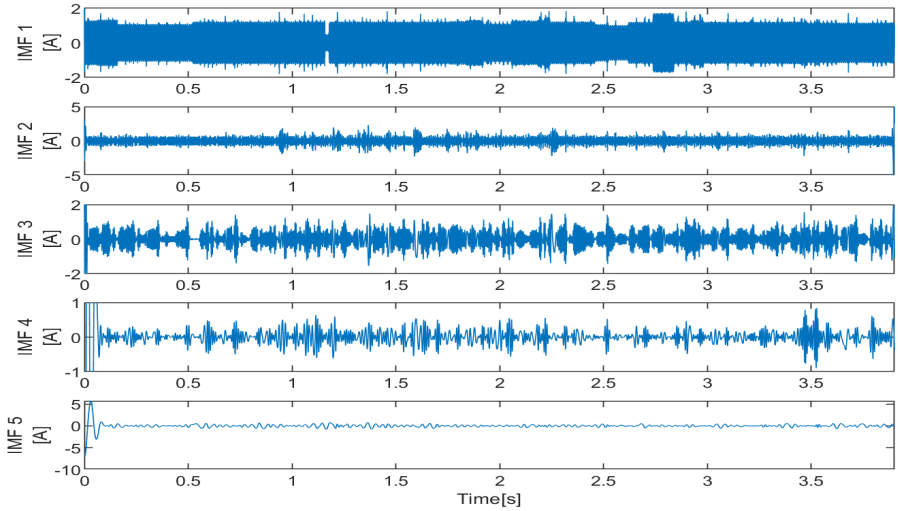

Figure 4.12: Resulting IMFs from EMD applied to $f_1(t)$.

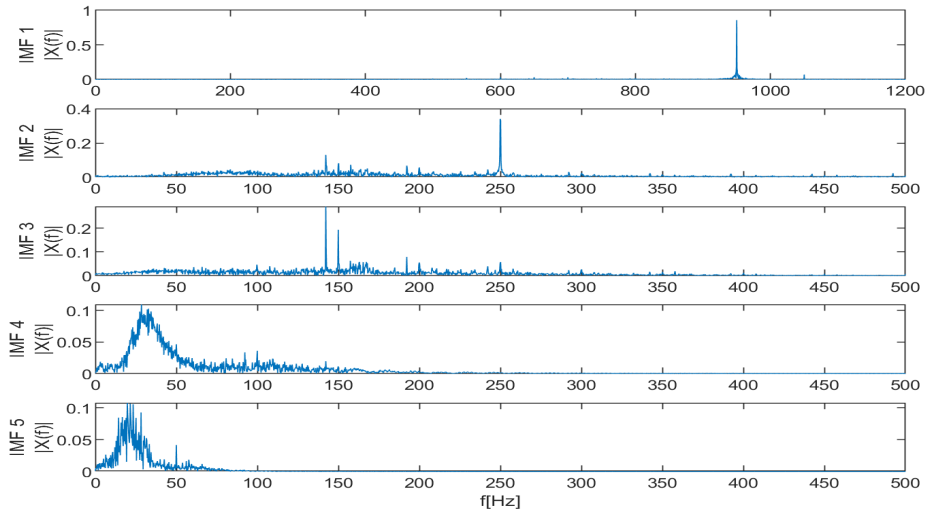

Figure 4.13: FFT of the IMFs from EMD applied to $f_1(t)$.

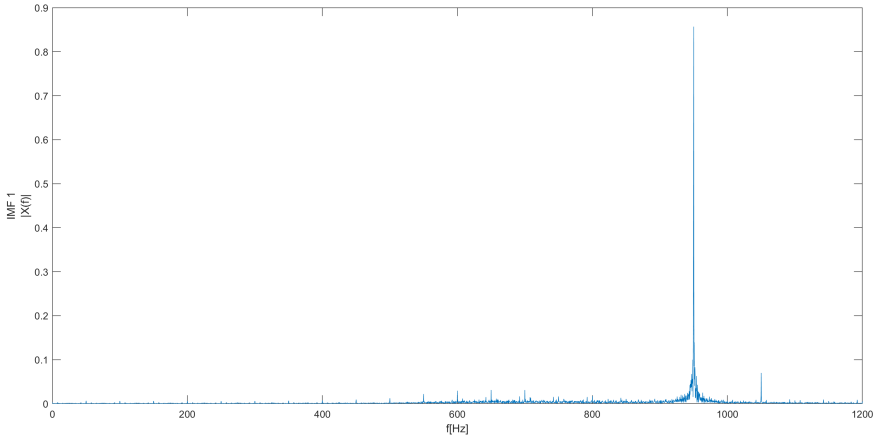

Figure 4.14: Closer look at FFT of IMF 1 of signal $f_1(t)$.

Treating IMF 1 as a resulting IMF in Figure 4.56 it is extracted from the signal such that $f_2(t) = f_1(t) - IMF_{950}$. The resulting signal can be seen in Figure 4.15.

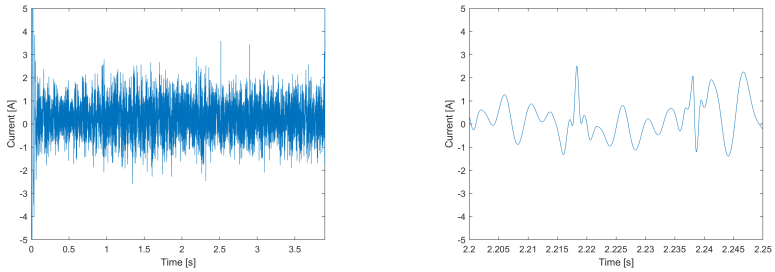

(a) Overall view of $f_2(t)$. **(b)** Close-up of $f_2(t)$.

Figure 4.15: Resulting signal $f_2(t)$, after removing 50 Hz and 950 Hz component.

Extraction of 250 Hz Component

Using $f_2(t)$ as the new signal results as can be seen in Figure 4.16. It is not immediately obvious from visual inspection of the IMFs that they represent separate modes, however, the resulting FFTs given in Figure 4.17 indicates that the cluster of inter-harmonics and the 250 Hz component initially found in the original signal $f(t)$ are represented by the two first IMFs.

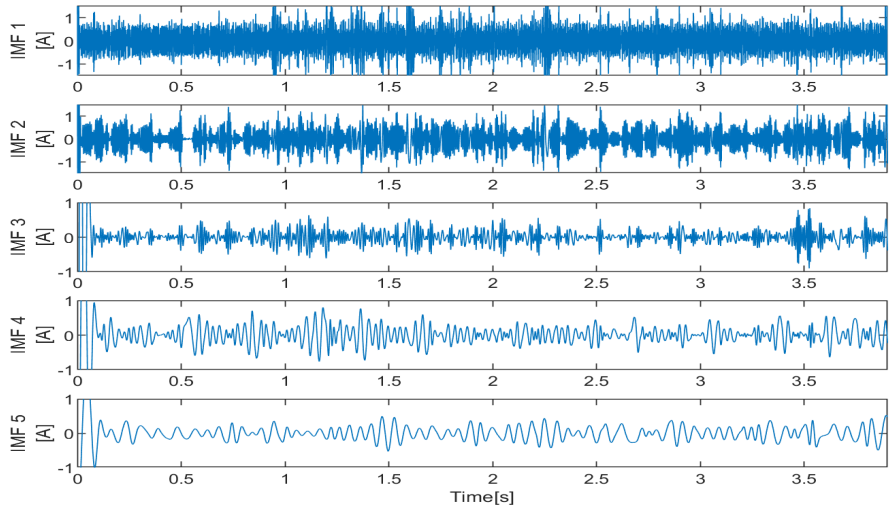

Figure 4.16: Resulting IMFs from EMD applied $f_2(t)$.

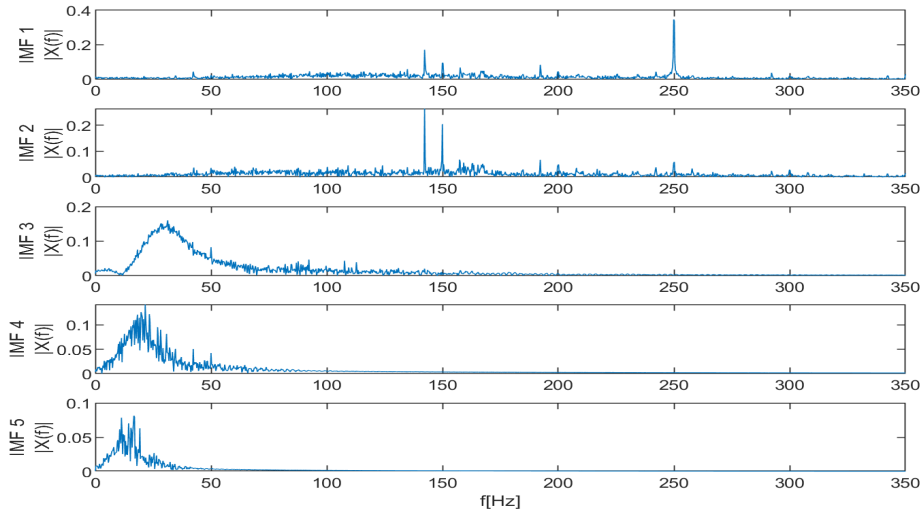

Figure 4.17: FFT of the IMFs from EMD applied to $f_2(t)$.

There appears to be a high degree of mixing between the two IMFs, as such a masking signal is constructed in an attempt to separate the 250 Hz frequency component from the inter-harmonics.

$$f_{m2}(t) = 0.05sin(2\pi 140t) \tag{4.2}$$

Results of this can be seen in Figure 4.18 and 4.19.

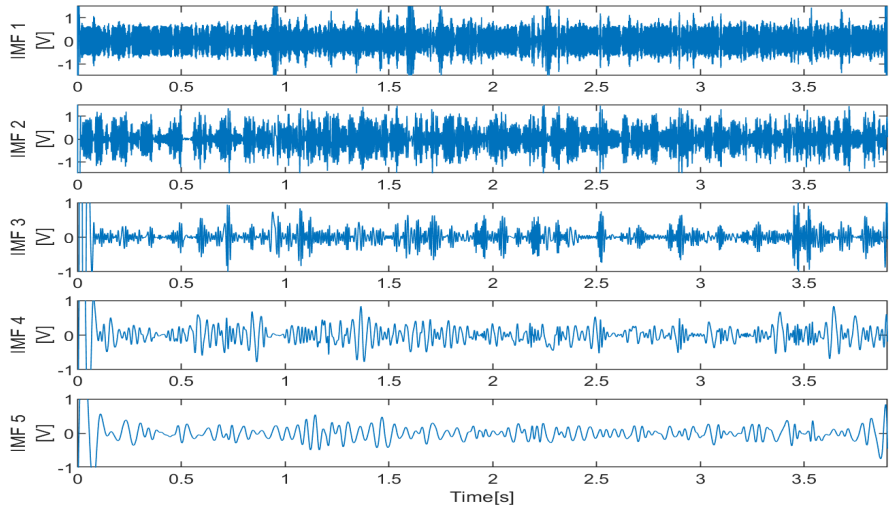

Figure 4.18: Resulting IMFs from EMD applied $f_2(t)$ after adding masking signal $f_{m2}(t)$.

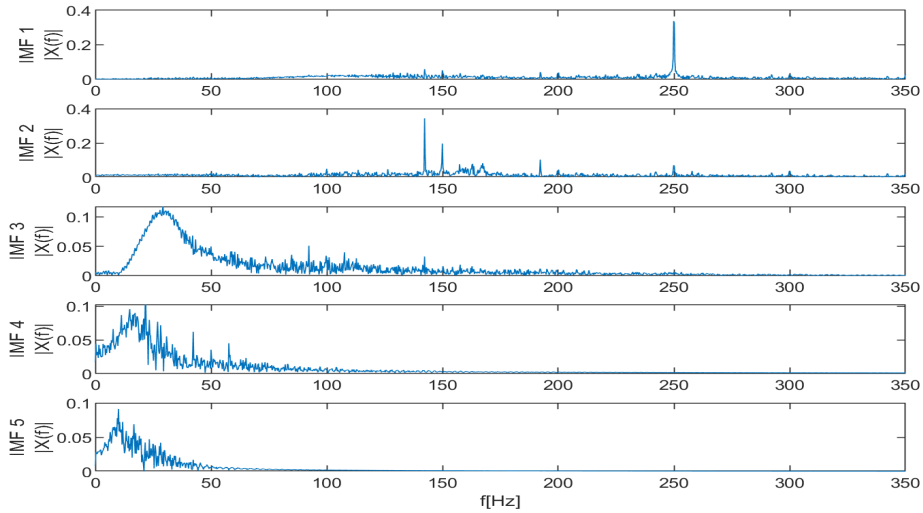

Figure 4.19: FFT of the IMFs from EMD applied to $f_2(t)$ after adding masking signal $f_{m2}(t)$.

The masking signal appears to have some effect indicated both by the smoother IMF and the reduction of the amplitudes in the FFT. However, there is still obvious signs of mode-mixing between the IMFs, indicated by the spikes in IMF 1 having an equal reduction at the same time in IMF 2. Further separation by masking signal is not successfully and IMF 1 is treated as a final IMF and is added to the resulting IMFs. Based on the amount of different frequencies of inter-harmonic nature and its irregular appearance, IMF 2 is

deemed to be a noise component. However, as these frequencies are indicated in the initial analysis of the original signal, and as there have been reports of inter-harmonics appearing in relation to WTG, IMF 2 is not added to the residue but rather seen as a separate ”noisy IMF”. IMF 2 is thus removed from the signal and is added as a final resulting IMF. Now, the remains are deemed to be residue originating from the EMD algorithm itself or the removal of IMFs from the signal. They are thus combined and treated as the resulting residue.

4.2.2 Voltage measurement L12

Figure 4.20 shows the voltage $L12$, hereby denoted as g(t). Initial visual inspection of the signal indicates that a pure sinusoidal of 50 Hz without the change or disturbances seen in $L1$. The results of applying FFT to the signal can be seen in Figure 4.21. It is as expected dominated by a 50 Hz component; however, closer inspection reveals the presence of other modes mixed in the signal. While these harmonics are too low to pose a operational issue, analysis of this signal can be useful in a diagnostic perspective.

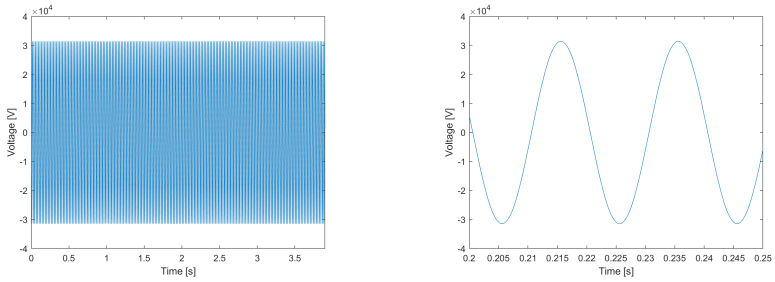

(a) Overall view of voltage measurement $g(t)$.

(b) Closer look at voltage $g(t)$.

Figure 4.20: Voltage measurement $g(t)$

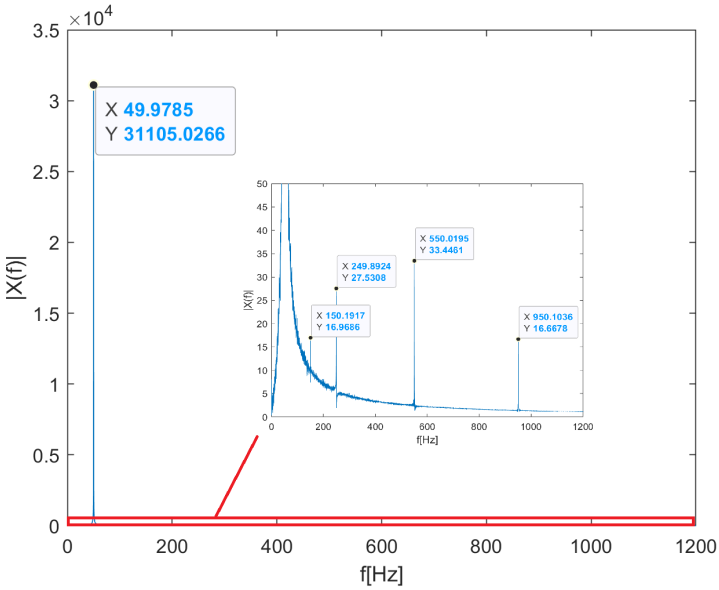

Figure 4.21: FFT of the dominant frequency, and a close-up of the other frequency components present in $g(t)$.

Extraction of the 50Hz Component

Attempting to separate the modes using EMD resulted in 15 IMFs, were IMF one to five are shown in Figure 4.22. The FFT of each IMF can be seen in Figure 4.23.

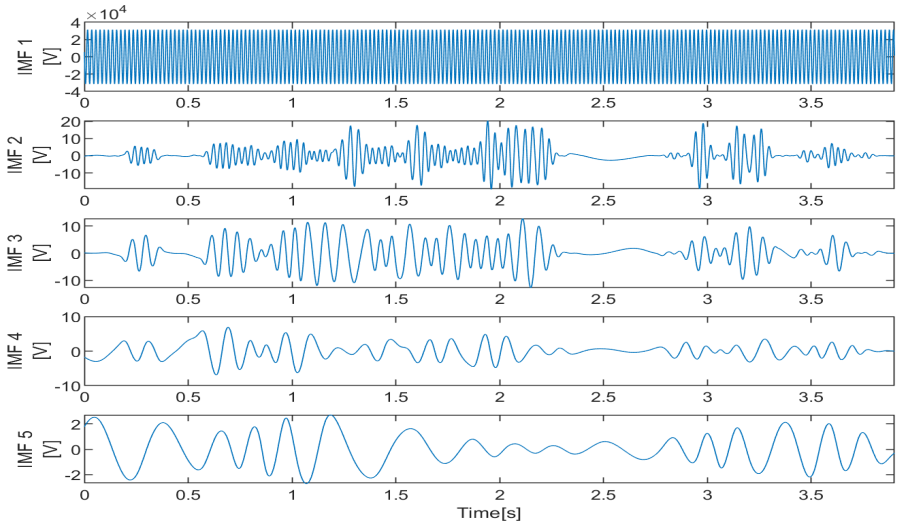

Figure 4.22: Resulting IMFs from EMD applied to $g(t)$.

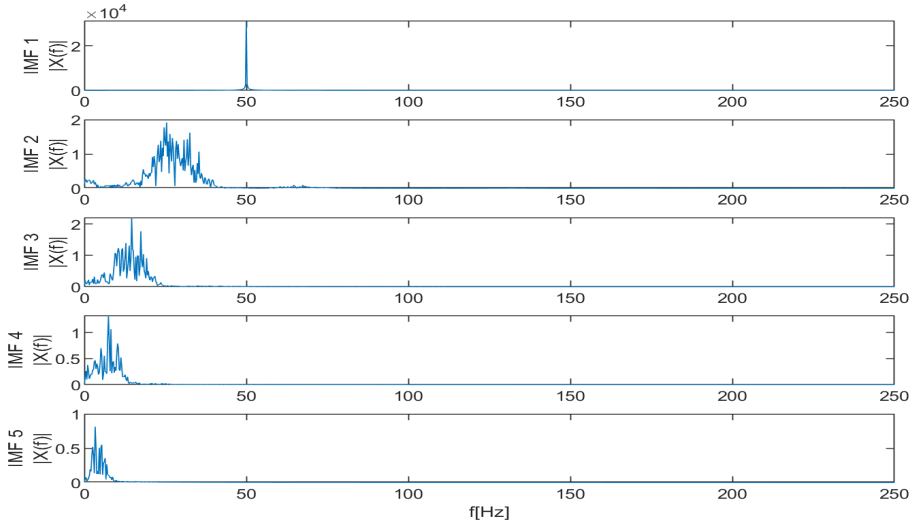

Figure 4.23: FFT of the IMFs from EMD applied to $g(t)$.

Based on the appearance of the IMFs and their FFTs, it seems EMD was unsuccessful

in separating the components uncovered by the initial FFT. The low amplitude of IMF 2 and up indicates these are residue and noise components due to the empirical nature of the separation. A closer look at IMF 1, seen in Figure 4.24 reveals that it is indeed an unsuccessful separation attempt; all modes are present in the first IMF.

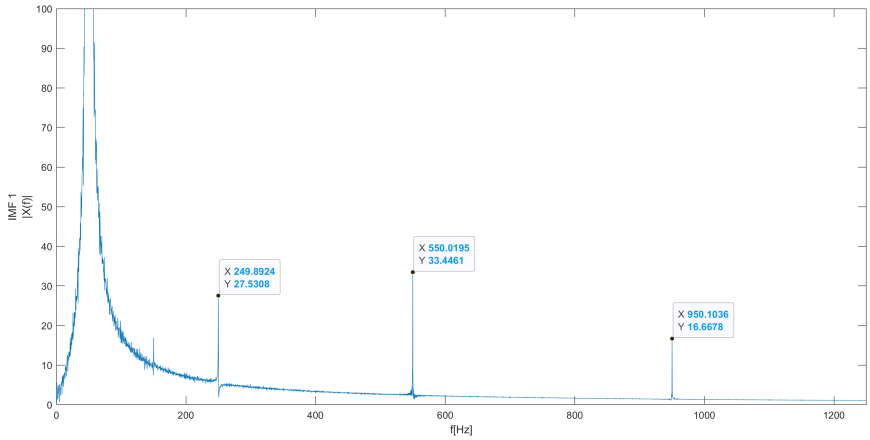

Figure 4.24: FFT of IMF 1 after applying EMD

This is expected as EMD is an empirical method, relying on extrema in the superimposed signal to extract relevant modes. While it might seem counter-intuitive, a high amplitude masking signal will actually reveal the lower amplitude harmonics in the signal. As the EMD is only able to extract the original signal (without the harmonics as they are too low to be seen) from the new superimposed signal, IMF 1 will contain both the masking signal and the harmonic content. Thus, masking signal $g_{m1}(t)$ is constructed in an attempt to separate the 50 Hz component and the lower amplitude harmonics.

$$g_{m1}(t) = 40000000sin(2\pi 230t) \tag{4.3}$$

The resulting IMFs and their respective FFTs after applying $g_{m1}(t)$ can be seen in Figure 4.25 and 4.26.

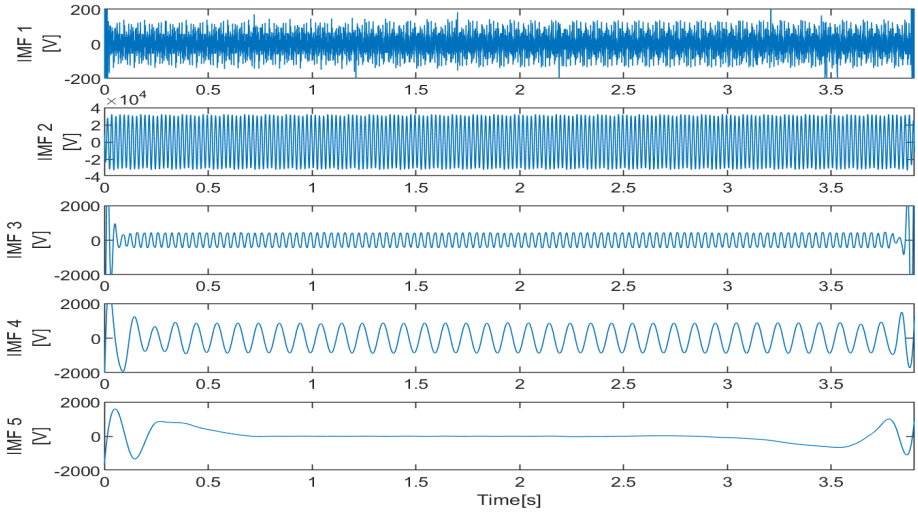

Figure 4.25: Resulting IMFs from EMD applied to $g(t)$ after adding masking signal $g_{m1}(t)$.

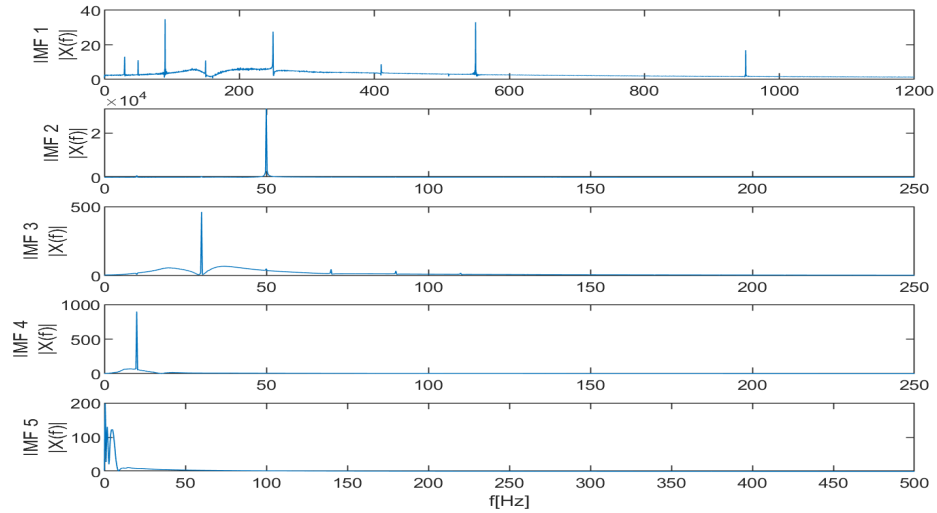

Figure 4.26: FFT of the IMFs from EMD applied to $g(t)$ after adding masking signal $g_{m1}(t)$.

Based on the results from the FFT, IMF 2 seems to represent the 50 Hz component, while IMF 1 contains the other modes previously uncovered. IMF 3 and 4 now represent almost perfect sinusoids with frequencies 30 and 10 Hz, respectively. Initially, it appears these IMFs represents previously hidden modes, possibly masked by the 50 Hz component. However, there is now a slight amplitude modulation present in IMF 2. This modulation is revealed to match the frequency of IMF 3 and 4, such that when these IMFs are combined,

it results in a sinusoid of 50 Hz without amplitude modulations. This is shown in Figure 4.27.

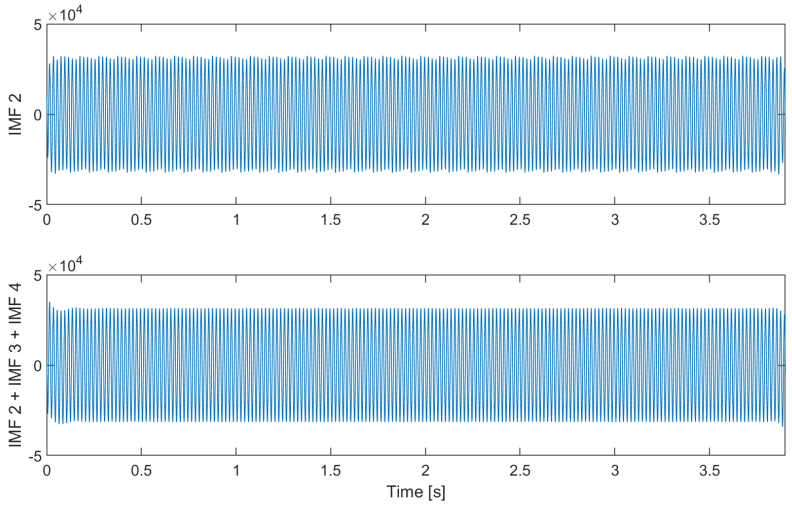

Figure 4.27: An example of over-decomposition. IMF 2 is shown to better represent the original signal when added to IMF 3 and IMF 4.

Thus the combination of IMF 2, 3, and 4 is treated as an adequately pure representation of the 50 Hz component and is removed from the original signal, $g_1(t) = g(t) - IMF_{50}$. These IMFs are combined and treated as a final result in Figure 4.64. The resulting signal $g_1(t)$ can be seen in Figure 4.28.

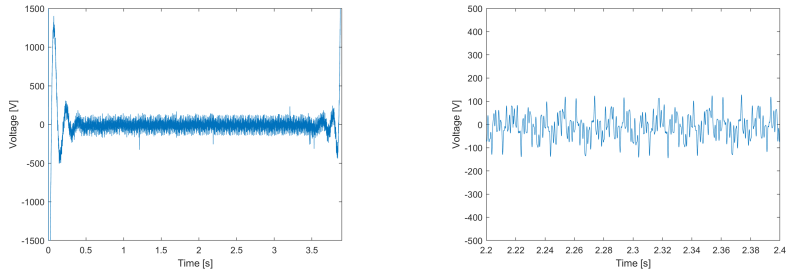

(a) Overall view of $g_1(t)$.

(b) Close-up of $g_1(t)$.

Figure 4.28: Resulting signal $g_1(t)$, after removing 50 Hz component.

Extraction of the 950 Hz Component

As the main component is removed, the signal is now much more erratic. The initial analysis is done through FFT, as can be seen in Figure 4.28(a). Relying on the result from the FFT, it appears to be a high amplitude low-frequency distortion present in the signal. The presence can be attributed to the slight boundary error condition, as seen in IMF 2 in Figure 4.25. As IMF 2 is removed from the original signal, the impact of the boundary error propagates to the much lower amplitude signal $g_1(t)$, making FFT a less reliable tool when observing the complete signal. In an attempt to limit the effect of the boundary conditions, FFT is applied to $g_1(t)$ for $t \in [0.5, 3.5]$. The results can be observed in Figure 4.28(b). It is thus reasonable to contribute lower frequency distortions present in the FFT to boundary errors due to the EMD. There also appears to be several new low-frequency component present in the resulting signal based on the FFT. However, this presence can likely be contributed residue due to the removal of the 50 Hz component. As EMD satisfies the perfect reconstruction condition, the new components pose no problem for the overall analysis.

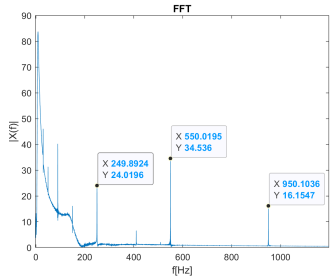

(a) FFT of $g_1(t)$

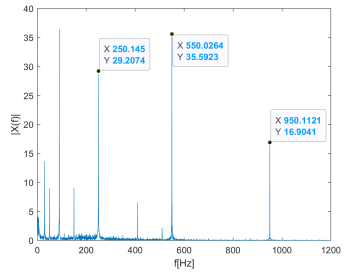

(b) FFT of $g_1(t)$ omitting the ends of the signal.

Figure 4.29: FFT of $g_1(t)$ with and without boundary condition errors

The results of using EMD to separate the modes can be seen in Figure 4.30. Applying FFT to each IMF can be seen in Figure 4.31.

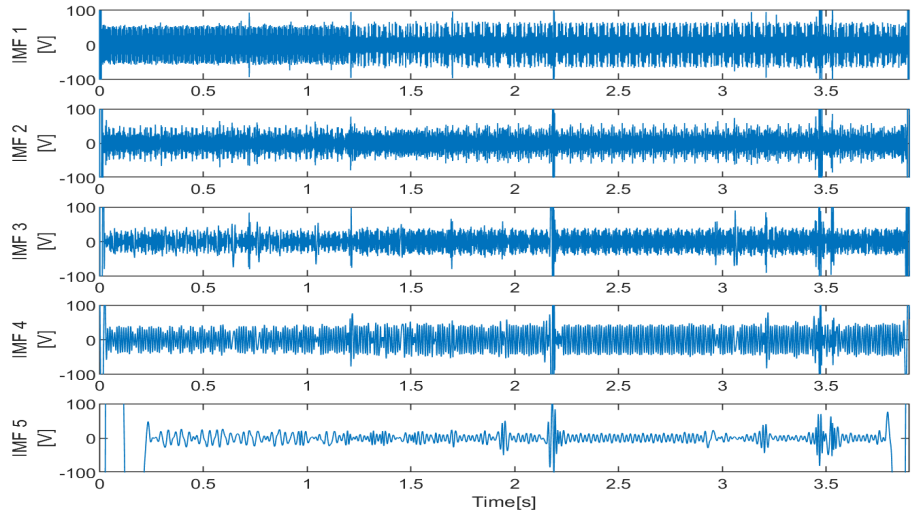

Figure 4.30: Resulting IMFs from EMD applied to $g_1(t)$.

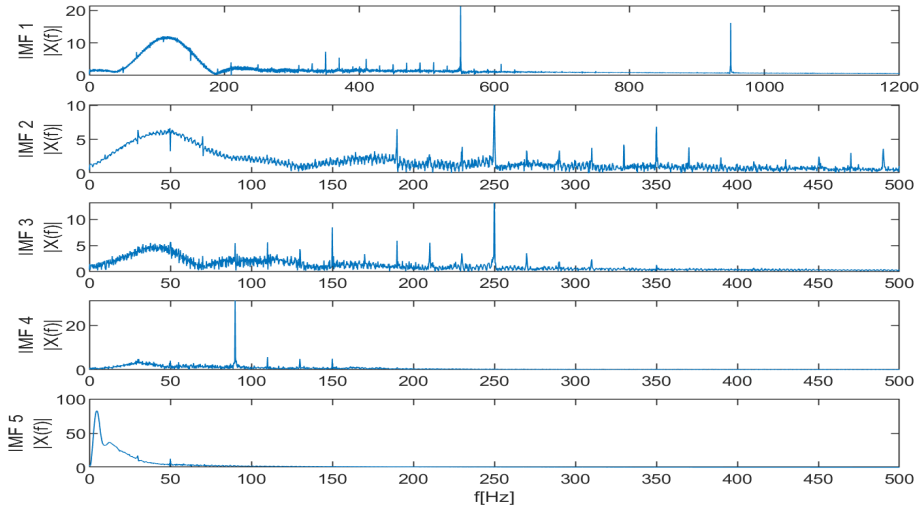

Figure 4.31: FFT of the IMFs from EMD applied to $g_1(t)$.

Based on the FFTs, there seems to a low-frequency presence in the first three IMFs. This can again be contributed to the boundary errors. However, based on the results from the initial FFT and the FFT of IMF 1, there appears to be a mode mix between components of

950 Hz and 550 Hz. This presence can also be noted visually in the IMF as there is a clear distinction at $t = 1.25s$. A masking signal $g_{m2}(t)$ is thus constructed to separate these modes.

$$g_{m2}(t) = 200sin(2\pi 1200t) \tag{4.4}$$

The new IMFs and their FFTs after applying $g_{m2}(t)$ can be seen in Figure 4.32 and 4.33.

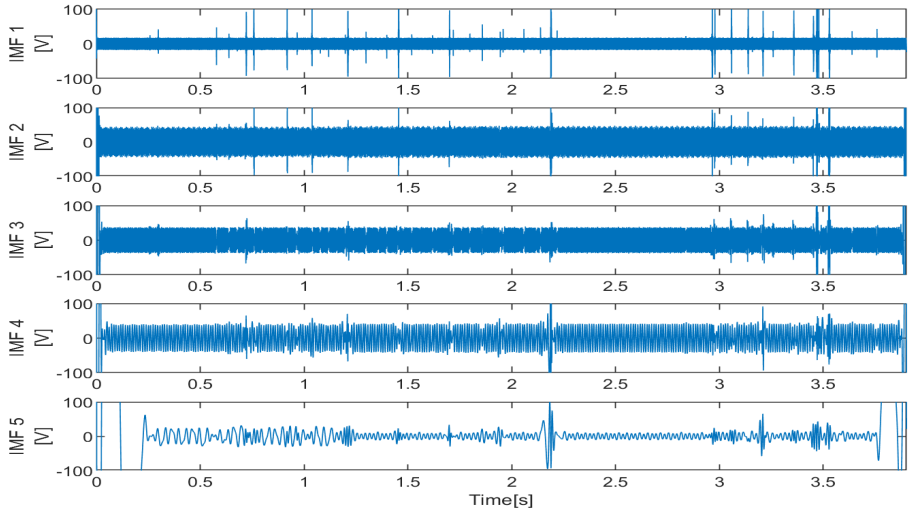

Figure 4.32: Resulting IMFs from EMD applied to $g_1(t)$ after adding masking signal $g_{m2}(t)$.

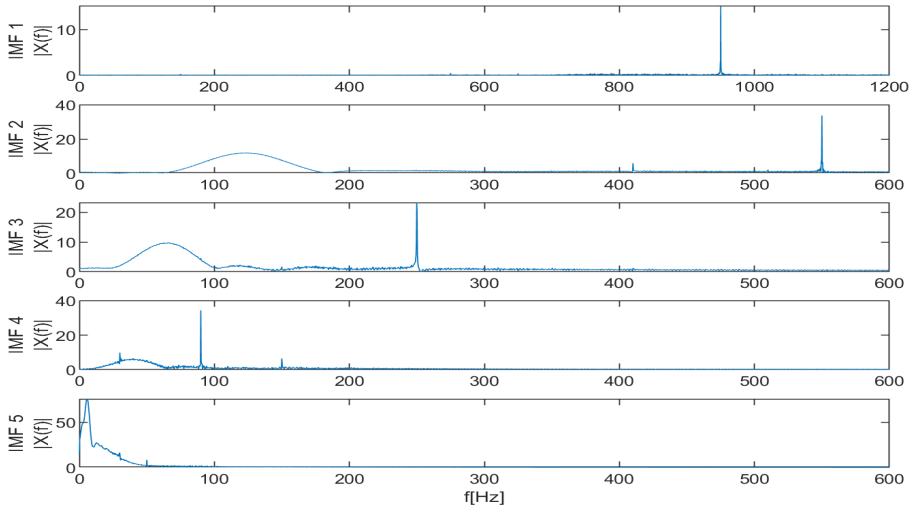

Figure 4.33: FFT of the IMFs from EMD applied to $g_1(t)$ after adding masking signal $g_{m2}(t)$.

IMF 1 now represents an adequately pure representation of the 950 Hz component. It is thus removed from the signal and treated as a final result, $g_2(t) = g_1(t) - IMF_{950}$. The resulting signal $g_2(t)$ can be seen in Figure 4.35.

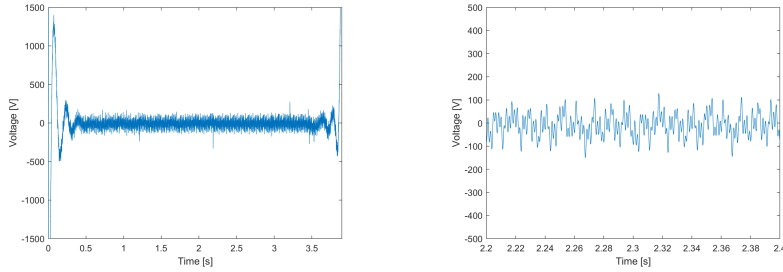

(a) Overall view of $g_2(t)$.

(b) Close-up of $g_2(t)$.

Figure 4.34: Resulting signal $g_2(t)$, after removing 50 and 950 Hz component.

The masking signal also separate the modes mixed in IMF 2 and IMF 3. As the low frequencies present in the FFTs can be contributed to the boundary errors, these IMFs can also be considered adequately pure representations of their respective frequency. However, the masking signal method is here seen to effectively separate the oscillations due to the boundary errors in IMF 1 from the actual oscillations in the IMF. While this method has limited visual results for the IMFs, it is seen to be highly effective when EMD is used in conjunction with FFT, as the resulting FFTs represents each IMF more accurately. To further illustrate this, the 550 and 250 Hz components are removed after applying a masking signal to reduce the boundary error effects in the FFT.

Extraction of 550 and 250 Hz Component

The result of applying EMD to the signal can be seen in Figure 4.35. Looking at the FFTs as given in Figure 4.36 the presence of boundary errors is again noticeable in the relevant IMFs.

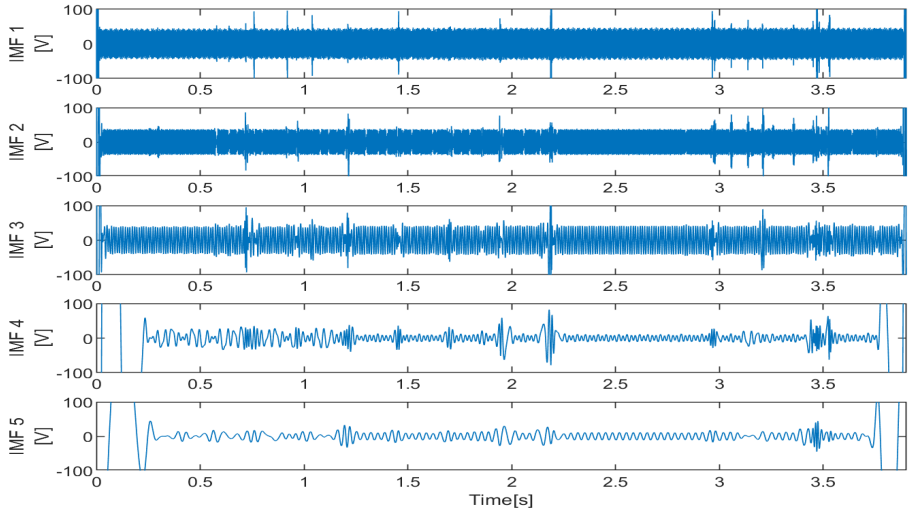

Figure 4.35: Resulting IMFs from EMD applied to $g_2(t)$.

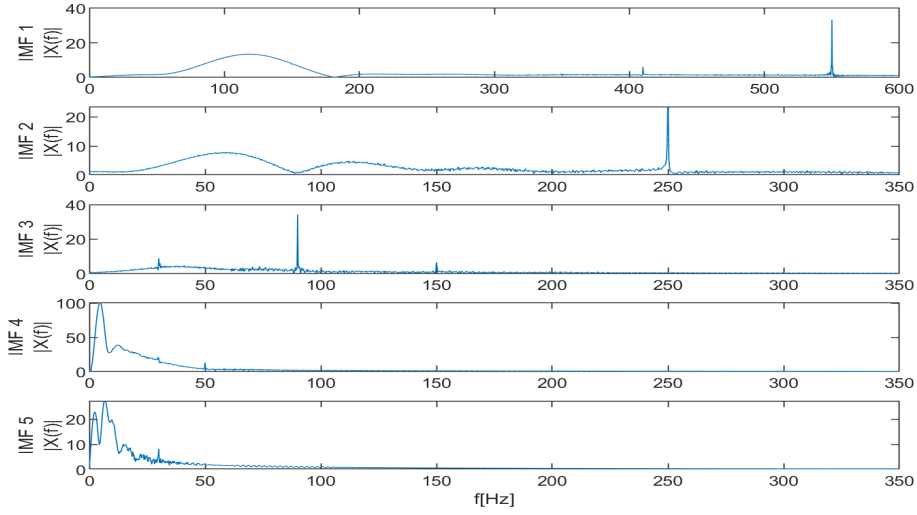

Figure 4.36: FFT of the IMFs from EMD applied to $g_2(t)$.

In an attempt to reduce the effect of the boundary error, masking signals $g_{m3}(t)$ is applied to the signal.

$$g_{m3}(t) = 300sin(2\pi 540t) \tag{4.5}$$

The results of applying $g_{m3}(t)$ can be seen in Figure 4.37 and 4.38.

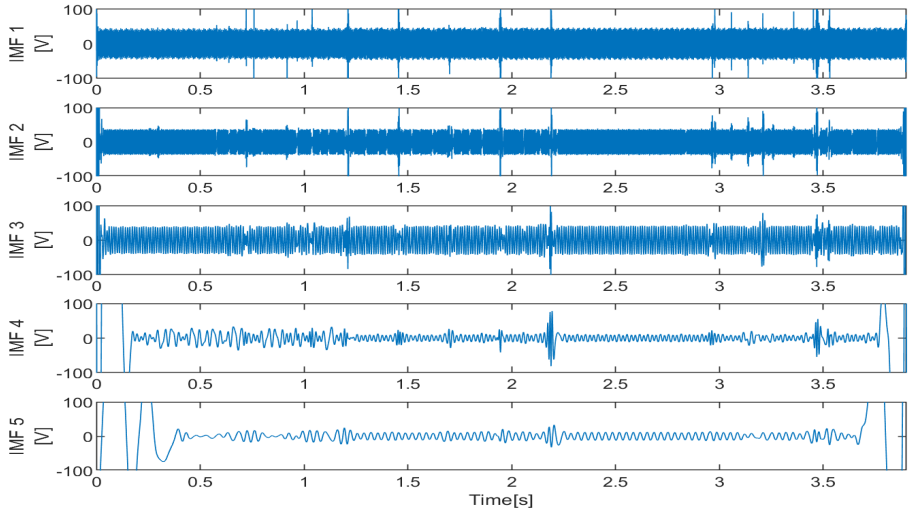

Figure 4.37: Resulting IMFs from EMD applied to $g_2(t)$ after adding masking signal $g_{m3}(t)$.

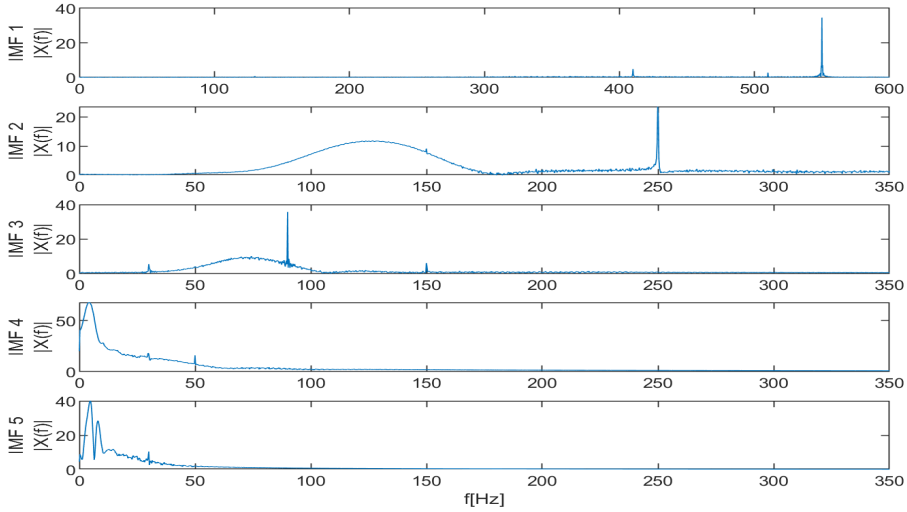

Figure 4.38: FFT of the IMFs from EMD applied to $g_2(t)$ after adding masking signal $g_{m3}(t)$.

IMF 1 represents an adequately pure IMF and is treated as a final result. IMF 2 is also treated as an adequately pure IMF as the frequency and amplitude of the oscillation due to the boundary error is too close to the IMF itself for the effective use of a masking signal. The leftover component $g_3(t) = g_3(t) - IMF_{550} - IMF_{250}$ as seen in Figure 4.39 is treated as residue and is added as is added to the results as the residue component.

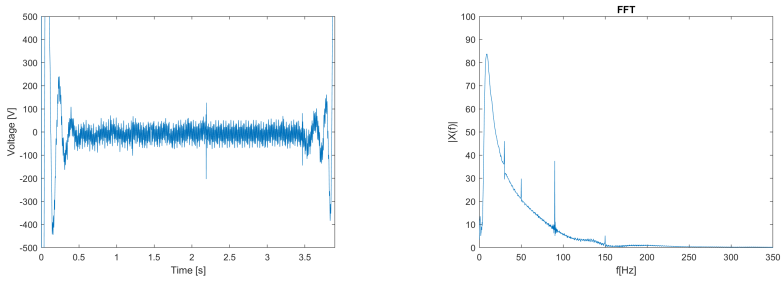

(a) Overall view of $g_3(t)$.

(b) Close-up of $g_3(t)$.

Figure 4.39: Resulting signal $g_3(t)$.

4.3 Methodology - Online EMD

Current measurement $L1$ denoted $f(t)$ depicted in Figure 4.4 and voltage measurement $L12$ denoted $g(t)$ depicted in Figure 4.20 are now decomposed using Online EMD. The standard EMD algorithm in the previous analysis is used as the base for the Online version, keeping previously used parameters constant. Window size $l = 10$ has been chosen for all cases.

4.3.1 Current measurement L1

The sliding window of the Online EMD continuously uncovers intrinsic mode functions as it moves through the signal. Thus there is a delay to the uncovered IMFs based on the rate of extrema and the length of the sliding window. As such, the possible number of IMFs extracted increases as the number of data points increases and are added by the EMD. Snapshots of the on-going decomposition after 662, 2650, and 10600 data points have been processed is shown in Figure 4.40 from left to right, respectively. The colors black, blue, and teal indicates that 2650, 5300, and 10600 data points have been used in the process. Red illustrates parts of the IMF still incomplete. For further analysis using Online EMD, only the results of iterating through all available data points are shown.

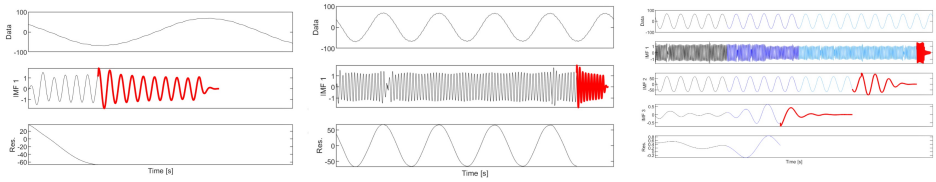

Figure 4.40: Online EMD applied to $L1$.From left to right, the total data points are 662, 2650, and 10600. The black part of the signal is related to the first 2650 data points. The blue part is related to the parts 2650 to 5300, and teal is related to the parts from 5300 to 10600. Red indicates the parts of the IMFs still incomplete

Initial analysis

The result of applying Online EMD to $f(t)$ can be seen in Figure 4.41. The FFT of each IMF can be seen in Figure 4.42. The separation of the 950 Hz component is successful. However, as with the classical EMD, the 50 Hz component represented by IMF 2 contains most of the modes uncovered by initial the FFT, and IMF 2 is leaking to the subsequent IMFs.

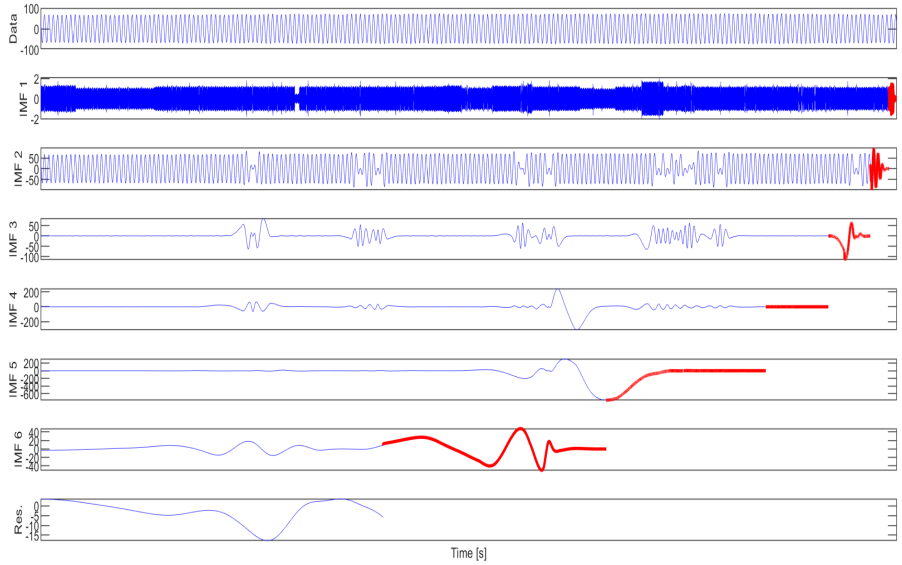

Figure 4.41: Online EMD applied to $f(t)$. In red are parts of the IMFs still incomplete.

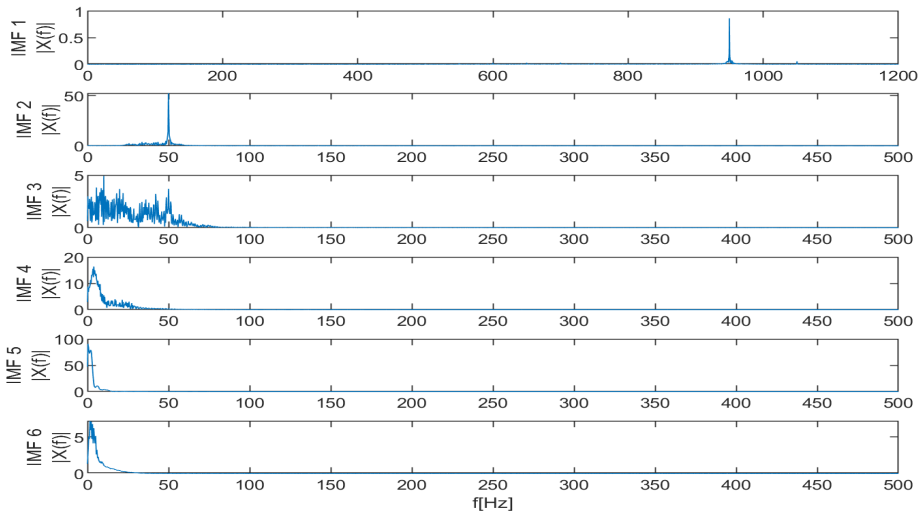

Figure 4.42: FFT of the resulting IMFs of $f(t)$ given by Online EMD.

In an attempt to reduce leakage and separate the 50 Hz component from other modes, mode-mixing separation by masking signal is adjusted and applied to the Online version. As the length of the IMFs extracted by the Online EMD varies based on the modes uncovered, the method is now adjusted to account for uneven IMFs. The result of running

two Online EMDs in parallel, using masking signal $f_{m1}(t)$ and matching the output for each IMF can be seen in Figure 4.43 and the FFT of each IMF in Figure 4.44. Based on the visual inspection of IMF 2 and the FFT of IMF 2, it appears the 50 Hz component has been separated successfully.

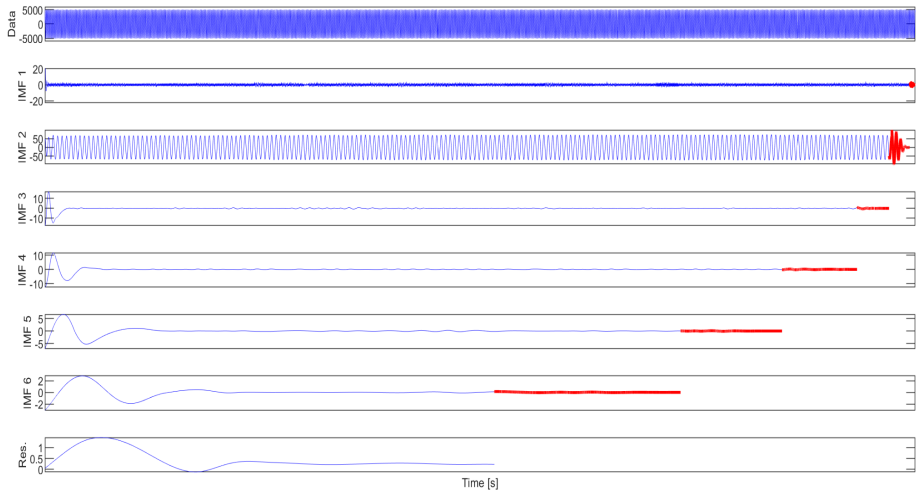

Figure 4.43: IMFs after Masking signal $f_{m1}(t)$ is applied to signal $f(t)$ for the Online EMD

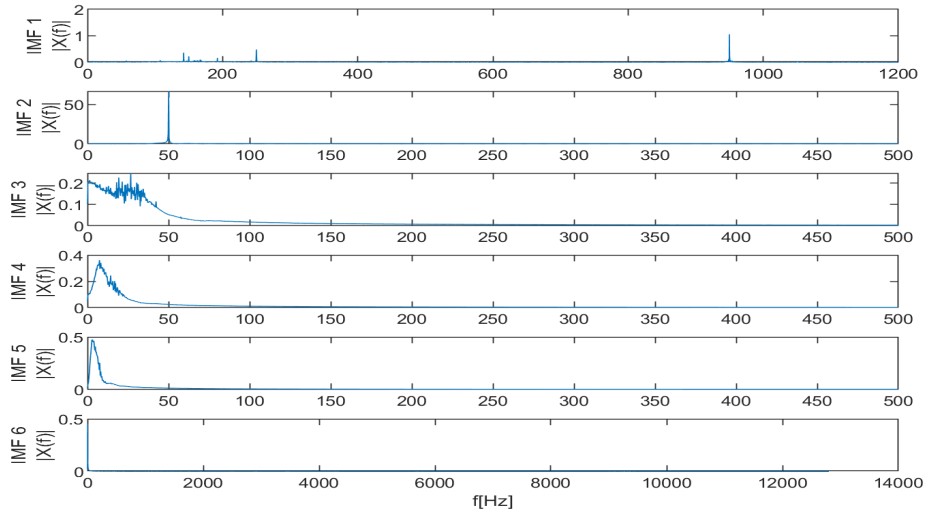

Figure 4.44: FFT of the IMFs after masking signal $f_{m1}(t)$ is applied to signal $f(t)$ for the Online EMD

To simulate the analysis of a data stream, further analysis is done without altering the original signal. IMF 2 is seen as an adequately pure IMF and is treated as a final result. IMF 1 is thus treated as the new input, $f_1(t) = IMF_{950}$.

Further decomposition of IMF 1

The results of applying Online EMD to $f_1(t)$ can be seen in Figure 4.45. The FFT of each IMF can be seen in Figure 4.46. IMF 1 is now seen to represent the 950 Hz component, while IMF 2 and 3 contain the rest of the frequencies previously uncovered using classical EMD. IMF 1 is seen as an adequately pure IMF and is treated as a final result. While IMF 2 and 3 show signs of mode-mode mixing in their FFTs, further separation and use of masking signal shows no effect. They are, therefore, also treated as final results. Due to the low amplitude of IMF 4 and 5, these are deemed to be noise components and are thus added to the final IMFs as residue.

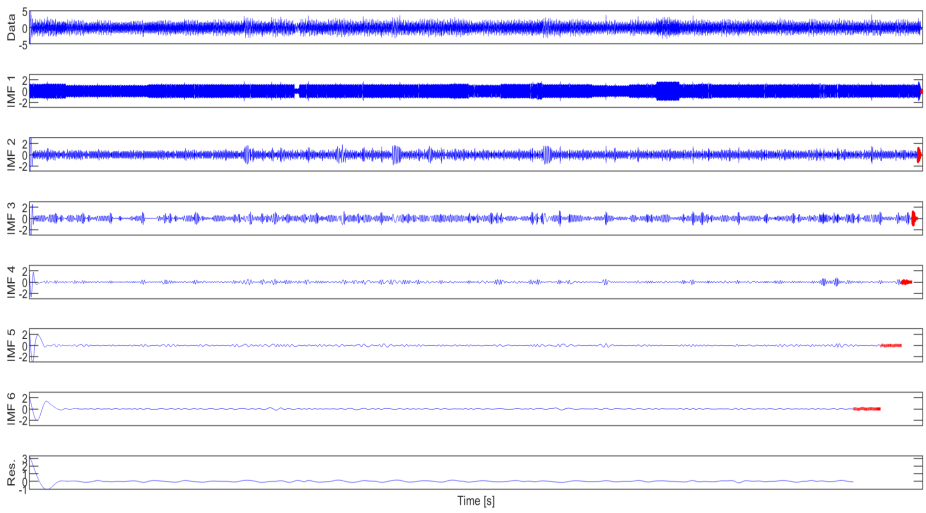

Figure 4.45: Resulting IMFs after applying Online EMD to $f_1(t)$

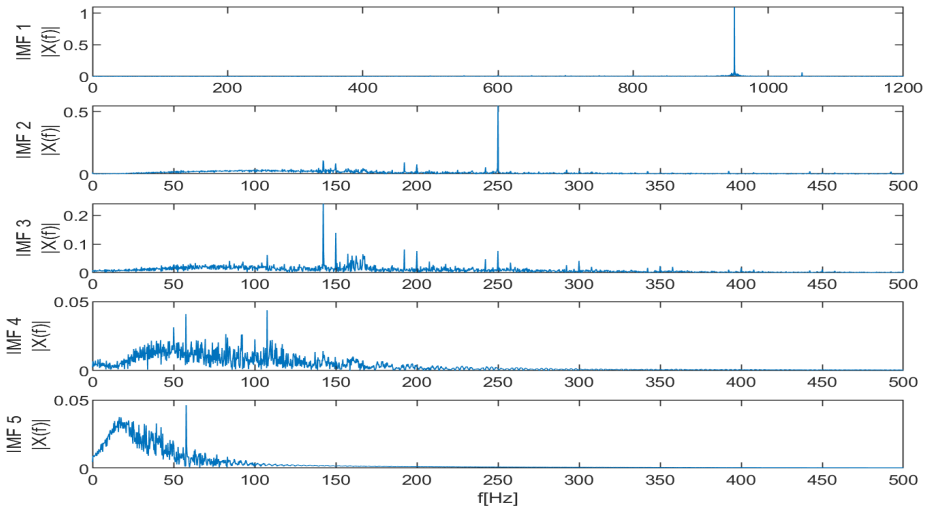

Figure 4.46: FFT of resulting IMFs after applying Online EMD to $f_1(t)$

4.3.2 Voltage measurement L12

In this section, signal $g(t)$ is analyzed using Online EMD. Snapshots from the decomposition process of the initial analysis can be seen in Figure 4.47. The first IMF represents the original signal causing the subsequent IMFs to contain very low amplitude noise components. As online EMD attempts to extract as many IMFs as possible, seeing each low amplitude point as extrema, the run-time is significantly increased. Therefore, the initial analysis is repeated, limiting the number of IMFs extracted to a maximum of three.

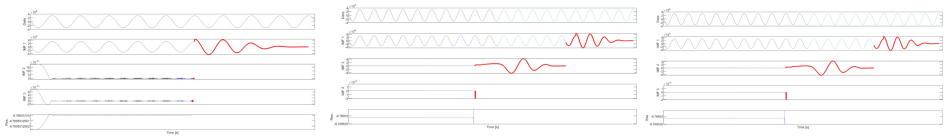

Figure 4.47: Online EMD applied to $L12$. From left to right, the total data points number 5120, 10240, and 20480. The black part of the signal is related to the first 5120 data points. The blue part is related to the parts 5120 to 10240, and teal is related to the parts from 10240 to 20480. Red indicates the parts of the IMFs still incomplete.

Initial analysis

The complete result of applying Online EMD with a maximum of three IMFs can be seen in Figure 4.48. The FFT of each IMF can be seen in 4.49. Online EMD seems to be unable to separate the low amplitude modes found in the initial FFT from the main 50 Hz component.

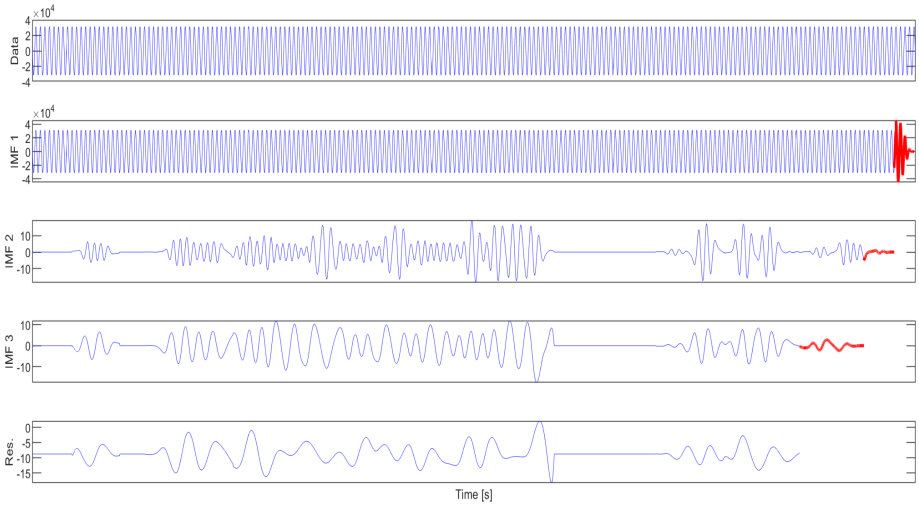

Figure 4.48: The resulting IMFs after applying Online EMD to $L12$

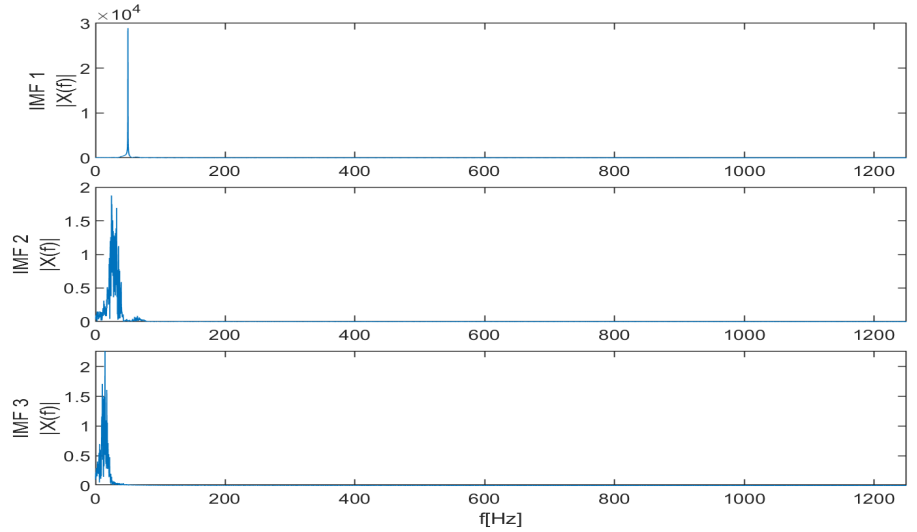

Figure 4.49: FFTs of the resulting IMFs after applying Online EMD to $g(t)$

By adding masking signal $g_{m1}(t)$, decomposition by Online EMD is attempted again. The IMFs can be seen in Figure 4.50, and the FFT of each IMF in Figure 4.51. $g(t)$ has now been decomposed into four relevant IMFs, the rest being residue.

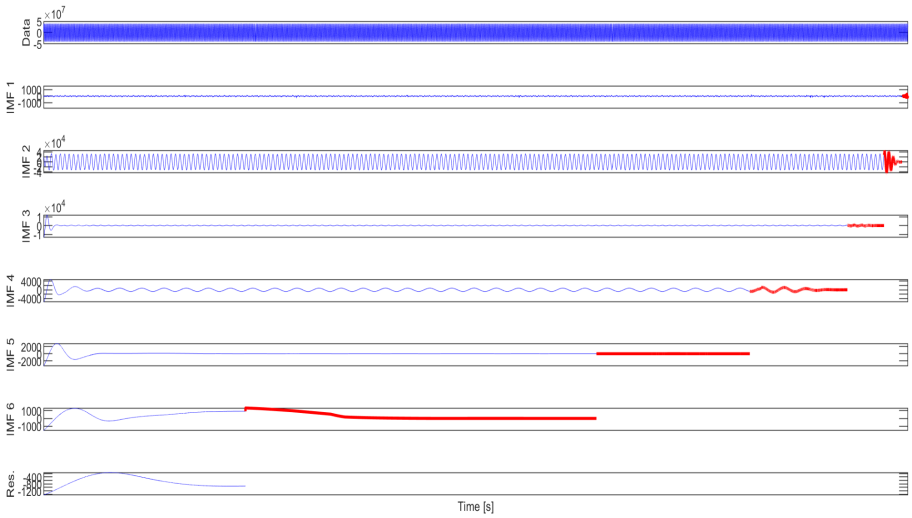

Figure 4.50: Resulting IMFs after applying masking signal $g_{m1}(t)$ to the Online EMD

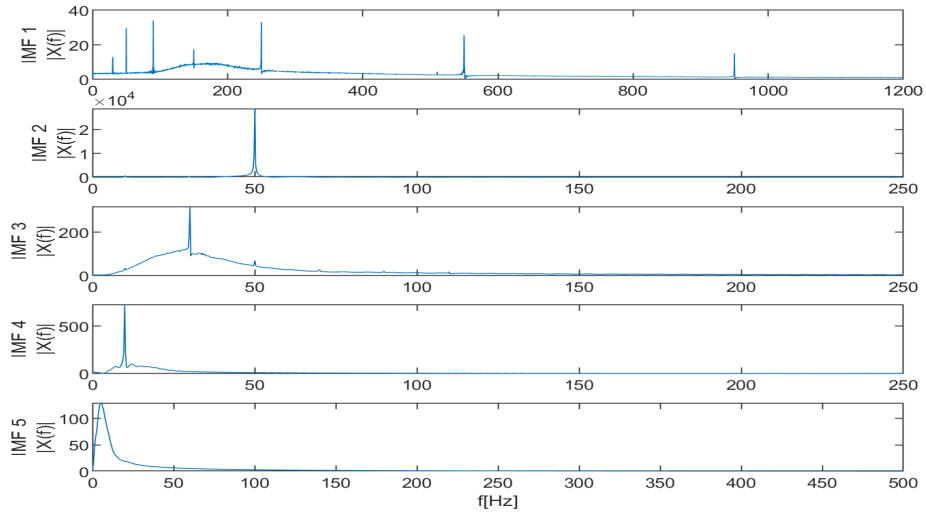

Figure 4.51: FFT of resulting IMFs after applying masking signal $g_{m1}(t)$ to the Online EMD

Again an over-separation of the 50 Hz component has occurred. This is evident in the amplitude modulation of IMF 2 matching that of the frequencies of IMF 3 and 4. When combined, these IMFs form a 50 Hz component without amplitude modulation. The combination of IMF 2-4 is seen as an adequately pure representation of the 50 Hz component, and it is treated as a final IMF. IMF 1 is now seen to contain a mix of several different frequencies, and further decomposition treats IMF 1 as the new input, $g_1(t) = IMF_{250}$.

Further decomposition of IMF 1

Applying Online EMD to $g_1(t)$ results in IMFs seen in Figure 4.52. The FFT of each IMF can be seen in Figure 4.53. Based on the FFTs, it seems the resulting IMFs are heavily mode-mixed.

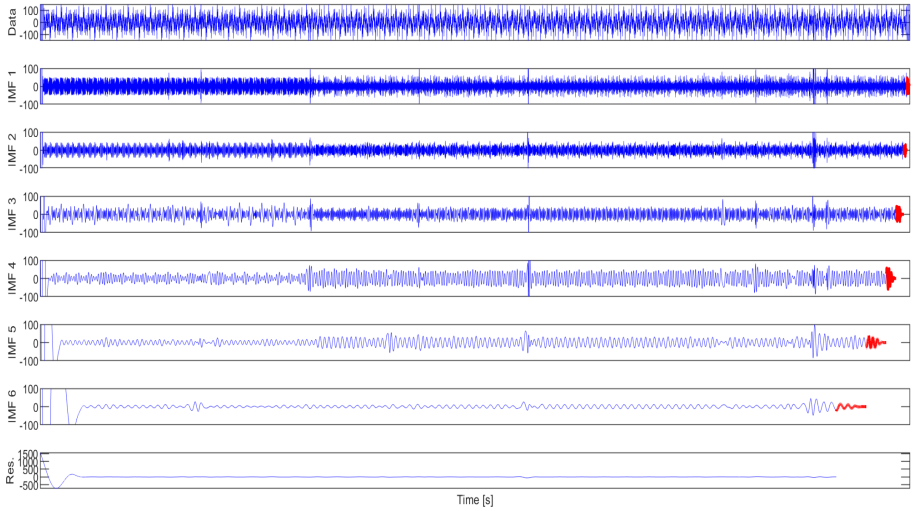

Figure 4.52: Resulting IMFs after applying Online EMD to $g_1(t)$

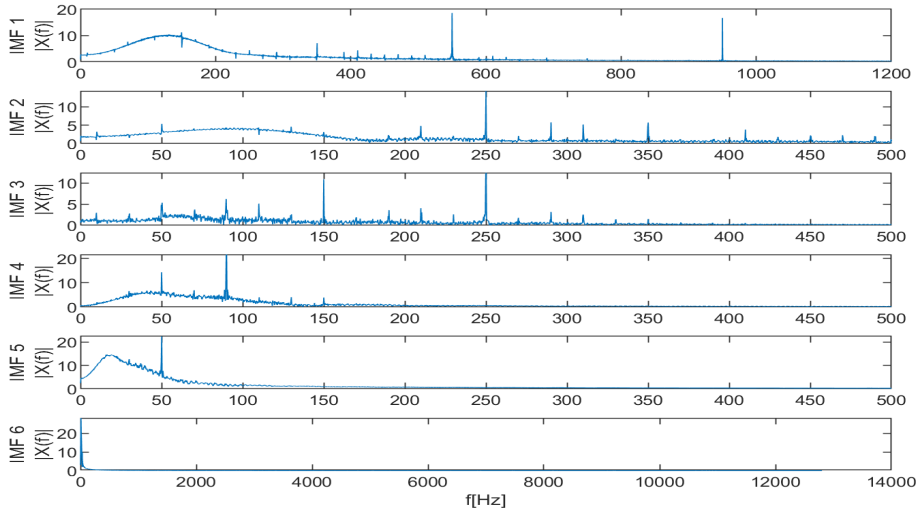

Figure 4.53: FFT of resulting IMFs after applying Online EMD to $g_1(t)$

Using masking signal $g_{m2}(t)$ a new decomposition is attempted, resulting in IMFs and

FFTs given in Figure 4.54 and 4.55. IMFs 1, 2, and 3 now appear to be pure representations of frequencies 950, 550, and 250 Hz, respectively. These are seen as adequately pure IMFs and are thus treated as final IMFs. While IMF 4 seems to properly separate a 90 Hz component, it is not included in the final IMFs, as this is a mode not detected in the original signal. IMF 4 and 5 are thus added to the residue in the final results.

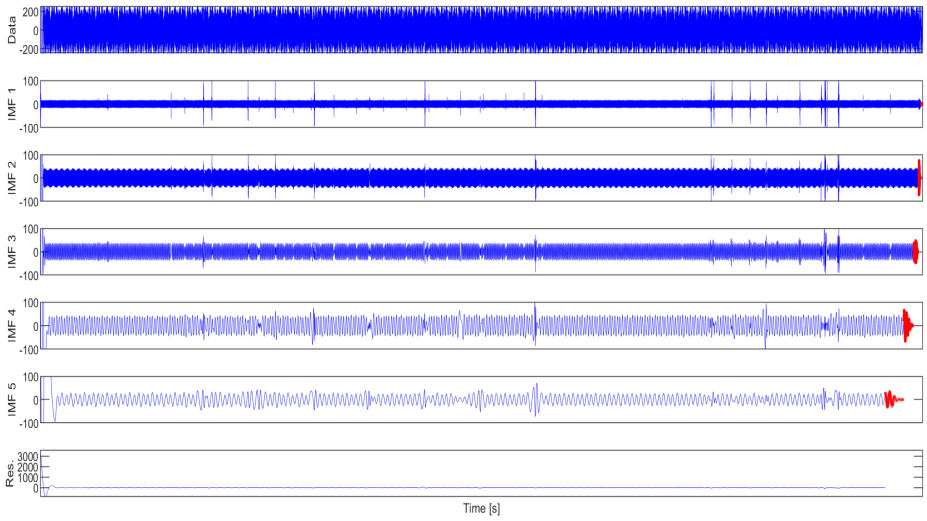

Figure 4.54: Resulting IMFs after adding masking signal g_{m2} to $g_1(t)$

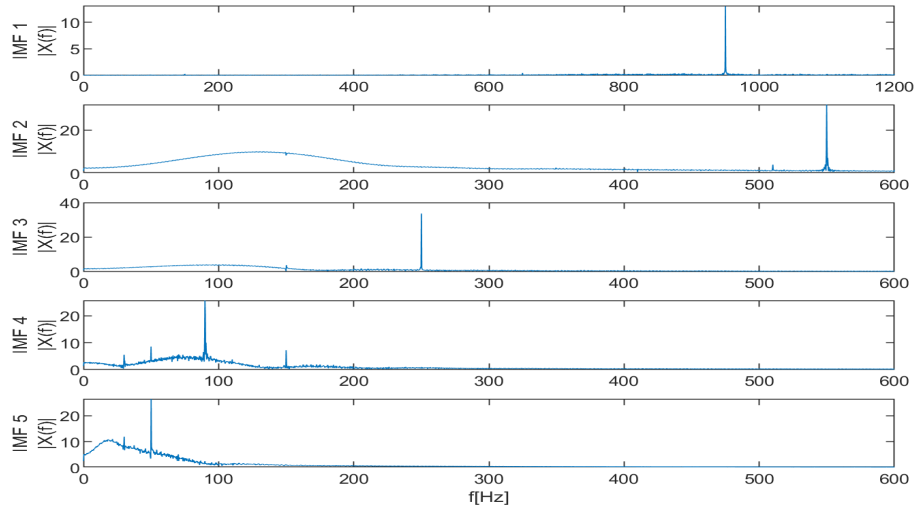

Figure 4.55: FFT of resulting IMFs after adding masking signal g_{m2} to $g_1(t)$

4.4 Results

This section contains all the resulting IMFs from the classical and Online EMD. The HT and FFT of each IMF are also presented. Appendix A includes a closer look at the IA and IF of the resulting IMFs.

4.4.1 Current measurement L1 - Classical EMD

The resulting IMFs for $L1$ using classical EMD as decomposition method can be seen in Figure 4.56. The results of applying FFT, and HT to find the IF and IA can be seen in Figure 4.57, 4.58 and 4.59 respectively.

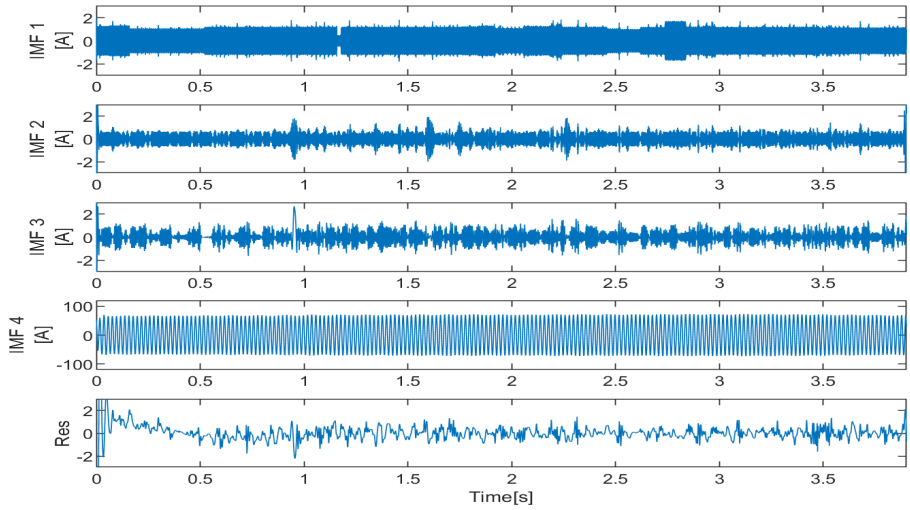

Figure 4.56: Final resulting IMFs for current measurement $L1$ using classical EMD.

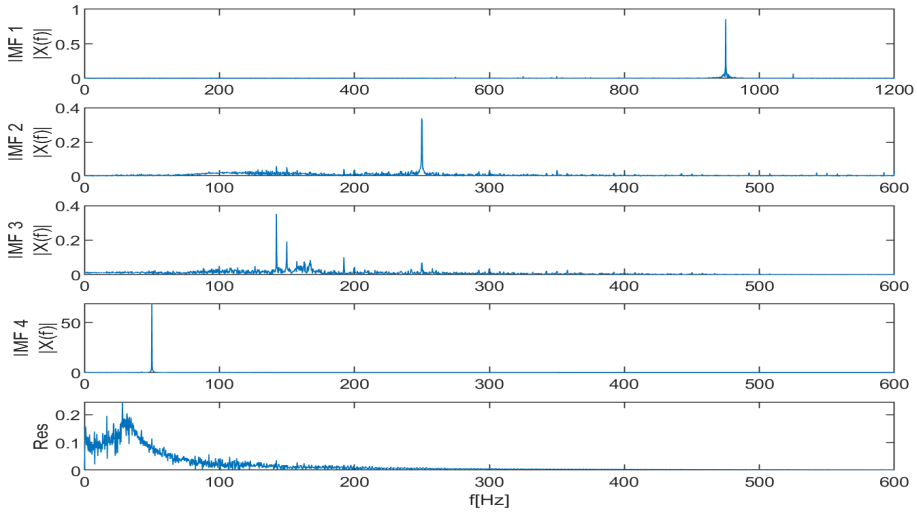

Figure 4.57: FFT of final resulting IMFs for current measurement $L1$ using classical EMD.

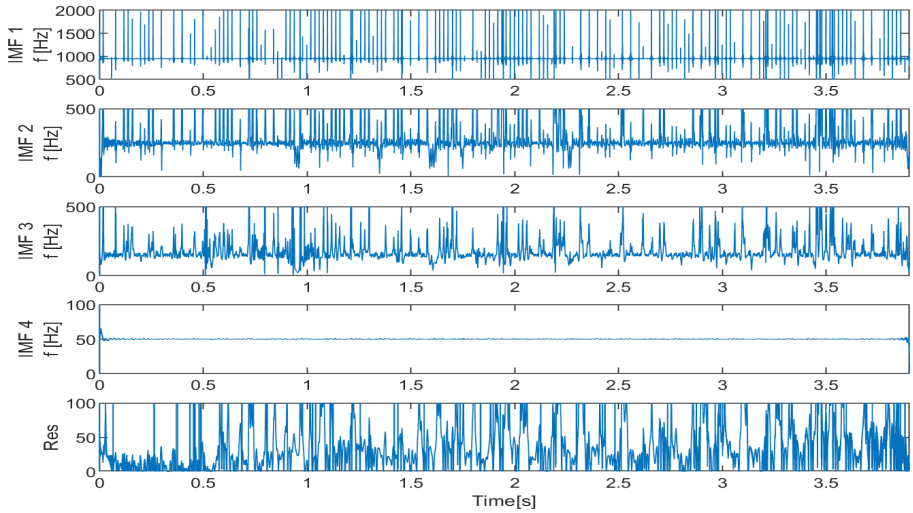

Figure 4.58: IF of final resulting IMFs for current measurement $L1$ using classical EMD.

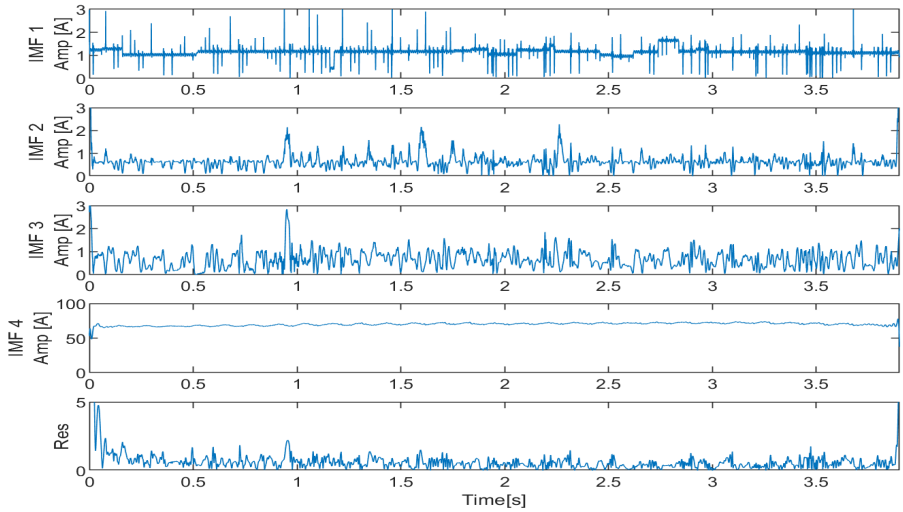

Figure 4.59: IA of final resulting IMFs for current measurement $L1$ using classical EMD.

4.4.2 Current measurement L1 - Online EMD

The resulting IMFs for $L1$ using Online EMD as decomposition method can be seen in Figure 4.60. The results of applying FFT, and HT to find the IF and IA can be seen in Figure 4.61, 4.62 and 4.63 respectively.

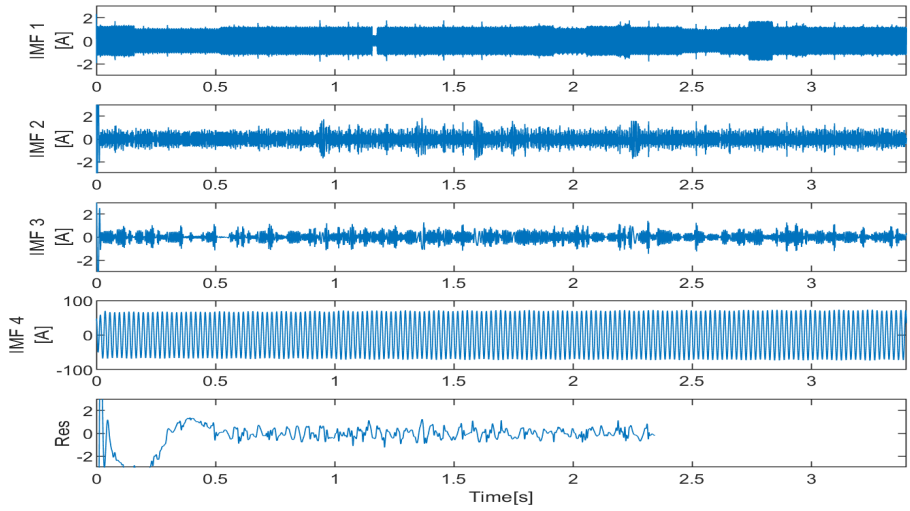

Figure 4.60: Final resulting IMFs for current measurement $L1$ using Online EMD.

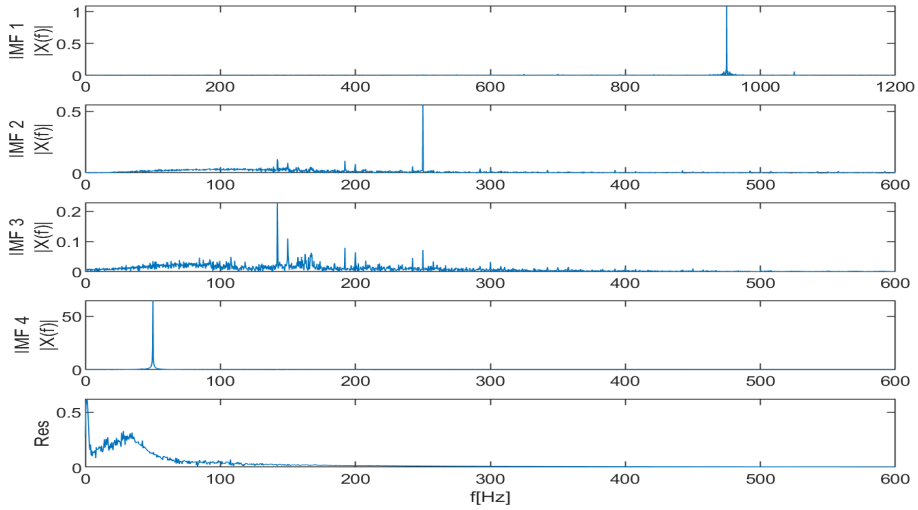

Figure 4.61: FFT of final resulting IMFs for current measurement $L1$ using classical EMD.

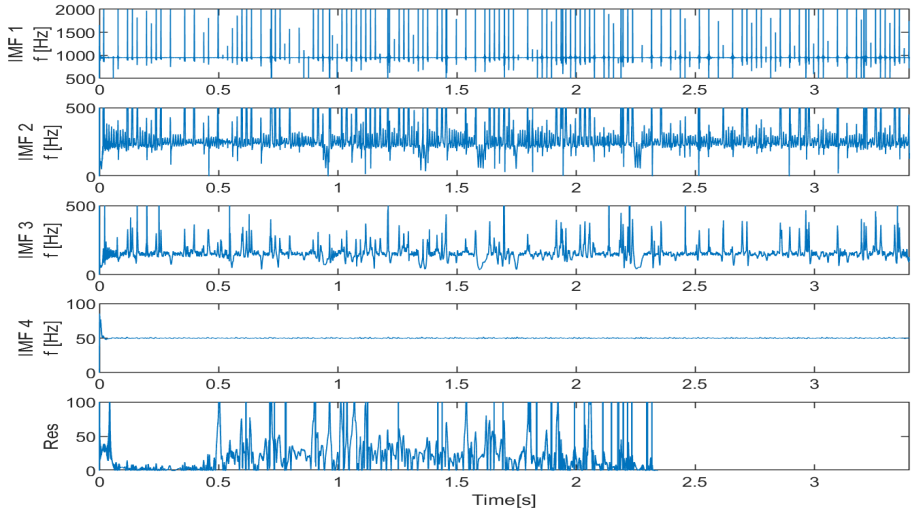

Figure 4.62: IF of final resulting IMFs for current measurement $L1$ using Online EMD.

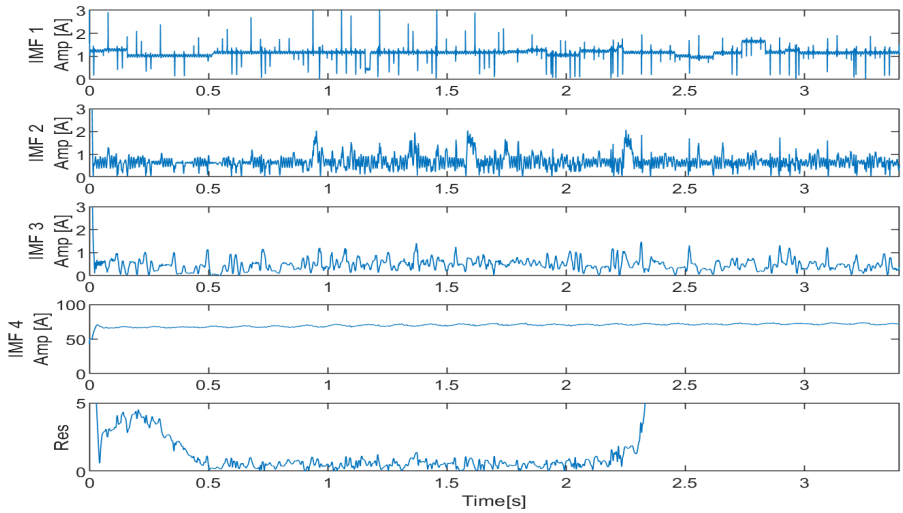

Figure 4.63: IA of final resulting IMFs for current measurement $L1$ using Online EMD.

4.4.3 Voltage measurement L12 - Classical EMD

The resulting IMFs for $L12$ using classical EMD as decomposition method can be seen in Figure 4.64. The results of applying FFT, and HT to find the IF and IA can be seen in Figure 4.66, 4.67 and 4.68 respectively.

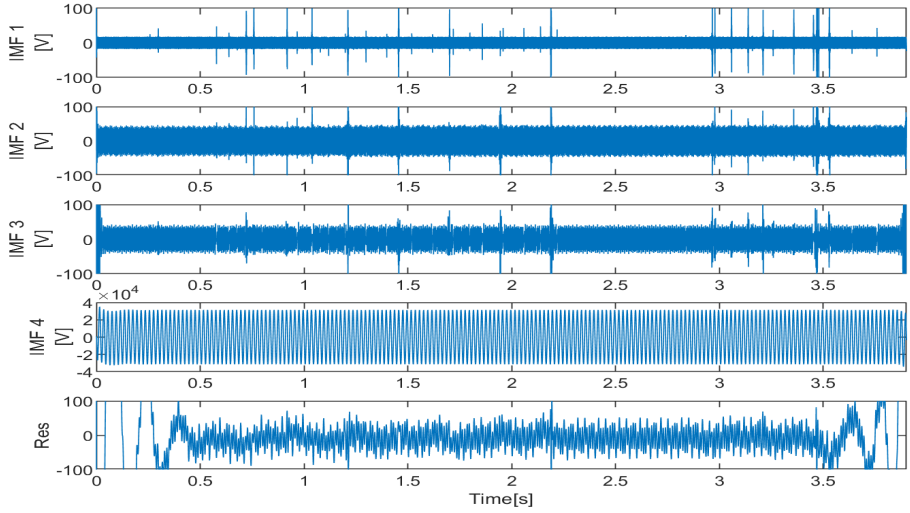

Figure 4.64: Final resulting IMFs for voltage measurement $L12$ using classical EMD.

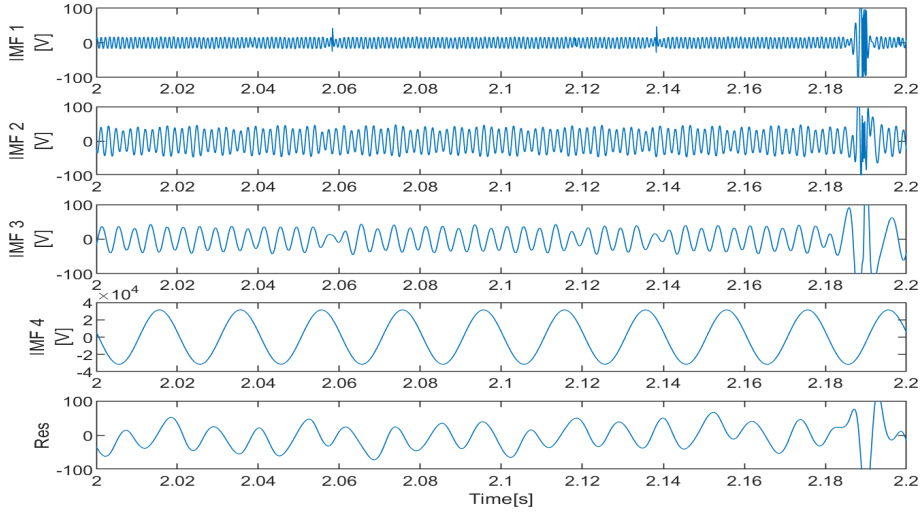

Figure 4.65: Close-up of the resulting IMFs for voltage measurement $L12$ using classical EMD.

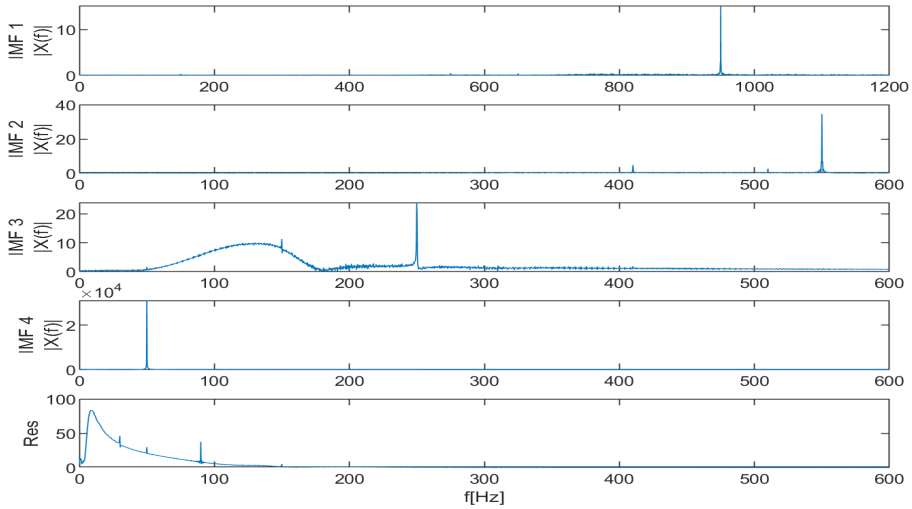

Figure 4.66: FFT of final resulting IMFs for voltage measurement $L12$ using classical EMD.

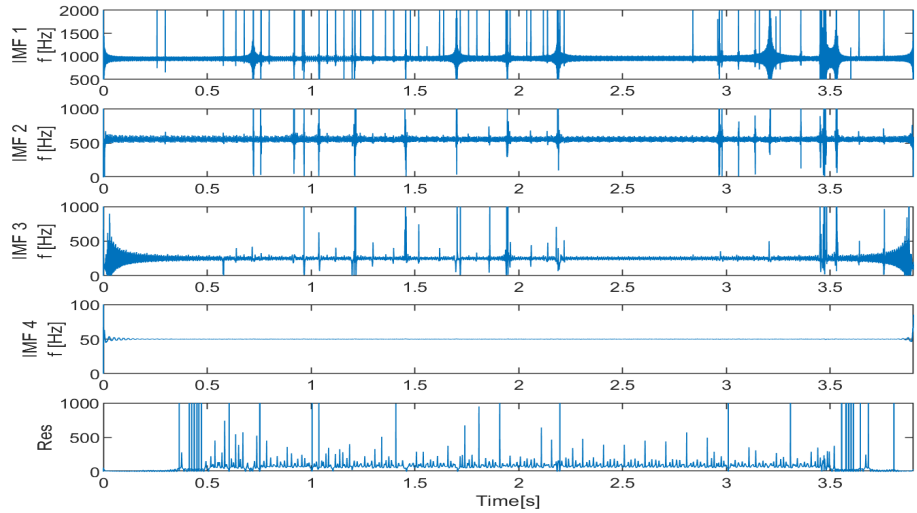

Figure 4.67: IF of final resulting IMFs for voltage measurement $L12$ using classical EMD.

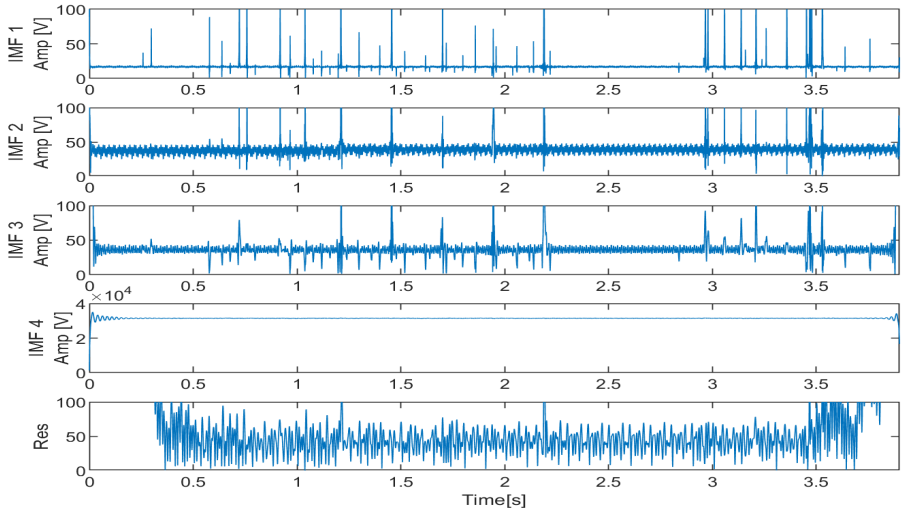

Figure 4.68: IA of final resulting IMFs for voltage measurement $L12$ using classical EMD.

4.4.4 Voltage measurement L12 - Online EMD

The resulting IMFs for $L12$ using Online EMD as decomposition method can be seen in Figure 4.69. The results of applying FFT, and HT to find the IF and IA can be seen in Figure 4.71, 4.72 and 4.73 respectively.

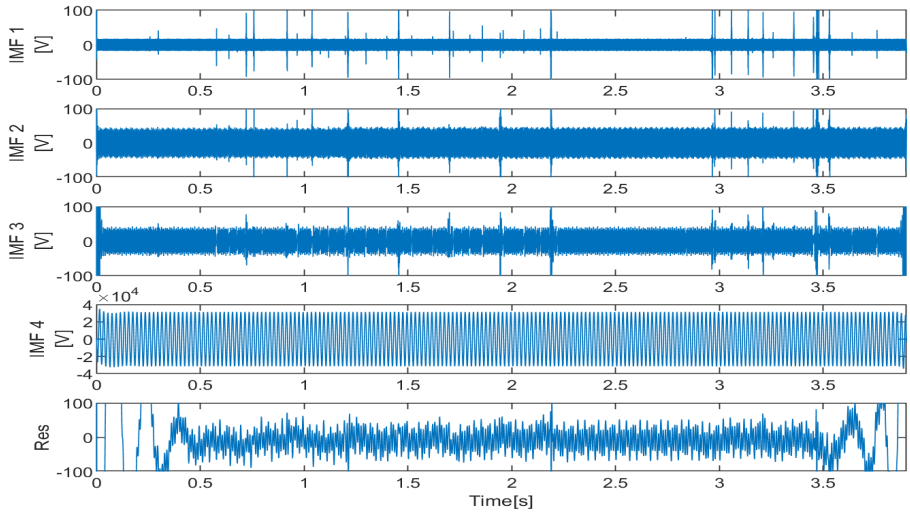

Figure 4.69: Final resulting IMFs for voltage measurement $L12$ using Online EMD.

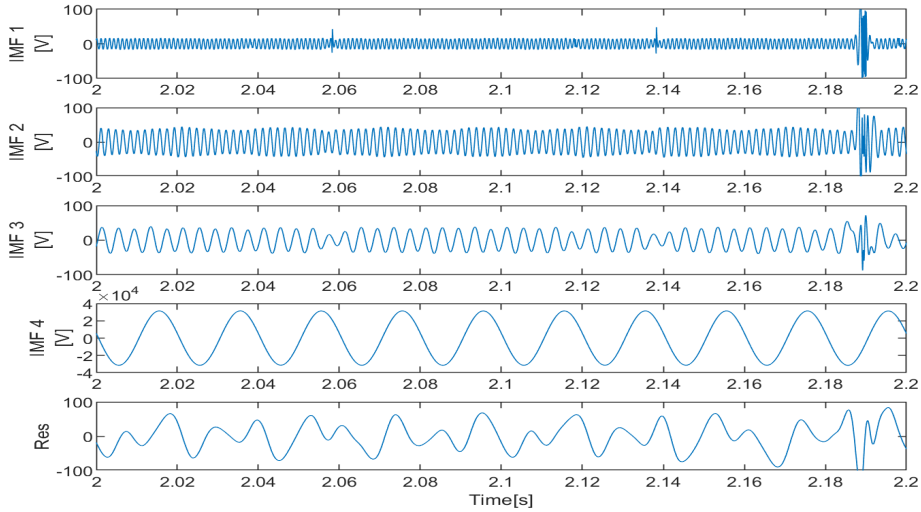

Figure 4.70: Closer look at the final resulting IMFs for voltage measurement $L12$ using Online EMD.

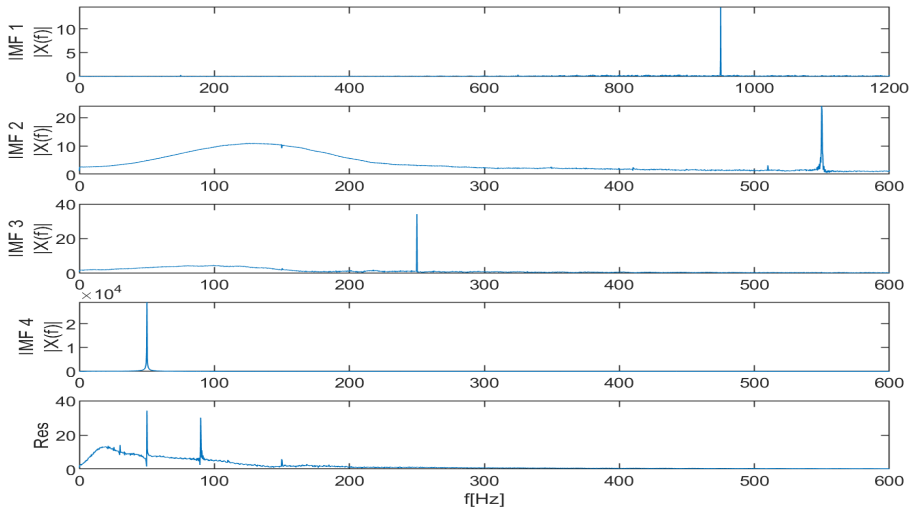

Figure 4.71: Closer look at the final resulting IMFs for voltage measurement $L12$ using Online EMD.

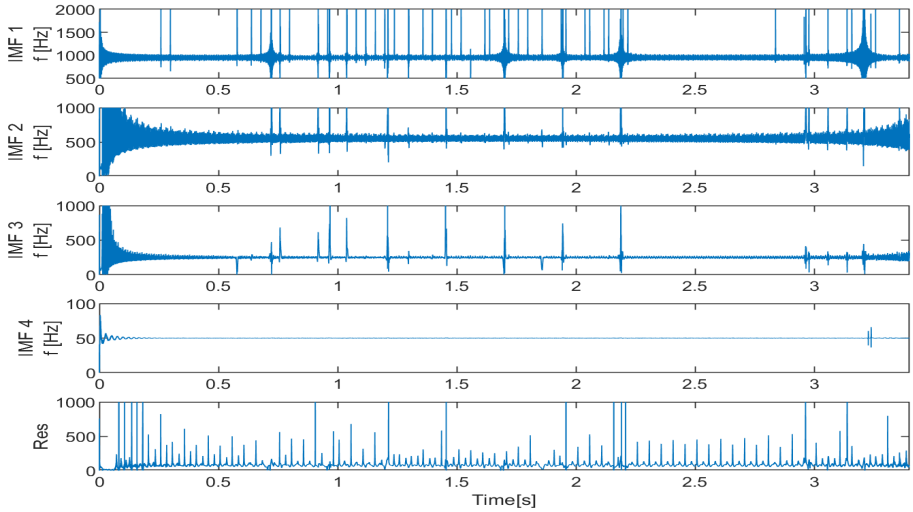

Figure 4.72: IF of final resulting IMFs for voltage measurement $L12$ using Online EMD.

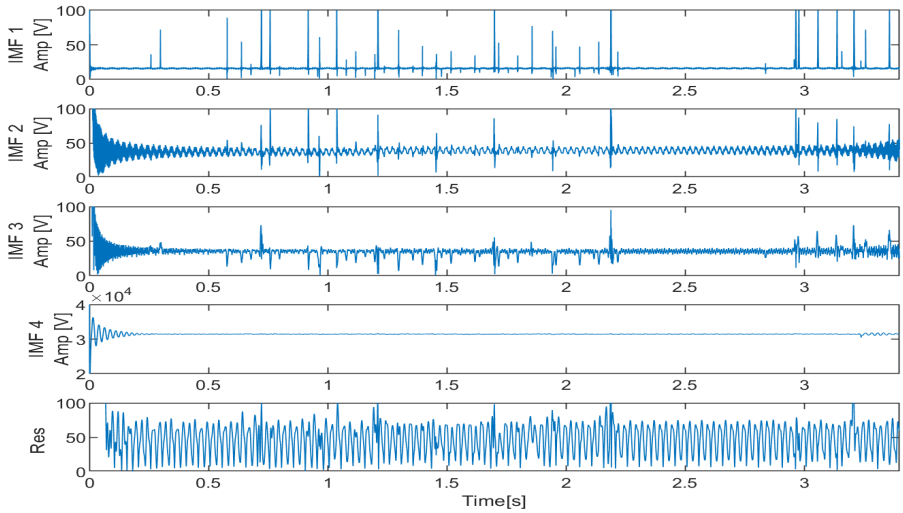

Figure 4.73: IA of final resulting IMFs for voltage measurement $L12$ using Online EMD.

4.5 Discussion

Applying classical EMD to the original current measurement L1 results in reasonably pure separation of the 50 Hz and 950 Hz component. However, further examination of the 50 Hz component reveals slight mode-mixing with frequencies discovered in the original signal using FFT. As the dominant 50 Hz component absorbs the relevant frequencies, the rest of the IMFs uncovered are left as low-frequency noise. After a more gradual approach using masking signals to extract IMFs with relevant modes of oscillation, the 19th, 5th, and a cluster of inter-harmonics are discovered in addition to the fundamental 50 Hz component. Initial visual inspection of the extracted IMFs does not yield immediately apparent conclusions. Thus further analysis using FFT and HT is required.

A closer look at IMF 1 reveals what appears to be a somewhat well-behaved sinusoid with slight amplitude modulation consistent throughout the entire signal duration. There are, however, more distinct instantaneous changes in amplitude occurring in the IMF, most prominent at $t = 1.2s$ and $t = 2.75s$. FFT of IMF 1 reveals the presence of a 1050 Hz frequency component of significantly lower amplitude than that of the 950 Hz component. As the amplitude of the IMF is seen to change over the signal duration, the amplitudes in the FFT does not necessarily represent the amplitude of each mode in the signal. Based on the FFT, it is not possible to determine whether the low amplitude of the 1050 Hz component is due to a low amplitude consistent in the entire signal or a high amplitude intermittence. However, as the resulting IF of IMF 1 seen in Figure 4.58 is relatively consistent throughout the entirety of the signal, the notion of a low amplitude 1050 Hz component being present for the entire signal duration seems reasonable. As the difference in frequency between 1050 and 950 Hz is relatively small, it is possible to attribute the amplitude modulations previously mentioned to the beat-effect of these two signals.

A closer look at the IF given in Figure 4.74 reveals, though distorted, frequency peaks regularly occurring in the IMF.

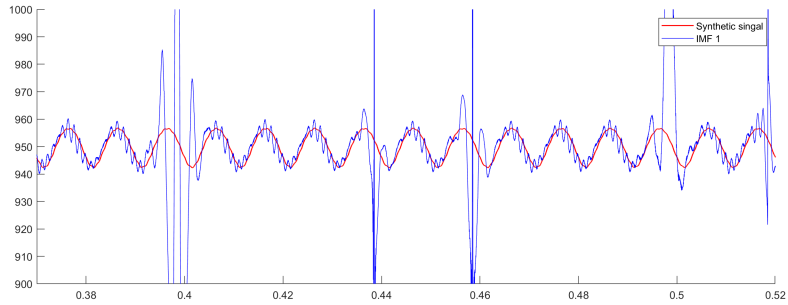

Figure 4.74: The frequency component of the HT for IMF 1 of signal $L1$ compared to the frequency component of the HT of a signal given by $cos(2\pi 950t) + 0.07cos(2\pi 1050t)$

This agrees with the patterns of mode-mixing mentioned in Section 2.4.5 as peaks in the

frequency of the HT occurs based on the difference between the frequencies mixed. By constructing a synthetic signal $cos(2\pi 950t) + 0.07cos(2\pi 1050t)$, where the amplitude of the 1050 Hz frequency component is based on the relative difference of the amplitudes in the FFT, it can be observed that the frequency component of the HT for IMF 1 matches that of a mode-mixed signal of frequencies 950 Hz and 1050 Hz. The IA of IMF 1 given in Figure 4.59, also shows clear instantaneous changes in amplitude. Due to the instantaneous nature of the changes, it seems unreasonable to contribute these changes to amplitude modulations naturally occurring in the signal or mode-mixing. Rather, it seems more likely that the changes are due to outside intervention of either mechanical or electrical nature.

By visual inspection of IMF 2 and IMF 3, it is apparent that these IMFs are more irregular than IMF 1. IMF 2 represents the 250 Hz component, and as mentioned in section 4.2.1, it shows signs of mode-mixing with IMF 3. The IMFs themselves indicate slight mode-mixing as each spike in IMF 2 relates to a reduction in IMF 3. There are also traces of activity in overlapping frequency ranges, as seen in the FFT in Figure 4.57. However, IMF 2 does appear relatively well behaved, and further investigation of the IF of IMF 2 does not reveal any meaningful patterns consistent with mode mixing. As such, the mode-mixing may be limited to intermittent bursts, explaining the low amplitude FFT and the IMF peaks. Thus IMF 2 is seen as a representation of a 250 Hz component will slight disturbances. IMF 3, however, is significantly more irregular than both IMF 1 and IMF 2. Based on the FFT, it appears to contain several inter-harmonics, the most notable frequencies being 142 Hz and 192 Hz. While this is likely to be noise, there have been reported instances of inter-harmonics concerning WTGs. Furthermore, this IMF contains a 150 Hz component noted in the initial analysis, also detected in voltage measurement $L12$. Thus the IMF is separate from the residue, as the components mixed have been previously noted in the analysis.

IMF 4 represents a 50 Hz frequency component. As the measurement is from a turbine connected to the Norwegian power grid operating at a frequency of 50 Hz, this component is expected. While this IMF appear well behaved, the IA, as seen in Figure 4.75 reveals a consistent amplitude modulation of frequency 8 Hz.

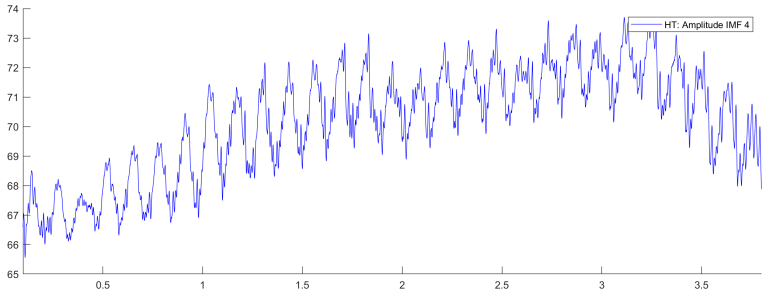

Figure 4.75: Closer look a the amplitude component of the HT for IMF 4 of signal $L1$

There is also a noticeable overall change in amplitude over the signal duration. Visual inspection of the IF of the IMF does not show the characteristic signs of mode-mixing, and FFT does not reveal other frequency components. Thus, the internal amplitude modulation is likely not a result of mode-mixing, but rather a part of the signal characteristic. As there is limited information regarding the surroundings of the turbine at the time the measurement is taken, the cause of the increase in current and its modulation is not immediately apparent. However, seeing as the voltage measured in signal $L12$ keeps relatively stable, this increase is possibly due to a load increase or adjustment in output.

The voltage measurement $L12$ has a significantly lower degree of harmonic pollution than the current $L1$. Looking at the initial measurement in Figure 4.20, no clear visual indication of harmonic disturbance is noted. This is also observed in the initial EMD, as it cannot separate or detect any relevant frequencies. However, the use of FFT reveals harmonic presence in the signal, previously hidden by the dominating 50 Hz frequency component. For further analysis using EMD, a masking signal is constructed based on the boundary condition map [28] and the large amplitude discrepancy between the fundamental and harmonic frequencies. The IMFs obtained after a more thorough analysis can be seen in Figure 4.64. The resulting IMFs represent the 19th, 11th, and 5th order harmonics. This agrees with the results from the current $L1$ where both the 19th and 5th order harmonics also appear. As there are no obvious visual signs of harmonic disturbance in $L12$ it seems likely to expect the harmonics uncovered in this signal to be relatively well behaved and of low amplitude.

IMF 1 represents a 950 Hz frequency component, also detected in current $L1$. However, this IMF is more well behaved than its counterpart. Both IF and IA, as seen in Figure 4.67 and 4.68 are relatively consistent throughout the signal duration, and apart from a slight modulation in amplitude, the IMF behaves as a near-perfect sinusoid. No signs of mode-mixing can be seen, and the FFT of the original $L12$ measurement shows no trace of a 1050 Hz frequency component. Therefore, the modulation in amplitude is not likely to be the result of mode-mixing, but rather characteristic to the signal itself.

IMF 2 and IMF 3 also contain very slight modulations in amplitude. These modulations can easily be detected in the IA seen in Figure 4.68. The FFT of IMF 3 seems to suffer from a high degree of mode-mixing with a component of frequency centered at 120 Hz. However, as mentioned in section 4.2.2, this peak can be attributed to the boundary condition error propagating at the ends of the IMF. It is seen that applying FFT to IMF 3 excluding the ends, results in an FFT only containing the 250 Hz frequency component. As none of the IMFs shows any clear signs of mode mixing in either FFT, IF, or IA, it seems unlikely these modulations are due to causes such as the beat-effect.

Overall, the results based on Online EMD are relatively similar to those of the classical EMD. Though the method of mode-mixing separation differs slightly as the online version simulates input as a data-stream, therefore not removing extracted IMFs from the original input, the methods are deemed similar enough to warrant a comparison of results. The immediately obvious difference is apparent in the residue of both plots. This difference is

expected as there is a delay to each subsequent IMF extracted for the Online EMD. Thus, when combining leftover IMFs, the residue is limited to the length of the shortest, i.e., last extracted IMF. However, some of the differences can also be attributed to mode-mixing and quality of decomposition, as all leftover noise and unsuccessful separation accumulate in the residue.

Looking at the actual IMFs, the difference between the Online and classical EMD is more subtle. There is a slight difference in the smoothness of the amplitude modulations, which is most visible in IMF 2 for voltage $L12$ as seen in Figure 4.65 and 4.70. Here the Online EMD is seen to have a much more discinct modulation, while the classical EMD seems somewhat irregular. However, applying HT and FFT on each IMF ultimately yields matching results. In general, it appears the Online version is as adept at signal decomposition as the classical EMD, even for complex signals. Based on the smoother, more distinct amplitude modulations, it is even possible to argue the Online EMD does a better job when dealing with noise, as the smoothing-effect of the averaging process might cancel out some of the disturbances. Furthermore, the use of masking signals to handle mode-mixing is seen to be effective for mode-mixing separation even when applied to the Online EMD.

Based on the IF plots, there seems to be a small internal frequency in each IMF. However, as these modulations in frequency seem to be very consistent and not inherently noticeable in the IMFs, they could be contributed to the HT itself. As the combination of EMD and HT is based on empirical separation and mathematical transformation used in conjunction, some inaccuracies are to be expected when applied to complex signals. While the results from this method have proven to give overall solid results uncovering much of the signal characteristics, it can be counter-productive to put too much trust in the details of the IA and IF. As mentioned, the notion of instantaneous frequency is still highly controversial, and patterns seen in the output can often be contributed to the nature of the transformation itself. This, combined with altering the input by applying masking signals, can give results that are too fragmented, not necessarily representing physically meaningful information. Thus, it can be advantageous to compare the results obtained to the results expected before the analysis. There are many causes of harmonics in WTGs. One possibility is harmonic current generation due to the soft starter installed in the turbine to reduce in-rush-current during startup. This harmonic current is, however, low in magnitude and usually has a short duration. Harmonic currents are often caused by the transformer during energization, resulting in a considerable amount of low-order harmonics. As the transformer usually is set to operate close to the saturation point, the nonlinear relationship between the voltage and current, especially given over-voltage condition, can cause harmonic distortion in the resulting output. Generally, this phenomenon is related to odd harmonics, and as delta windings block triplen harmonics, the harmonic content reported in WTG are of the orders 5th, 7th, 11th, 13th, 17th, 19th and so on—i.e., those of orders 6k $\pm$ 1, where k is an integer [31]. This is consistent with the results in this analysis. The 19th and 5th order harmonic is extracted from $L1$ and the 19th, 11th, and 5th order harmonics from $L12$. The presence of inter-harmonics is also noted in IMF 3 for current measurement $L1$. While it has been noted that the harmonic content can vary

based on the wind speeds as the size of the capacitor compensation is related to the power [32], there is no clear link to the amplitude modulation seen in the uncovered harmonics in this analysis.

Chapter 5

Conclusion and Future Work

In this master's thesis, different methods for identifying and tracking the instantaneous frequencies and amplitudes in microgrids have been presented. First, a brief general introduction is given for the concept of microgrids and harmonics in the power system, followed by a more thorough theoretical background for the FFT, HT, EMD, and Online EMD. A comparison of the decomposition quality of the EMD and Online EMD is made through the analysis of synthetic signals. When applied to a three-tone superimposed signal, the decomposition quality of the Online EMD is seen to converge to the decomposition quality of the classical EMD using identical stoppage criteria. For lower values of window size, the Online EMD has a slightly worse decomposition quality but is seen to outperform the classic version for $l = 13$. As a disturbance is added to the signal, there is no clear relationship between the online and classical versions. However, Online EMD is seen to result in slightly better decomposition for lower window sizes compared to the classical EMD using identical stoppage criteria, but as the window size increases, the decomposition quality declines.

These methods are then used to identify the harmonic content in an actual voltage and current measurement taken from a WTG. The measurements are decomposed using both EMD and Online EMD and are further analyzed by FFT and HT. Using FFT for frequency identification to construct appropriate masking signals proved to be highly effective when used in conjunction with a boundary condition map. While there are traces of inter-harmonics in IMF 3 of current measurement $L1$, the separation of modes using classical EMD is deemed satisfactory. This is also the case for Online EMD. As such, the usage of masking signals for mode-mixing separation can be considered effective when adapted to the Online EMD. The findings based on classical and Online EMD proved to be similar enough to warrant an identical conclusion. Thus the Online EMD is deemed to be a suitable alternative to the classical version when real-time identification or processing power is of the essence.

However, some problems and findings have been mentioned but left unanswered and are

thus suggested as topics for future work:

- This thesis addressed decomposition quality and mode-mixing related to the Online EMD, it is thus suggested by the author to further study the time-delay associated with the decomposition using Online EMD.
- The method used for frequency identification to construct masking signals is here the FFT, it is suggested to investigate the use of other more dynamic methods capable of detecting amplitudes more effectively when used in conjunction with the EMD.
- The use of masking signals proved to be effective for mode-mixing separation also in the Online EMD. However, the author suggests further study into alternative mode-mixing separation methods as the construction of masking signals requires extensive knowledge of the signal characteristic and requires more processing power.
- Finally, it is suggested to study further the amplitude modulations discovered in the uncovered IMFs, especially the more instantaneous changes in IMF 1 of $L1$ as they appear to be influenced by outside intervention.

Bibliography

[1] E. Westad, "Harmonic management through adaptive data analysis," *Specialization Project TET4520, Department of Electric Power Engineering, NTNU – Norwegian University of Science and Technology*, Dec 2019. doi:10.13140/RG.2.2.27771.75046.

[2] B. Hillenbrand, G. Kulia, and M. Molinas, "Impact of time varying angular frequency on the separation of instantaneous power components in stand-alone power systems," *6th IEEE International Conference on Clean Electrical Power*, July 2017.

[3] M. Lopez, M. Molinas, and G. Kulia, "Understanding instantaneous frequency detection: A discussion of hilbert-huang transform versus wavelet transform," *International Work-Conference on Time Series Analysis*, Sept 2017.

[4] "IEEE Recommended Practice and Requirements for Harmonic Control in Electric Power Systems," *IEEE Std 519-2014 (Revision of IEEE Std 519-1992)*, pp. 1–29, June 2014.

[5] "IEC Standard 61000-4-7: General guide on harmonics and inter-harmonics measurements and measuring instruments for power supply networks and attached devices used for the measurements."

[6] Gunther, "Harmonic and interharmonic measurement according to ieee 519 and iec 61000-4-7," *2005/2006 IEEE/PES Transmission and Distribution Conference and Exhibition*, pp. 223–225, May 2006.

[7] T. Tarasiuk, "Angular frequency variations at microgrids and its impact on measuring instruments performance," *IET Generation, Transmission Distribution*, vol. 10, no. 13, pp. 3234–3240, 2016.

[8] G. Kulia, M. Molinas, L. Lundheim, and B. Larsen, "Towards a real-time measurement platform for microgrids in isolated communities," *Humanitarian Technology: Science, Systems and Global Impact*, June 2016.

[9] D. Ton and M. Smith, "The u.s. department of energy's microgrid initiative," *The Electricity Journal*, vol. 25, p. 84–94, Oct 2012.

[10] W. Bower, D. Ton, R. Guttromson, S. Glover, J. Stamp, D. Bhatnagar, and J. Reilly, "The advanced microgrid integration and interoperability," *Sandia National Laboratories*, 2014.

[11] O. Dag and B. Mirafzal, "On stability of islanded low-inertia microgrids," *Clemson University Power Systems Conference (PSC)*, pp. 1–7, 2016.

[12] D. Chapman, "Application note - harmonics: Causes and effects," *European Copper Institute*, 2011.

[13] N. Mohan, T. M. Undeland, and W. P. Robbins, *Power Electronics - Converters, Applications, and Design*. Wiley, 3 ed., 2003.

[14] J. W. Cooley and J. W. Tukey, "An algorithm for the machine calculation of complex fourier series," *Mathematics of Computation*, vol. 19, pp. 297–301, Apr 1965.

[15] J. Cooley, P. Lewis, and P. Welch, "Historical notes on the fast fourier transform," *IEEE Transactions on Audio and Electroacoustics*, vol. 15, pp. 76–79, June 1967.

[16] M. Molinas, "Lecture material, TTK7 - Adaptive Data Analysis, NTNU - Norwegian University of Science and Technology," fall 2019.

[17] W. T. Cochran, J. W. Cooley, D. L. Favin, H. D. Helms, R. A. Kaenel, W. W. Lang, G. C. Maling, D. E. Nelson, C. M. Rader, and P. D. Welch, "What is the fast fourier transform?," *Proceedings of the IEEE*, vol. 55, pp. 1664–1674, Oct 1967.

[18] M. Feldman, *Hilbert Transform Applications in Mechanical Vibration*, ch. 1, pp. 1–6. John Wiley & Sons, Ltd, 2011.

[19] N. E. H. et al, "The empirical mode decomposition and the hilbert spectrum for nonlinear and non-stationary time series analysis," *Proceedings of the Royal Society of London. Series A: Mathematical, Physical and Engineering Sciences*, vol. 454, pp. 903–995, Mar 1998.

[20] R. Faltermeier, A. Zeiler, A. Tomé, A. Brawanski, and E. Lang, "Weighted sliding empirical mode decomposition," *AADA*, vol. 3, pp. 509–526, Aug 2011.

[21] K. Coughlin and K. Tung, "11-year solar cycle in the stratosphere extracted by the empirical mode decomposition method," *Advances in Space Research*, vol. 34, pp. 323–329, Feb 2004.

[22] E. Souza Neto, M. Custaud, J.-C. Cejka, P. Abry, J. Frutoso, C. Gharib, and P. Flandrin, "Assessment of cardiovascular autonomic control by the empirical mode decomposition," *Methods of information in medicine*, vol. 43, pp. 60–5, Feb 2004.

[23] R. Fontugne, N. Tremblay, P. Borgnat, P. Flandrin, and H. Esaki, "Mining anomalous electricity consumption using ensemble empirical mode decomposition," *International Conference on Acoustics, Speech, and Signal Processing, ICASSP-88*, pp. 5238–5242, Oct 2013.

[24] G. Rilling, P. Flandrin, and P. Gonçalves, "On empirical mode decomposition and its algorithms," *Proceedings of IEEE-EURASIP Workshop on Nonlinear Signal and Image Processing NSIP-03*, vol. 3, June 2003.

[25] A. Zeiler, R. Faltermeier, I. Keck, A. Tomé, C. Puntonet, and E. Lang, "Empirical mode decomposition - an introduction," *Proceedings of the International Joint Conference on Neural Networks*, pp. 1–8, 07 2010.

[26] Z. Yang, L. Yang, C. Qing, and D. Huang, "A method to eliminate riding waves appearing in the empirical am/fm demodulation," *Digital Signal Processing*, vol. 18, no. 4, pp. 488 – 504, 2008.

[27] G. Rilling and P. Flandrin, "One or two frequencies? the empirical mode decomposition answers," *IEEE Transactions on Signal Processing*, vol. 56, pp. 85–95, Jan 2008.

[28] O. Fosso and M. Molinas, "Emd mode mixing separation of signals with close spectral proximity in smart grids," *IEEE PES ISGT Europe 2018 - 8th IEEE PES Innovative Smart Grid Technologies*, Oct 2018.

[29] R. Fontugne, P. Borgnat, and P. Flandrin, "Online empirical mode decomposition," *IEEE International Conference on Acoustics, Speech and Signal Processing (ICASSP)*, pp. 4306–4310, Mar 2017.

[30] R. Fontugne, P. Borgnat, and P. Flandrin, "MATLAB Implementation of Online EMD." `https://github.com/romain-fontugne/onlineEMD`.

[31] J. Arrillaga and R. Watson, N, *Power System Harmonics*, pp. 290–304. John Wiley & Sons, Ltd, 2 ed., 2004.

[32] V. Preciado, M. Madrigal, E. Muljadi, and V. Gevorgian, "Harmonics in a wind power plant," *2015 IEEE Power and Energy Society General Meeting*, Apr 2015.

Appendix

This section contains the IF and IA of every step of the decomposition by classical EMD for both $L1$ and $L12$. It also includes a closer look a the resulting IA and IF, and a recreation of the original signal using the resulting IMF.

A.1 Current Measurement L1

A.1.1 Initial analysis

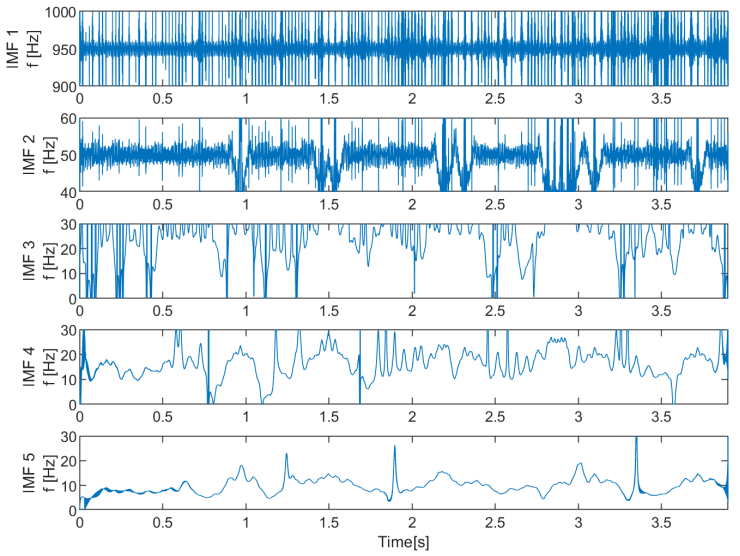

Figure A.1: IF of the IMFs from the EMD applied to $f(t)$.

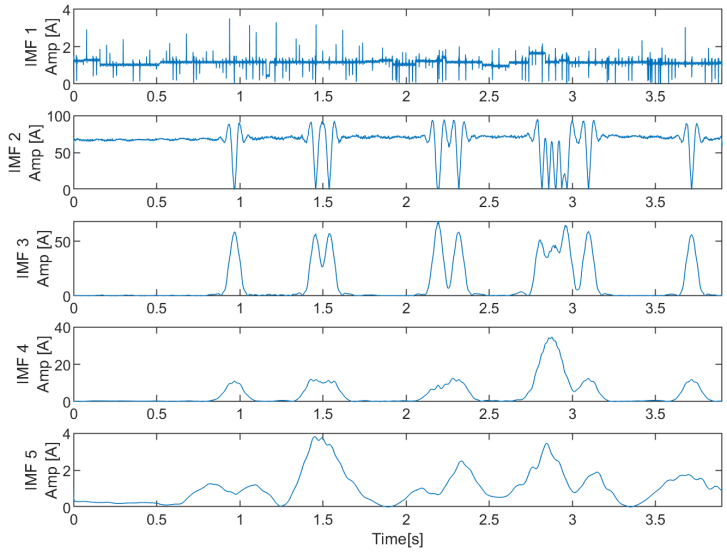

Figure A.2: IA of the IMFs from the EMD applied to $f(t)$.

A.1.2 After Applying Mask fm1

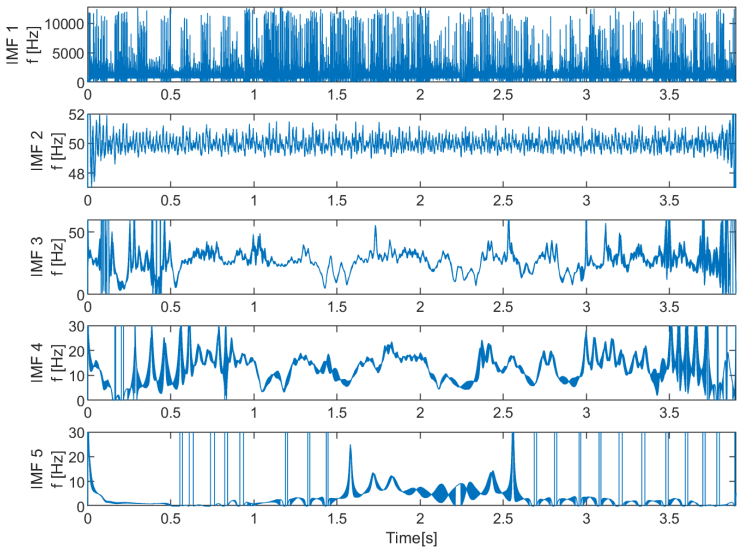

Figure A.3: IF of IMFs after adding masking signal $f_{m1}(t)$ to $f(t)$.

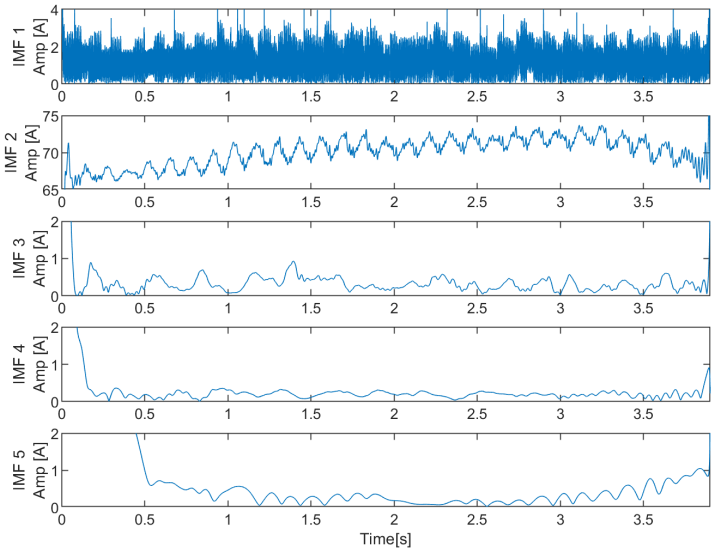

Figure A.4: IA of IMFs after adding masking signal $f_{m1}(t)$ to $f(t)$.

A.1.3 After extraction of the 50 Hz Component

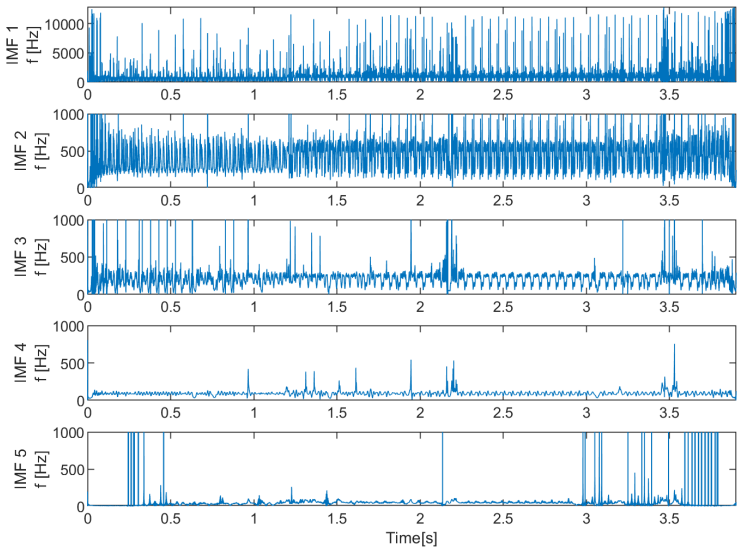

Figure A.5: IF of the IMFs from the EMD applied to $f_1(t)$.

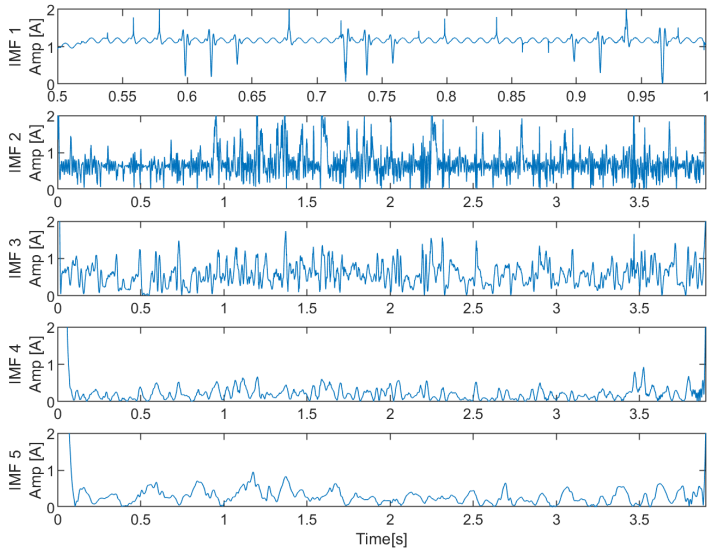

Figure A.6: IA of the IMFs from the EMD applied to $f_1(t)$.

A.1.4 After extraction of the 50 Hz and 950 Hz Component

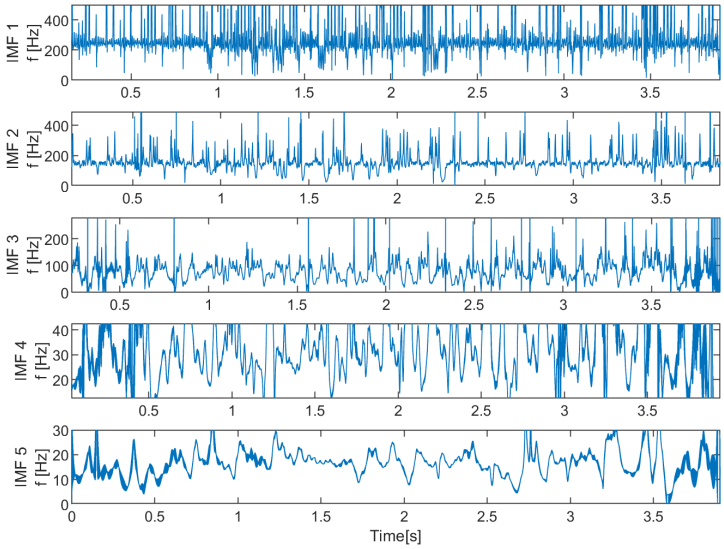

Figure A.7: IF of the IMFs from the EMD applied to $f_2(t)$.

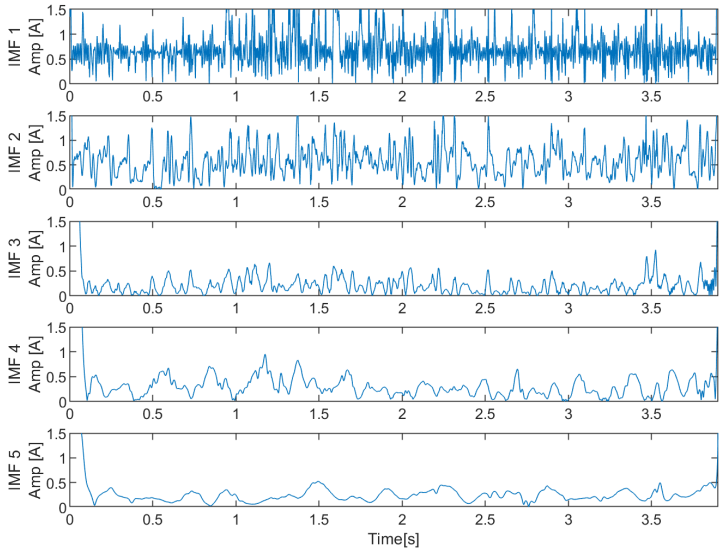

Figure A.8: IA of the IMFs from the EMD applied to $f_2(t)$.

A.1.5 After Applying Mask fm2

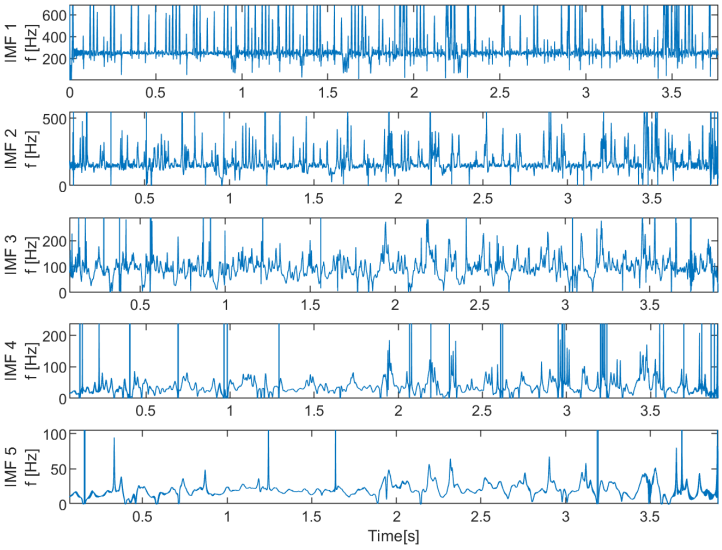

Figure A.9: IF of IMFs after adding masking signal $f_{m2}(t)$ to $f_2(t)$.

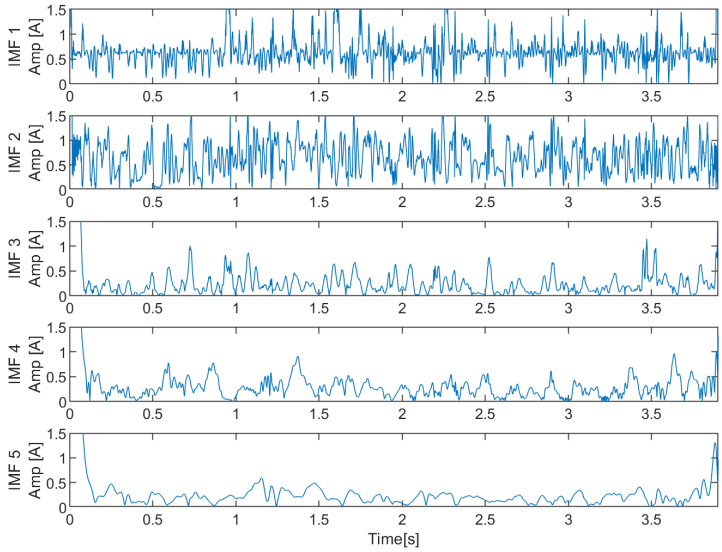

Figure A.10: IA of IMFs after adding masking signal $f_{m2}(t)$ to $f_2(t)$.

A.1.6 Resulting IMFs

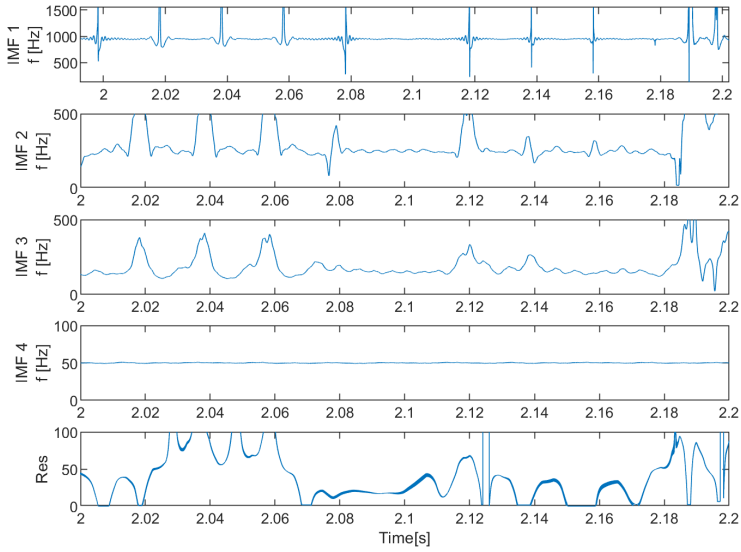

Figure A.11: Closer look at the IF of resulting IMFs of $f(t)$.

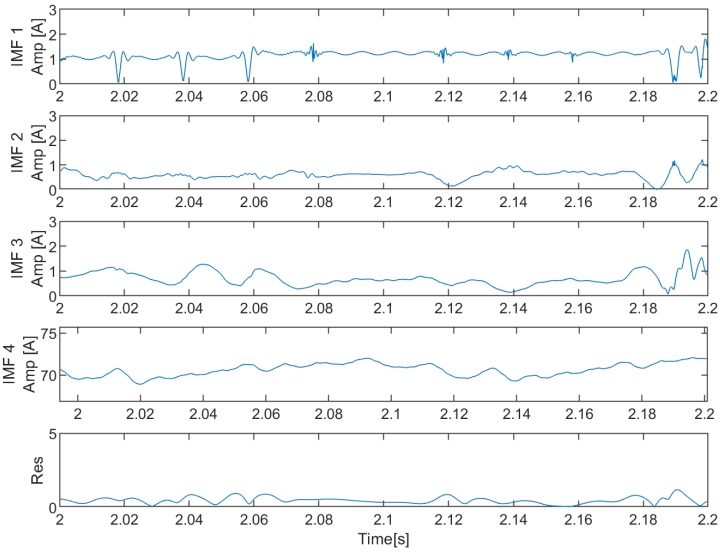

Figure A.12: Closer look at the IA of resulting IMFs of $f(t)$.

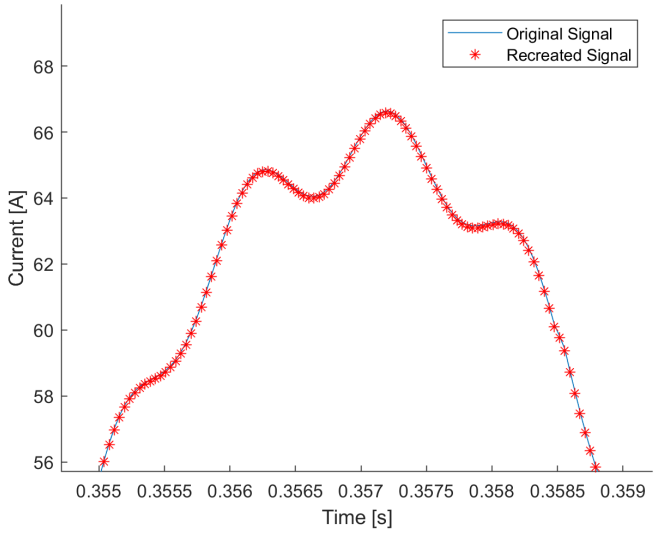

Figure A.13: Recreation of original signal $f(t)$ from the resulting IMFs.

A.2 Voltage Measurement L12

A.2.1 Initial analysis

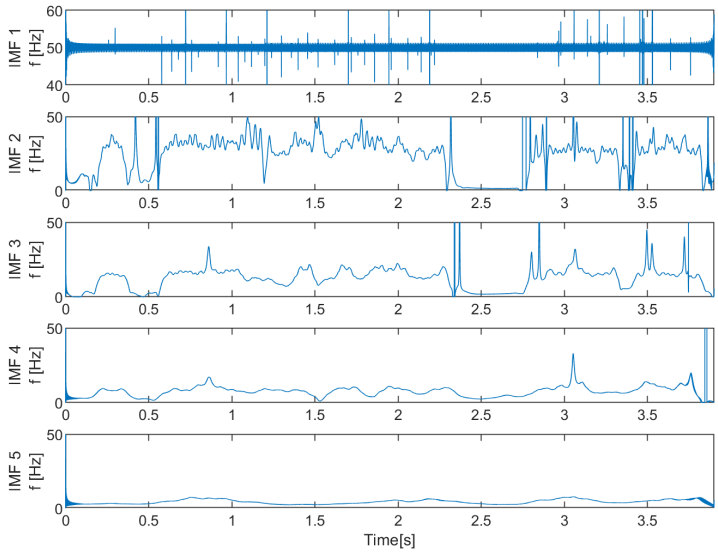

Figure A.14: IF of the IMFs from the EMD applied to $g(t)$.

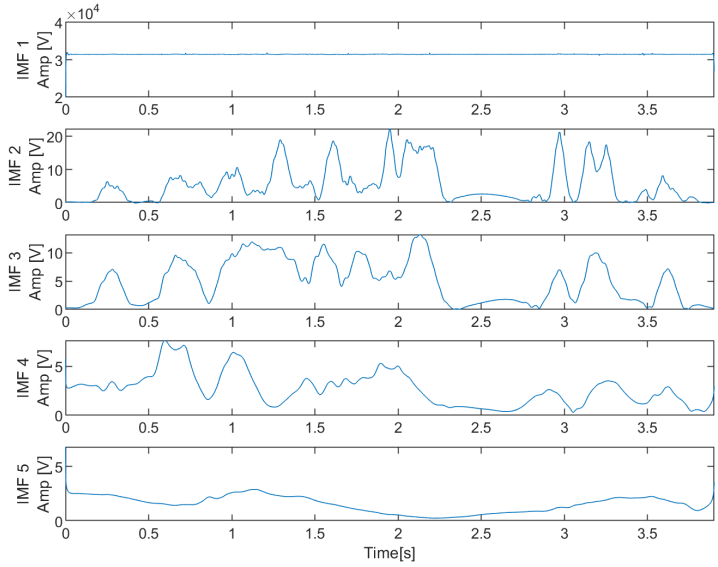

Figure A.15: IA of the IMFs from the EMD applied to $g(t)$.

A.2.2 After Applying Mask gm1

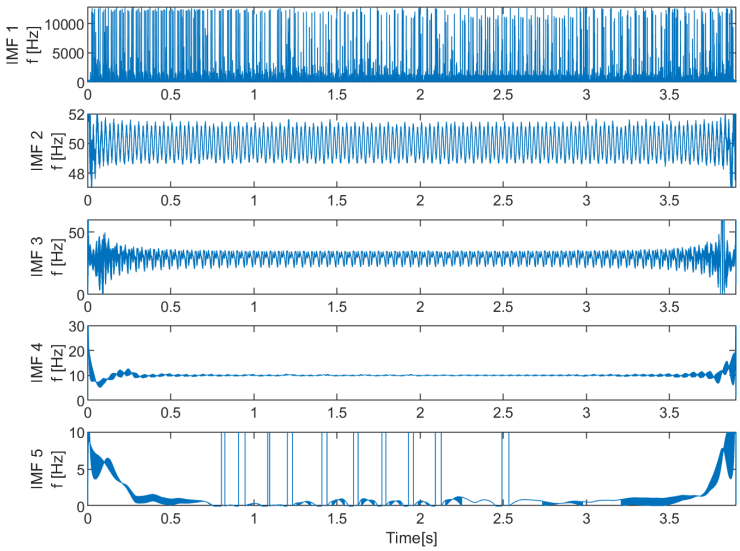

Figure A.16: IF of IMFs after adding masking signal $g_{m1}(t)$ to $g(t)$.

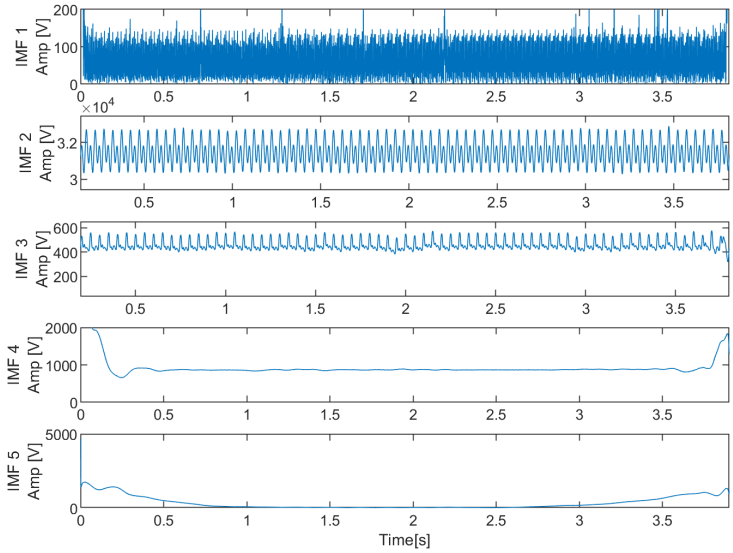

Figure A.17: IA of IMFs after adding masking signal $g_{m1}(t)$ to $g(t)$.

A.2.3 After extraction of the 50 Hz Component

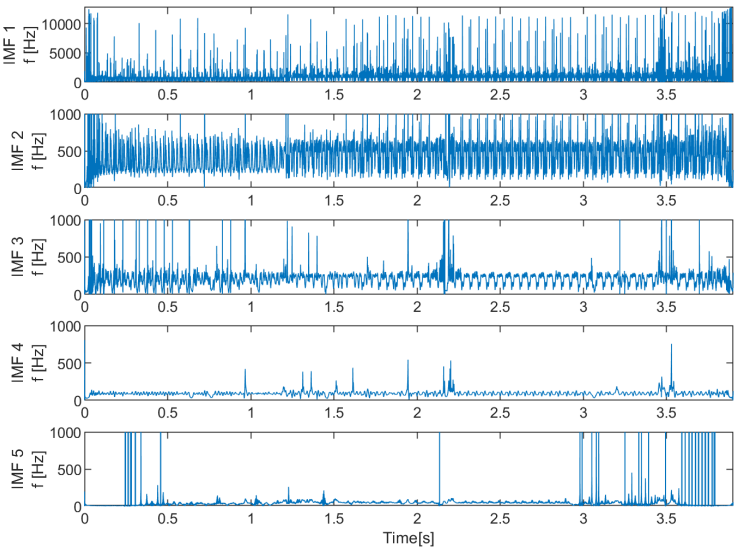

Figure A.18: IF of the IMFs from the EMD applied to $g_1(t)$.

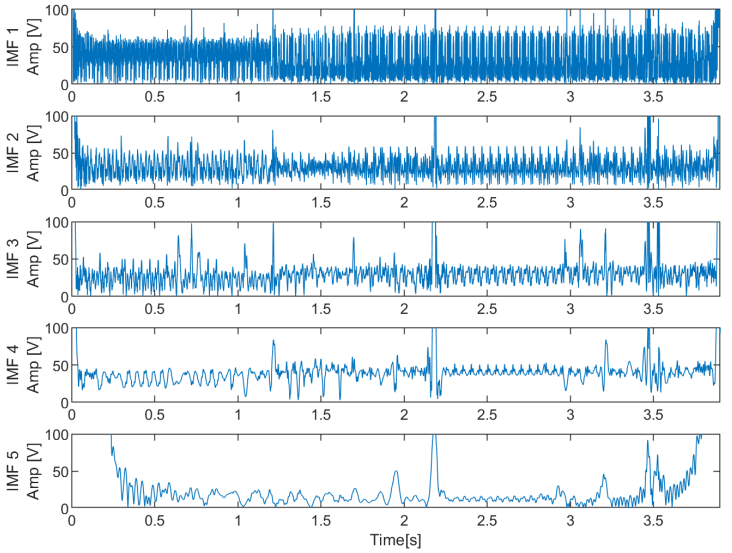

Figure A.19: IA of the IMFs from the EMD applied to $g_1(t)$.

A.2.4 After Applying Mask gm2

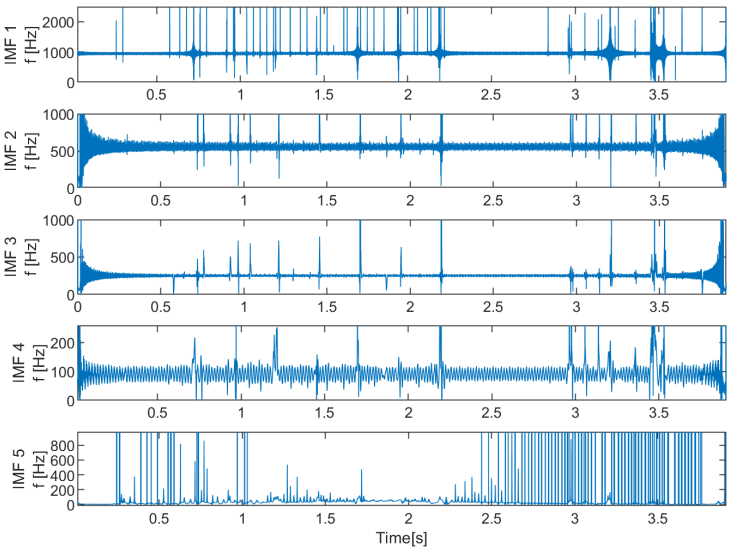

Figure A.20: IF of IMFs after adding masking signal $g_{m2}(t)$ to $g_1(t)$.

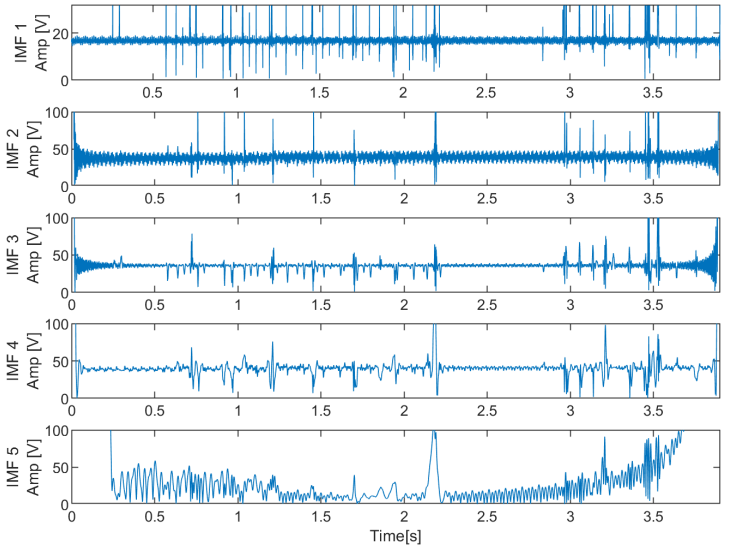

Figure A.21: IA of IMFs after adding masking signal $g_{m2}(t)$ to $g_1(t)$.

A.2.5 After extraction of the 50 Hz and 950 Hz Component

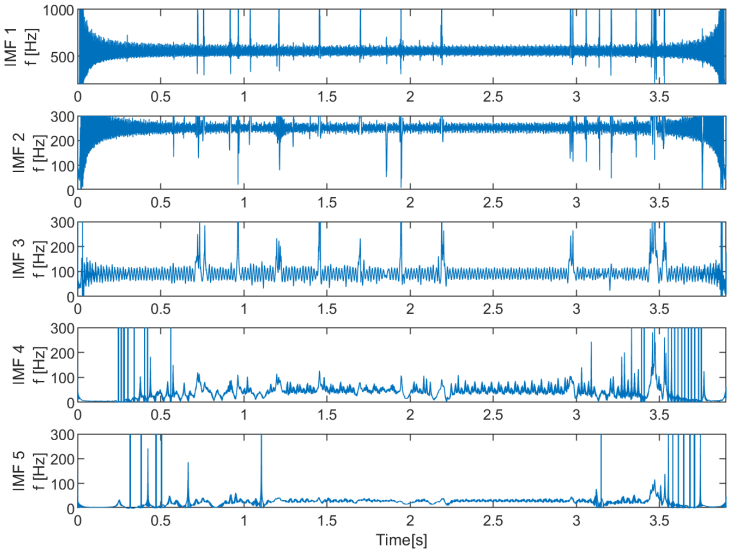

Figure A.22: IF of the IMFs from the EMD applied to $g_2(t)$.

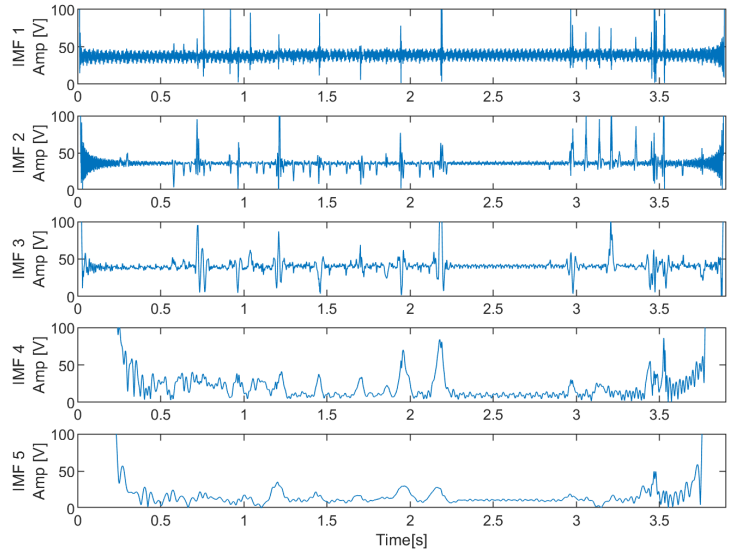

Figure A.23: IA of the IMFs from the EMD applied to $g_2(t)$.

A.2.6 After Applying Mask gm3

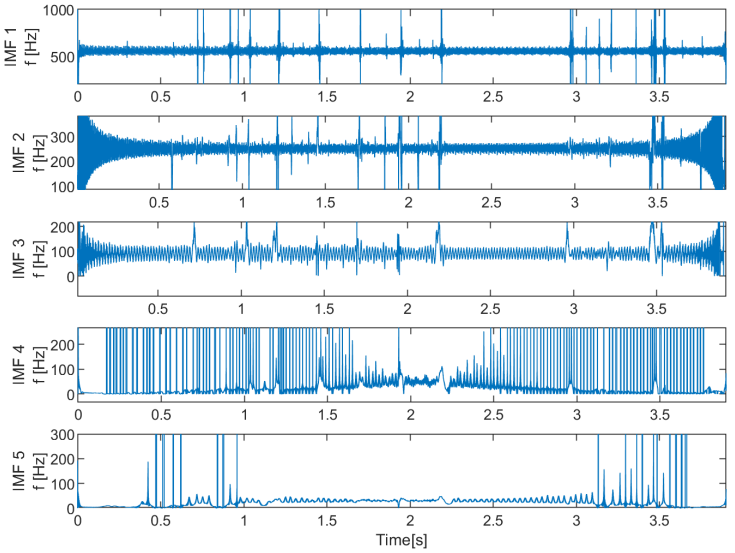

Figure A.24: IF of IMFs after adding masking signal $g_{m3}(t)$ to $g_2(t)$.

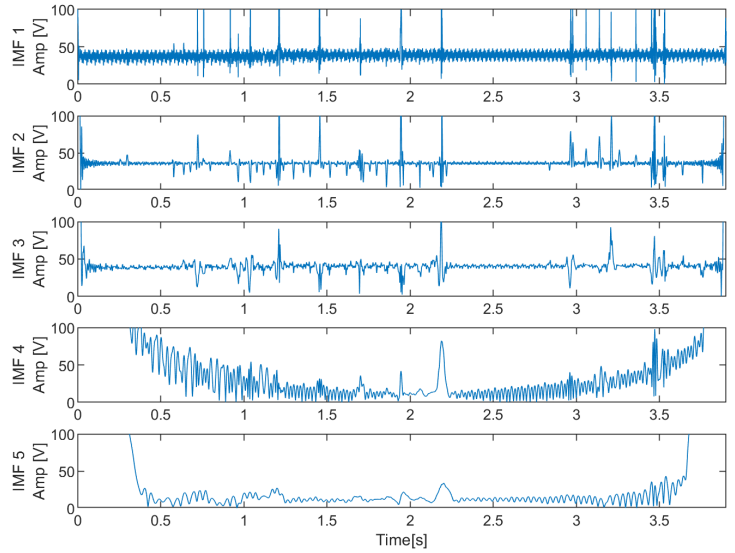

Figure A.25: IA of IMFs after adding masking signal $g_{m3}(t)$ to $g_2(t)$.

A.2.7 Resulting IMFs

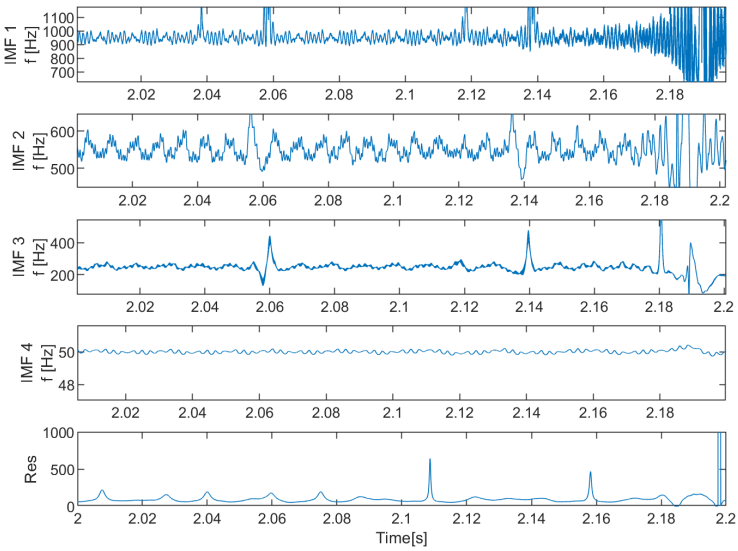

Figure A.26: Closer look at the IF of resulting IMFs of $g(t)$.

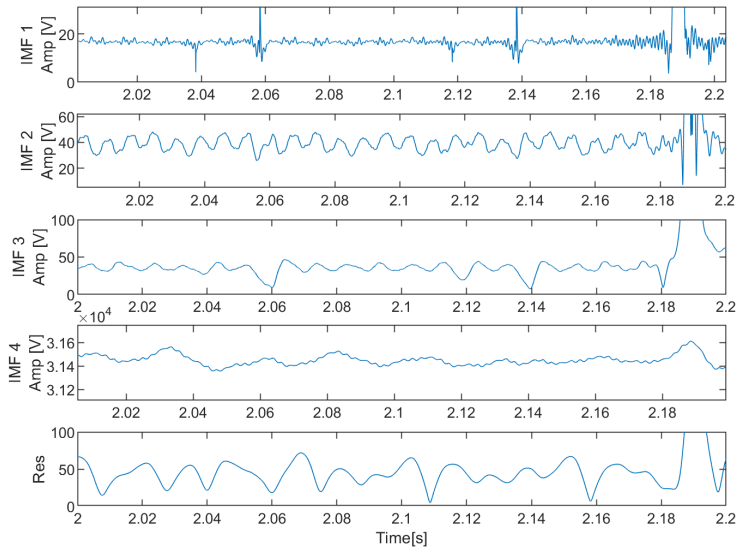

Figure A.27: Closer look at the IA of resulting IMFs of $g(t)$.

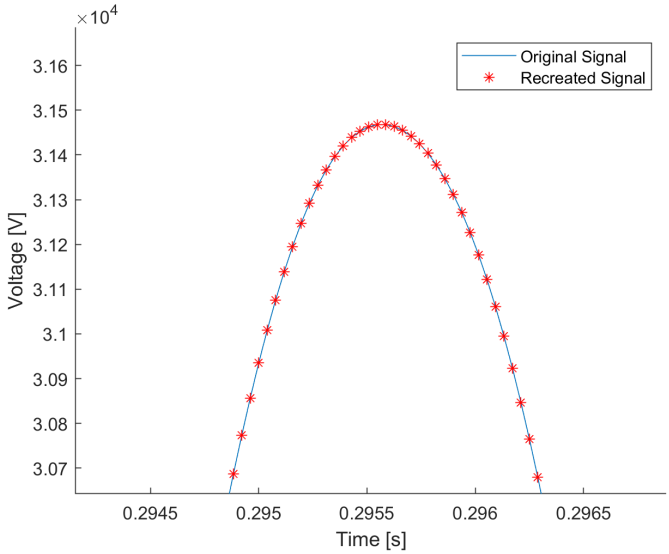

Figure A.28: Recreation of original signal $g(t)$ from the resulting IMFs.

Erlend Westad

Instantaneous Frequency Identification in Microgrids Through Adaptive Data Analysis

NTNU
Norwegian University of
Science and Technology